Ministério da Ciência e Tecnologia

GOVERNO FEDERAL

CHARACTERIZATION OF EXOPLANET CANDIDATES FROM HUBBLE SPACE TELESCOPE ASTROMETRY, GROUND-BASED RADIAL VELOCITY, AND INFRARED INTERFEROMETRY

Eder Martioli

Doctorate Thesis at Post Graduation Course in Astrophysics, advised by Drs. Francisco Jablonski, Barbara E. McArthur, and G. Fritz Benedict, approved in June 9, 2010.

URL of the original document:
<http://urlib.net/8JMKD3MGP7W/37JAFA5>

INPE
São José dos Campos
2010

Ministério da Ciência e Tecnologia

GOVERNO FEDERAL

CHARACTERIZATION OF EXOPLANET CANDIDATES FROM HUBBLE SPACE TELESCOPE ASTROMETRY, GROUND-BASED RADIAL VELOCITY, AND INFRARED INTERFEROMETRY

Eder Martioli

Doctorate Thesis at Post Graduation Course in Astrophysics, advised by Drs. Francisco Jablonski, Barbara E. McArthur, and G. Fritz Benedict, approved in June 9, 2010.

INPE

São José dos Campos

2010

Aprovado (a) pela Banca Examinadora em cumprimento ao requisito exigido para obtenção do Título de Doutor(a) em Astrofísica

Dra.   Adriana Benetti Marques Válio

Presidente / CRAAM/Mackenzie / São Paulo - SP

Dr.   Francisco José Jablonski

Orientador(a) / INPE / SJCampos - SP

Dr.   Deonísio Cieslinski

Membro da Banca / INPE / SJCampos - SP
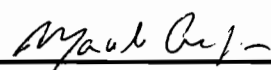
Dr.   José Williams dos Santos Vilas Boas

Membro da Banca / INPE / SJCampos - SP

Dr.   Eduardo Janot Pacheco

Convidado(a) / IAG/USP / São Paulo - SP

Dr.   Marcelo Assafin

Convidado(a) / UFRJ / Rio de Janeiro - RJ

Aluno (a):   Eder Martioli

São José dos Campos, 09 de junho de 2010

To my family.

ACKNOWLEDGEMENTS

Finally, I should point up that I have not mentioned everyone who deserves being here. For this reason I would like to express my general but sincere gratitude to all of my friends, co-workers, and family members, who witnessed my quest and in some way supported me and made this thesis possible. These people surely know how important they were and still are to me.

ABSTRACT

In this work we present the development of observational techniques and data analysis for the follow-up of RV-detected exoplanet candidates and low-mass companions. We observed the exoplanet candidate systems HD 136118 and HD 33636, for which we present high-cadence radial velocity data obtained with the High Resolution Spectrograph on the Hobby-Eberly Telescope, and relative astrometry with the FGS-1r instrument on the Hubble Space Telescope. We performed a simultaneous analysis of these data in order to characterize the orbit of the companions thoroughly. This establishes the actual mass of HD 136118 b, $M_b = 63^{+22}_{-13} \, M_J$, in contrast to the minimum mass determined from the radial velocity data only, $M_b \sin i \sim 12 \, M_J$. Therefore, the low-mass companion to HD 136118 is now identified as a likely brown-dwarf residing in the "brown-dwarf desert". Our results for HD 33636 are consistent with those found in the literature. For the latter object we also present experimental infrared interferometric observations with the AMBER instrument at the Very Large Telescope Interferometer. We have identified visibility variations consistent with an additional light with flux ratio of 30%. This result is incompatible with those obtained from the other two experiments, i.e. a binary system that is composed of a G0 V primary star and an M-dwarf companion.

CARACTERIZAÇÃO DE CANDIDATOS A EXOPLANETAS VIA ASTROMETRIA COM O TELESCÓPIO ESPACIAL, MEDIDAS EM TERRA DE VELOCIDADES RADIAIS E INTERFEROMETRIA NO INFRAVERMELHO

RESUMO

Neste trabalho são desenvolvidas técnicas observacionais e análise de dados para o estudo de candidatos a exoplanetas e companheiras de baixa massa detectados via velocidades radiais. Foram observados os sistemas HD 136118 e HD 33636. As observações incluem medidas de alta-cadência de velocidades radiais com o espectrógrafo de alta resolução do telescópio Hobby-Eberly e medidas astrométricas com o Sensor de Guiagem Fina 1r do telescópio espacial HST. Os dados de ambos experimentos foram analisados simultaneamente para a caracterização completa da órbita das companheiras. O trabalho resultou na determinação da massa verdadeira de HD 136118 b, $M_b = 63^{+22}_{-13}\,\mathrm{M_J}$. Essa massa é relativamente maior que a massa mínima determinada anteriormente via velocidades radiais, $M_b \sin i \sim 12\,\mathrm{M_J}$. Portanto, HD 136118 b é identificada como uma provável anã-marrom que reside no "deserto das anãs-marrons". Os resultados obtidos para o sistema HD 33636 são consistentes com os encontrados na literatura. Para HD 33636, ainda foram realizadas medidas interferométricas experimentais no infravermelho com o instrumento AMBER e três telescópios do Very Large Telescope Interferometer . Foram identificadas variações na visibilidade interferométrica que são consistentes com uma luz adicional com razão de fluxos de aproximadamente 30%. Este resultado é inconsistente com os resultados dos dois primeiros experimentos, ou seja, um sistema binário constituído por uma estrela primária do tipo G0 V e uma companheira anã do tipo M.

LIST OF FIGURES

xvi

CONTENTS

1 INTRODUCTION

Centuries ago philosophers and scientists like Giordano Bruno and Isaac Newton have already assumed the possibility of planets existing around stars other than the Sun. Although it has been conjectured long ago, the search for exoplanets only became possible when the experiments in astronomy reached maturity. The search for other worlds has started with astrometric measurements. Jacob (1855) announced the discovery of a likely planetary body orbiting the binary star 70 Ophiuchi. He asserted the discovery of a third unseen companion affecting the orbit of the two visible stars. His discovery has never been confirmed. Later on, during the 1950s and 1960s, Peter van de Kamp also claimed the astrometric detection of planetary bodies orbiting the Barnard's Star (KAMP, 1969), the largest proper motion star in the sky. It was found later that his photographic plate technique had not attained sufficient precision for the detections he was claiming. In a recent work, Benedict et al. (1999), using the Fine Guidance Sensors (FGS) with the *Hubble Space Telescope* (*HST*), have found no companion to Barnard's star, with a companion detection sensitivity less than or equal to one Jupiter mass, for periods longer than 150 days.

Although the first attempts to detect exoplanets were astrometric, the first discovery of a planetary body outside the Solar System came along through a different technique. In 1992, radio astronomers Aleksander Wolszczan and Dale Frail announced the discovery of planets around a pulsar, PSR 1257+12 (WOLSZCZAN; FRAIL, 1992), using pulsar timing variations. On October 6, 1995, Michel Mayor and Didier Queloz of the University of Geneva announced the first definitive detection of an exoplanet orbiting an ordinary main-sequence star, 51 Pegasi (MAYOR; QUELOZ, 1995). The latter was possible using the Radial Velocity (RV) method. The technological advances and the development of this technique have contributed to the detection of the majority of exoplanets to date. The number of detections has been raising very rapidly in the last few years and today over 400 of these objects are known, most of which has been detected through the RV method. A full up-to-date list of exoplanets can be found at *http://exoplanet.eu*.

Planetary systems and binary (or multiple) star systems are currently becoming part of the same field of study in astronomy. The reason for this is that these objects are all of the same kind, a Multiple Orbiting Body System (MOBS). Although the bodies involved in each kind of system may be very different physically, on what concerns the observing techniques they turn out to be very alike. The study of MOBS

has become highlighted in the past few years due to the discovery of exoplanets. The great attention given to this field is obviously motivated by the possibility of finding bodies that might be similar to the Earth and perhaps host some kind of extraterrestrial life. Although this would be the most exciting achievement for the exoplanetary research, an important progress in this field has already been done. For example, the understanding of how planets, brown-dwarfs and low-mass stars are formed. Few years ago the only known planets were those in the Solar System. Today, the hundreds of exoplanets present an entire "zoo" of planetary systems. Among these, one can find even unprecedented classes of planets, like the Hot-Jupiters and Super-Earths. There are also planets in very unusual and unexpected conditions, like those in very eccentric orbits, or those in extremely short period orbits. Multiple systems are common, including some systems that resemble our own, like υ And and 55 Cnc. Exoplanet candidates have been found in many different environments, like in binary stars systems, around pulsars, around brown dwarfs, among others. Exoplanetary systems also present themselves as excellent laboratories to test theories in orbital dynamics. This has provided important contributions to the study of planet formation in general as well as to the study of our own Solar System. These discoveries are certainly just the tip of the iceberg, since the techniques employed are still limited and under growing technological development. The outstanding precision required for the detection of exoplanets in part motivates these advances and as a benefit many other areas in astrophysics may be privileged. In particular those that make use of the same techniques, like the MOBS.

A good illustration to show the limitation of methods for detecting exoplanets is the fact that for most objects detected to date only a few of them have their actual mass known. The widely used Doppler spectroscopy technique (same as Radial Velocity) yields the radial velocity component of the stellar perturbation only. Consequently, the inclination of the orbital plane is unknown and only the minimum mass of the companion may be determined. To fully determine the orbit and obtain a companion's true mass it is necessary to make use of additional techniques. Note that the mass is a crucial parameter, since it is definitive to classify a body as a planet.

The first precise determination of an exoplanet mass was made for a transiting system (HENRY et al., 2000). In transiting systems the planet crosses the stellar disk once every orbital passage. This phenomenon permits one to determine the inclination of the orbital plane with respect to our line of sight, removing the $M \sin i$

degeneracy, thus providing the true mass of the companion. The success of the transit method is based on extensive ground-based search programs and on the ongoing space missions CoRoT from the European Space Agency (ESA) and Kepler from NASA. Together, these programs have detected over 80 transiting systems, which represent about 20% of all exoplanet candidates. The transit is also yet the only method that provides the measurement of planetary radius, and in some cases, it also provides the atmospheric absorption spectrum (CHARBONNEAU et al., 2002; RICHARDSON et al., 2007; REDFIELD et al., 2008). These features comprise valuable information to yield accurate physical models of planetary atmospheres and internal structure. The drawback of the transit method is that transits occur only for systems that are oriented edge-on, and they have only a small probability of occurrence. In particular the chances increase for close-in planets. As a consequence all transiting planets detected to date has semimajor axes less than about 0.1 AU.

Another way to determine the orbital inclination of an unseen companion is by measuring the stellar reflex motion astrometrically. The first astrometrically determined mass of an exoplanet by Benedict et al. (2002) was possible thanks to the high precision of the FGS instrument on the *HST*. The FGS provides per observation precisions of better than 1 mas for relative astrometry. This unique capability enables the detection of stellar perturbations due to planetary mass companions in wide orbits.

For this thesis work we were granted observing time with the *HST* to measure the perturbation and determine the true mass of HD 136118 b, which is an exoplanet candidate found by radial velocity measurements (FISCHER et al., 2002). We have also been granted observing time with the Hobby-Eberly Telescope (HET) to obtain high-cadence radial velocity measurements. This supplements previously published data and provides better constrain on the companion's spectroscopic orbital parameters. A similar experiment has been performed for the exoplanet candidate HD 33636 b, for which the results are published in Bean et al. (2007). The companion to HD 33636 is an M-dwarf star. We have selected this object as a test-bed to perform interferometric measurements as an additional and alternative technique to the *HST* astrometry. We were granted observing time with the Very Large Telescope Interferometer (VLTI) in a short Science Verification (SV) run for testing the new instrument, Fringe-tracking Instrument of NIce and Torino (FINITO), working with the Astronomical Multi-BEam combineR (AMBER), in order to measure the binary

parameters of HD 33636.

In summary, the primary goal of this work is the development of methods for combining the two techniques, Doppler spectroscopy and relative astrometry, and if possible, include infrared interferometry data. These are meant to be analyzed simultaneously, in order to provide a thorough characterization of exoplanet candidates and MOBS in general. The advantage of combining multiple techniques is that one may constrain parameters in the model and determine them more precisely. It means that it provides more information about bodies involved in the system. Some parameters are critical and without this information it is almost impossible to define what kind of body is involved in the MOBS.

Below we outline the contents of this work.

- Related Work - brief description of works that motivated us and that present results obtained in a similar way as the experiments developed in this thesis. We also include the previous results from each individual object in study.

- Background - overview on the background theory for the astrophysical models and experiments.

- Experiments Design - detailed description of the experiments and the observational techniques employed.

- Data Reduction - detailed description of the methods used to calibrate data and extraction of observables from each experiment.

- Data Analysis - analysis of the reduced data in order to obtain the relevant physical information from each observed system.

- Results and Discussion - discussion on the results and their main astrophysical implications.

- Summary and Conclusions - summary of achievements obtained with this work and concluding remarks.

2 RELATED WORK

2.1 Motivation

The main motivation for this thesis work is that the Doppler spectroscopy technique is insufficient to characterize the systems thoroughly. Therefore, we make use of *HST* astrometry in order to better understand these systems. We also propose infrared interferometry as an additional tool for obtaining further information from the system. Below we describe some related works found in the literature that have motivated us and that provided us with the necessary background for the development of these experiments.

2.2 Radial Velocity

The RV technique consists of measuring the star's velocity through the shift of spectral lines due to the Doppler effect. In order to obtain precise radial velocities, it is important to perform a careful treatment of the spectral data. Baranne et al. (1996) present a method to reduce the ELODIE spectrograph data, which was the responsible for the first, and many other detections of extrasolar planet candidates around Sun-like stars. The success of this method is based on a long learning process on how to obtain the best performance of a high resolution echelle spectrograph. This involves a complete knowledge of the system in use, which permits one to keep track on every source of systematic errors, and thus be able to correct them. Additionally, the use of an efficient numerical method, the cross-correlation spectroscopy, is shown to provide a considerable improvement on the precision.

At about the same time, another efficient technique was developed by Butler et al. (1996), who have attained comparable radial velocity precision using the iodine method. This technique has also led to the discovery of many exoplanet candidates. We have employed the same methodology for our spectroscopic measurements. The reason for choosing this method rather than Baranne et al. (1996)'s is that the iodine technique provides means to calibrate data through pos-processing analysis, without the need for an extremely accurate knowledge of the system. This method together with the large collecting area of the Hobby-Eberly Telescope (HET), and the quality of its High-Resolution Spectrograph (HRS) allowed us to obtain relative velocity precision of about $\sim 3\,\mathrm{m/s}$.

2.3   Astrometry

One of our main results is to show the importance of using complementary techniques to the RV method in the characterization of low-mass companions. The relative astrometry with FGS/*HST* is a potential technique to explore the entire orbit of the star due to unseen companions. This method is shown to be efficient for variations due to companions within a range of minimum masses, $5 < M \sin i < 17 \, \mathrm{M_J}$. In our measurements, we were able to estimate the key orbital elements of the RV-detected companion to HD 136118 like the perturbation orbit size, α, the longitude of the ascending node, Ω, and the inclination, i, thus turning $M \sin i$ into true mass, M. A similar approach has already been performed in previous work, where *HST* astrometry and ground-based radial velocities have been combined to determine the orbit and the true mass of exoplanet candidates. Gliese 876 b, a planetary companion to the M dwarf star Gl 876 (BENEDICT et al., 2002), is the case where *HST* astrometry allowed the determination of the true mass of an exoplanet candidate companion, $M_b = 1.89 \pm 0.34 \, \mathrm{M_J}$, which is now unequivocally defined as a Jupiter-like giant planet. Only the transiting star-planet systems can provide a mass estimate with smaller error. In contrast to that short-period system, the same techniques have been used to determine the inclination for the outermost known planet 55 Cnc d in the 55 Cnc system (MCARTHUR et al., 2004), a companion with a period, $P = 4517 \, \mathrm{days}$. In this case seventeen data sets over 380 days resulted in an inclination with a 13% error. The perturbation had a semi-amplitude $\alpha = 1.9 \pm 0.4 \, \mathrm{mas}$. As it will be shown in our results, we found similar levels of precision for HD 136118 with observations spread over about a similar time span, because shorter periods result in great curvature in the perturbation. In a recent work McArthur et al. (2010) have determined the true mass of two exoplanet candidate companions to the υ And system, $M_c = 13.98^{+2.3}_{-5.3} \, \mathrm{M_J}$ and $M_d = 10.25^{+0.7}_{-3.3} \, \mathrm{M_J}$, which is the first multi-planet system with accurate mass determination for two components. This is also the first determination of the mutual inclination between objects in an extrasolar system. Notice that υ And is a wide binary star system, for which the component υ And A is a solar type star with three planetary companions.

The FGS/*HST* astrometric observations of the G4 IV star HD 38529 have also provided the measurement of the mass of the outermost of two previously known companions (BENEDICT et al., 2010). The mass of HD 38529 c is $M_c = 17.6^{+1.5}_{-1.2} \, \mathrm{M_J}$, which is 3σ above a $13 \, \mathrm{M_J}$ deuterium burning, brown dwarf lower limit.

In contrast to the exoplanet candidates Gl876 b, 55 Cnc d, and υ And c and d, which have been identified as truly planetary bodies, and HD 38529 c, as a brown dwarf companion, the other exoplanet candidate observed by FGS/*HST*, HD 33636 b, has been identified as an M dwarf stellar companion, with true mass $M = 142 \pm 11\,\mathrm{M_J}$ (BEAN et al., 2007). HD 33636 b has firstly been detected through RV (VOGT et al., 2002; PERRIER et al., 2003; BUTLER et al., 2006), showing a minimum mass of $M \sin i = 9.3\,\mathrm{M_J}$, which is consistent with planetary mass. This discrepancy occurs due to the nearly face-on orbit orientation. This proves the efficiency of astrometry in complementing the RV method to access the real nature of a planetary system.

Given the high astrometric signal from HD 33636 we have selected this system as an experimental case of study to validate the methods used in the analysis of HD 136118 data. The companion to HD 33636 is likely to provide a larger flux contribution to the system, therefore it is a suitable target to perform an interferometric experiment using the AMBER instrument at VLTI. This sort of experiment has already been performed as explained below.

2.4 Interferometry

The interferometric experiment we present in this work is not an attempt of direct imaging, rather it is just an attempt of detecting any interferometric signature in the infrared originated from the unseen companion. The contrast between a hot parent star and its cooler companion is much favorable in the infrared region of spectra. Besides, interferometry provides two main features that favors the detection of exoplanets and low mass companions. First it combines the light collected from many optical telescopes, therefore resulting in larger collecting area than in single instruments. Second, an interferometer can probe the light distribution at very small angular scales. These characteristics are essential for the detection of any weak luminous feature lying close to the stellar disk, just like planets. The theory relating interferometric observables to the binary parameters is explained in Chelli et al. (2009). Duvert et al. (2010) have recently published the results of an interferometric experiment for the detection of a close faint companion using AMBER/VLTI, thus very similar to the experiment presented here.

2.5 Individual Objects

In this section we provide a compilation of facts from the targets in study. The targets, HD 136118 and HD 33636, are solar type main-sequence stars with RV-detected low mass companions, both of which present $M \sin i$ below the planetary limit, $\lesssim 13 \, M_J$. HD 136118 (=HIP 74948) is a $V = 6.93$, F9 V star with roughly solar photospheric abundances (GONZALEZ; LAWS, 2007). Table 2.1 summarizes its observed properties given in the literature. HD 33636 (=HIP 24205) is a high-proper motion, $V = 7.0$ G0 V solar-type star at a distance of 30 pc. Table 2.2 summarizes its observed properties.

TABLE 2.1 - Properties of HD 136118.

ID	HD 136118	Unit	Reference
RA(2000)	$15:18:55.4719$	h:m:s	Perryman et al. (1997)
Dec(2000)	$-01:35:32.590$	d:m:s	Perryman et al. (1997)
μ_α	-123.6 ± 0.4	$\mathrm{mas\,yr^{-1}}$	this work
μ_δ	23.59 ± 0.19	$\mathrm{mas\,yr^{-1}}$	this work
π_{abs}	19.9 ± 0.6	mas	this work
Γ	-3.6 ± 0.1	$\mathrm{km\,s^{-1}}$	Perryman et al. (1997)
Spc type	F9V	-	Martioli et al. (2010)
Age	$4.8^{+0.7}_{-1.9}$	Gyr	Saffe et al. (2005)*
[Fe/H]	-0.01 ± 0.05	dex	Gonzalez & Laws (2007)
[C/H]	0.05 ± 0.08	dex	Gonzalez & Laws (2007)
[O/H]	0.11 ± 0.05	dex	Gonzalez & Laws (2007)
[Si/H]	-0.04 ± 0.06	dex	Gonzalez & Laws (2007)
[Ca/H]	-0.06 ± 0.06	dex	Gonzalez & Laws (2007)
d	52.3 ± 0.6	pc	Martioli et al. (2010)
$v \sin i$	7.33 ± 0.5	$\mathrm{m\,s^{-1}}$	Butler et al. (2006)
P_{rot}	12.2	day	Fischer et al. (2002)
T_{eff}	6097 ± 44	K	Butler et al. (2006)
$\log g$	4.16 ± 0.09	$\mathrm{cm\,s^{-2}}$	Prieto & Lambert (1999)
M_*	1.24 ± 0.07	$\mathrm{M_\odot}$	Fischer et al. (2002)
R_*	1.58 ± 0.11	$\mathrm{R_\odot}$	Prieto & Lambert (1999)
BC	0.01 ± 0.03	mag	Prieto & Lambert (1999)
M_V	3.34	mag	Prieto & Lambert (1999)
B	7.432	mag	Zacharias et al. (2010)
V	6.945	mag	Zacharias et al. (2010)
R	6.630	mag	Zacharias et al. (2010)
J	5.934	mag	Cutri et al. (2003)
H	5.693	mag	Cutri et al. (2003)
K	5.599	mag	Cutri et al. (2003)

*Age value and limits derived from isochrone method

TABLE 2.2 - Properties of HD 33636.

ID	HD 33636	Unit	Reference
RA(2000)	$05:11:46.449$	h:m:s	Zacharias et al. (2005)
Dec(2000)	$+04:24:12.74$	d:m:s	Zacharias et al. (2005)
μ_α	180.3 ± 0.4	$\mathrm{mas\,yr^{-1}}$	this work
μ_δ	-137.8 ± 0.3	$\mathrm{mas\,yr^{-1}}$	this work
π_{abs}	34.98 ± 0.28	mas	this work
d	28.59 ± 0.23	pc	this work
Γ	5.3 ± 0.2	$\mathrm{km\,s^{-1}}$	Nordstrom et al. (2004)
Spc type	G0 V	-	Bean et al. (2007)
Age	5.0 ± 1.9	Gyr	Fischer & Valenti (2005)*
[Fe/H]	-0.13	dex	Vogt et al. (2002)
[Na/H]	-0.22	dex	Fischer & Valenti (2005)
[Si/H]	-0.09	dex	Fischer & Valenti (2005)
$v \sin i$	3.08	$\mathrm{m\,s^{-1}}$	Butler et al. (2006)
P_{rot}	13	day	Vogt et al. (2002)
T_{eff}	5904	K	Butler et al. (2006)
$\log g$	4.37 ± 0.04	$\mathrm{cm\,s^{-2}}$	Prieto & Lambert (1999)
M_*	1.02 ± 0.03	$M_\odot$	Takeda et al. (2007)
R_*	1.26 ± 0.03	$R_\odot$	Prieto & Lambert (1999)
BC	0.07	mag	Prieto & Lambert (1999)
M_V	4.71 ± 0.17	mag	Prieto & Lambert (1999)
B	7.559	mag	Zacharias et al. (2010)
V	6.990	mag	Zacharias et al. (2010)
R	6.600	mag	Zacharias et al. (2010)
J	5.931	mag	Cutri et al. (2003)
H	5.633	mag	Cutri et al. (2003)
K	5.572	mag	Cutri et al. (2003)

*Age value and limits derived from isochrone method

3 BACKGROUND

This chapter provides the basic background theory concerned in the experiments and data analysis.

3.1 The Kepler's Laws

Johannes Kepler deduced empirically three 'laws' of planetary orbital motion. Although these were obtained specifically for the orbits of the planets around the Sun they can be generalized for any unperturbed orbit involving two bodies. For this reason it is widely used in the analysis of binary stars and exoplanets. The Kepler's laws and their generalization are given below:

1st Law - The planet moves along elliptical path with the Sun at one focus. We can express the planet's distance from the Sun as:

$$r = \frac{a(1 - e^2)}{1 + e \cos f},$$ (3.1)

with a the semimajor axis, e the eccentricity and f the true anomaly. Notice that this expression gives the orbit in polar coordinates. The center of coordinates is taken at the position of the central body, the Sun, which is considered to be much more massive than the orbiting body. For the general case of two orbiting bodies with comparable masses (hereafter binary), both bodies move along elliptical paths with the barycenter at one focus. Nevertheless, Equation 3.1 still holds for the distance of each body to the barycenter. Note that each body has a particular semimajor axis, which can be computed through the following equation:

$$a_A M_A = a_B M_B,$$ (3.2)

where a_A and a_B are the semimajor axes, and M_A and M_B are the masses. By convention the true anomaly f is the angle measured from the periastron passage counterclockwise. This makes f from each component be delayed by $180°$.

2nd Law - A line connecting the planet and the Sun sweeps out an area, A, at constant rate dA/dt. For binaries, the line connecting the two bodies passes

through the shared focus and both bodies sweep out areas at constant rate.

3rd Law - The square of planet's orbital period (in years) is equal to the cube of its semimajor axis (in AU):

$$P_{yr}^2 = a_{AU}^3. \tag{3.3}$$

Equation 3.3 only holds for Solar System planets. To consider planets around a star other than the Sun, one should include the star mass (in solar units) as follows:

$$P_{yr}^2 = \frac{a_{AU}^3}{M_{M_\odot}}. \tag{3.4}$$

Equations 3.3 and 3.4 assume the mass of the planet is negligible compared to the star mass. The general expression that may be used for binaries must include the masses of each body explicitly, and is given as follows:

$$\left(\frac{P}{2\pi}\right)^2 = \frac{a^3}{G(M_A + M_B)}, \tag{3.5}$$

where G is the gravitational constant, and a is the semimajor axis of the relative motion between the two bodies, also given by $a = a_A + a_B$. By making use of Equation 3.2 we can rewrite Equation 3.5 for the orbit of a particular body around the barycenter:

$$\left(\frac{P}{2\pi}\right)^2 = \frac{(M_A + M_B)^2 a_A^3}{G M_B^3}, \tag{3.6}$$

where we have chosen the body A. In order to obtain this expression for body B one just needs to switch the index letters.

3.2 Physics of Orbital Motion

The Kepler's laws are empirical and work well only when the dominant force is the one between the two bodies. However, the theory to explain orbits for the more general case with multiple gravitationally interacting bodies is based on Newton's Universal Law of Gravitation,

$$F = G\frac{M_A M_B}{r^2}, \tag{3.7}$$

where G is the gravitational constant, F is the gravitational attractive force between two particles with masses M_A and M_B, which are separated by the distance r. The total gravitational force applied to a given particle in a system of N particles may be written as the resultant of all forces from the interaction with the other $N-1$ particles:

$$\mathbf{F}_i = G m_i \sum_{j \neq i}^{N} \frac{m_j}{r_{ij}^3} \mathbf{r}_{ij}. \tag{3.8}$$

We have introduced the vectorial force, $\mathbf{F}_i$, and the difference between the position vectors, $\mathbf{r}_{ij} \equiv \mathbf{r}_j - \mathbf{r}_i$. The positions are relative to an arbitrary inertial system of coordinates. It has also been used the definition $\mathbf{r} \equiv r\hat{r}$.

In order to obtain the equations of motion for a given particle, one should make use of Newton's Second Law in Equation 3.8 for all particles, and therefore solve the following system of differential equations:

$$\begin{cases} \frac{d^2 \mathbf{r}_1}{dt^2} = ... \\ ... \\ \frac{d^2 \mathbf{r}_i}{dt^2} = G \sum_{j \neq i}^{N} \frac{m_j}{r_{ij}^3} \mathbf{r}_{ij}, \\ ... \\ \frac{d^2 \mathbf{r}_N}{dt^2} = ... \end{cases} \tag{3.9}$$

This expression is valid when no external force is present. Any additional force should be included as an additional term on the right side of Equation 3.9 divided by the particle mass m_i.

3.3 The Two-Body Problem

For the case where $N = 2$, the two-body problem, Equation 3.9 leads to the following system of equations:

$$\begin{cases} \frac{d^2\mathbf{r}_1}{dt^2} = G\frac{m_2}{r_{12}^3}\mathbf{r}_{12}, \\ \frac{d^2\mathbf{r}_2}{dt^2} = G\frac{m_1}{r_{21}^3}\mathbf{r}_{21}. \end{cases} \tag{3.10}$$

Note that $r_{12} = r_{21}$ and $\hat{r}_{12} = -\hat{r}_{21}$. Subtracting the first equation from the second, and letting the relative position vector be $\mathbf{r} \equiv \mathbf{r}_2 - \mathbf{r}_1$, we have the following:

$$\ddot{\mathbf{r}} + \frac{\mu}{r^3}\mathbf{r} = 0, \tag{3.11}$$

where it has been defined the gravitational coefficient $\mu \equiv G(m_1 + m_2)$. Equation 3.11 is a second order ordinary differential equation that needs to be solved in order to obtain the equation of motion for the relative position $\vec{r}(t)$ of particle 2 with respect to the particle 1.

The general solution for Equation 3.11 is a conic section, which depending on the total energy of each body can be either an ellipse, a hyperbola or a parabola. The particular solution that leads to an ellipse is the same as Equation 3.1, which was obtained empirically by Kepler.

Since Equation 3.11 is of vectorial type, it is in fact a system of three independent differential equations of second order, each of which requires two boundary conditions, $r(t_0)$ and $\dot{r}(t_0)$, at arbitrary time t_0, in order to provide a unique solution. Therefore, the 3-D components of position and velocity at a given time must be provided. However, these are not the only set of elements that may be provided. Equivalently one could use a different set of six parameters, the orbital elements. Although there are several definitions for the orbital elements, we adopt here the Keplerian elements, which are the following: eccentricity (e), semimajor axis (a), inclination (i), longitude of the ascending node (Ω), argument of periastron (ω) and mean anomaly at epoch (M).

A proper choice of the system of coordinates may provide a handful of relationships between the orbital elements and the cartesian coordinates. It will be shown that this is also important when one wants to relate these elements with the observables in the experiments. Figure 3.1 shows the geometry of an ellipse that has its focus lying closer to the periastron centered in a cartesian system of coordinates. By setting up this system, one is led to the definitions shown in Figure 3.1.
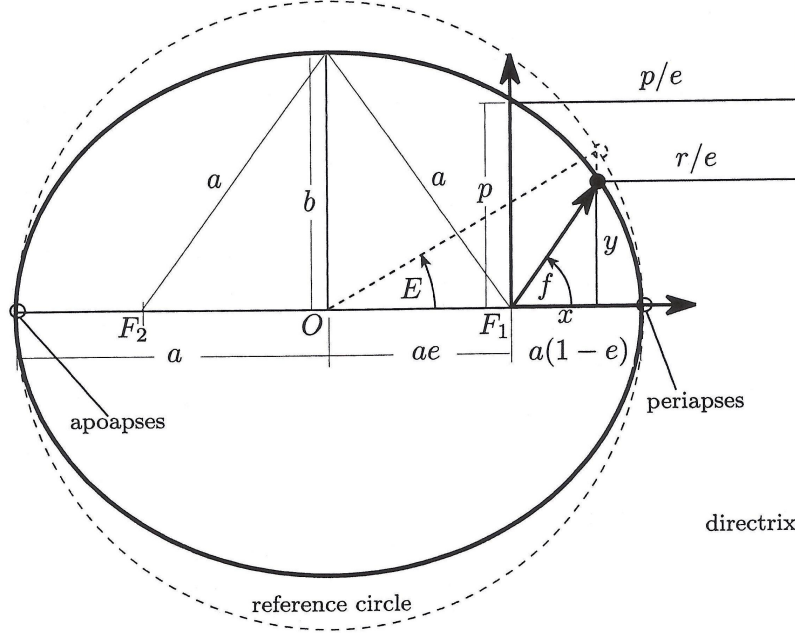
FIGURE 3.1 - Ellipse geometry.

Note that parameters e and a alone already define the shape of the orbit in the orbital plane. The mean anomaly M is the parameter that contains the time dependence and defines the orbital phase of the object. Although M is mathematically defined as an angle, it is not a real angle in the ellipse, it is rather the angle that varies linearly with time and is also defined as function of the orbital period (P), and of the epoch of periastron passage (T_0) through the following expression:

$$M = \frac{2\pi}{P}(t - T_0). \tag{3.12}$$

The angle E indicated on Figure 3.1 is the eccentric anomaly, which is related to the mean anomaly by the following expression:

$$M = E - e \sin E. \tag{3.13}$$

Equation 3.13 is known as the Kepler equation. The eccentric anomaly is related geometrically to the true anomaly (f), which is the argument of the position vector ($\mathbf{r}$) in polar coordinates (see Figure 3.1). Thus the following expression holds:

$$\tan \frac{f}{2} = \sqrt{\frac{1+e}{1-e}} \tan \frac{E}{2}. \tag{3.14}$$

The remaining orbital elements, i, Ω, and ω are the orientation angles. They represent the Euler angles to describe the orientation of an orbit in 3-dimensional Euclidean space. Therefore, any Keplerian orbit can be represented by its natural shape rotated by the orientation angles in space.

3.4 N-Body Problem

The N-body problem consists of solving the equations of motion (Equation 3.9) for a given body that is part of a system of N gravitationally interacting bodies. An analytic exact solution only exists for trivial problems, like the two-body problem. Therefore, any attempt to solve a general N-body problem is likely to be an approximation of the reality. In fact, to be more comfortable with non-exact solutions, we remind the reader that even for a two-body problem the model presented above is an approximation, since the more correct theory to calculate orbits is the General Theory of Relativity, developed by Albert Einstein. Given the precision of our experiments and the small separation angles involved in the astrometric experiments, the classical theory is suitable. However, although the interactions between bodies in a given observed system may be small enough to perturb the orbits at a level that is not detected in the experiments, when this small perturbations are propagated through many years, the outcome solution may diverge from what is expected. This means that Keplerian orbits may represent a suitable model for a short-term experiment, but it might be necessary to make use of a full treatment of the N-body problem for experiments that last more than a couple of orbits. Moreover, performing long-term simulations of a system with more than two components also requires N-body numerical integrator, and in some cases it is even necessary to make use of General Relativity (ADAMS; LAUGHLIN, 2006). In our analysis we have used the symplectic numerical integrator MERCURY which is fully described in Chambers (1999).

3.5   Experiment Models

3.5.1   Astrometry: Proper Motion and Parallax

In the analysis of astrometry data there are two main apparent intrinsic movements in the plane of sky for stars that should be taken into account. First, the apparent relative displacement of stars due to their galactic motions, also called the proper motion, $\vec{\mu}$, which is usually written in terms of its equatorial components, μ_α and μ_δ. These are angular velocities measured in units of milliseconds of arc per year (mas yr^{-1}). Stars appear to move slowly due to their large distances, therefore, for most of the cases, the displacement in each direction can be approximated by an uniform linear motion:

$$\Delta\xi = \mu_\alpha \Delta t, \tag{3.15}$$

$$\Delta\eta = \mu_\delta \Delta t, \tag{3.16}$$

where ξ and η are the standard coordinates.

Besides the intrinsic movement of each star, there is also an apparent movement resulting from the orbital motion of the Earth around the Sun, the parallactic displacement. This presents an annual parallactic motion with shape defined by the position of the target in the sky and size defined by the intrinsic distance of the star to the Sun. The parallactic orbit displacement is given by the following expressions:

$$\Delta\xi = P_\alpha \pi_{abs}, \tag{3.17}$$

$$\Delta\eta = P_\delta \pi_{abs}, \tag{3.18}$$

where π_{abs} is the amplitude of the parallactic ellipse, also called the absolute parallax. This relates to the physical distance to the object, $d = 1/\pi_{abs}$, where d is expressed in parsec and π_{abs} in seconds of arc. The indices α and δ represent the equatorial coordinates, Right Ascension (RA) and Declination (DEC), respectively. The terms P_α and P_δ are the parallax factors, defined in Kamp (1967),

$$P_\alpha = R_\oplus(\cos\epsilon\cos\alpha\sin\odot - \sin\alpha\cos\odot), \tag{3.19}$$

$$P_\delta = R_\oplus[(\sin\epsilon\cos\delta - \cos\epsilon\sin\alpha\sin\delta)\sin\odot - \cos\alpha\sin\delta\cos\odot], \tag{3.20}$$

where $R_\oplus$ is the Earth distance to the Sun expressed in astronomical units, $\epsilon \simeq 23°.4392794$, is the obliquity of the ecliptic, and $\odot$ is the geocentric longitude of the Sun in the ecliptic system, measured from the vernal equinox, in the direction of increasing right ascensions. All of these quantities vary on time and are related to the orbit of Earth around the Sun. The most accurate data to calculate these quantities can be found in the JPL Planetary and Lunar Ephemerides (STANDISH JR., 1998), which can be accessed through the address `http://ftpssd.jpl.nasa.gov`.

The proper motion and parallax can be modeled together and removed from the astrometric data using the following expressions:

$$\xi = \xi_0 - P_\alpha\pi_{abs} - \mu_\alpha\Delta t, \tag{3.21}$$

$$\eta = \eta_0 - P_\delta\pi_{abs} - \mu_\delta\Delta t, \tag{3.22}$$

where ξ_0 and η_0 are the measured standard coordinates for a given star in a given epoch, and ξ and η are the reduced standard coordinates. The latter provides an astrometric catalogue, which contains the star coordinates for a reference frame, which is chosen arbitrarily. These coordinates must match for all observations, and for this reason Equations 3.21 and 3.22 are called equations of condition.

3.5.2 Astrometry: Apparent Orbital Motion

The high precision of FGS allows us to measure the apparent reflex orbital motion of the star due to the presence of a low mass unseen companion. This orbital displacement may also be removed from the equations of conditions similarly to the parallactic orbit. The model for the apparent orbital displacements of the star around the barycenter between the star and a given low mass unseen companion is given below.

First we write the elliptical rectangular coordinates, x and y, in the unit orbit:

$$
\begin{aligned}
x &= (\cos E - e), & (3.23) \\
y &= \sqrt{1 - e^2} \sin E, & (3.24)
\end{aligned}
$$

where e is the eccentricity and E is the eccentric anomaly. Remember that E carries the dependence on time through the Kepler's equation (Equation 3.13). The projection of this true orbit onto the plane tangent to the sky gives the coordinates $\Delta x, \Delta y$. This projection can be expressed mathematically by:

$$
\begin{aligned}
\Delta x &= Bx + Gy, & (3.25) \\
\Delta y &= Ax + Fy, & (3.26)
\end{aligned}
$$

where B, A, G, F are the Thiele-Innes constants, given by:

$$
\begin{aligned}
B &= a(\cos \omega \sin \Omega + \sin \omega \cos \Omega \cos i), & (3.27) \\
A &= a(\cos \omega \cos \Omega - \sin \omega \sin \Omega \cos i), & (3.28) \\
G &= a(-\sin \omega \sin \Omega + \cos \omega \cos \Omega \cos i), & (3.29) \\
F &= a(-\sin \omega \cos \Omega - \cos \omega \sin \Omega \cos i), & (3.30)
\end{aligned}
$$

where a is the semimajor axis, Ω is the longitude of the ascending node, i is the inclination of the orbit plane to the plane tangent to the sky and ω is the argument of periastron. It should be noted that this can be the orbit coordinates for either the parent star or its companion around the barycenter, depending on which semi-major axis is taken; the ω in the respective orbits differ by 180°. We measure the star orbit, so the coordinates of interest are $\Delta x_s, \Delta y_s$, obtained by taking $a = a_s$.

A more practical expression for the apparent orbit displacements is given by

$$\Delta\xi = \alpha Q_\alpha, \tag{3.31}$$

$$\Delta\eta = \alpha Q_\delta, \tag{3.32}$$

where α is the semimajor axis expressed in milliseconds of arc (mas), and Q_α and Q_δ are the orbit factors, which are analogous to the parallax factors (KAMP, 1967). These can be calculated through the following:

$$Q_\alpha = B'x + G'y, \tag{3.33}$$

$$Q_\delta = A'x + F'y, \tag{3.34}$$

where the factors indicated with the prime symbol are related to the Thiele-Innes constants as follows:

$$B' = -B/a, \quad G' = -G/a, \tag{3.35}$$

$$A' = -A/a, \quad F' = -F/a. \tag{3.36}$$

The semimajor axis in angular measure and in linear measure are related through the following expression:

$$a(\mathtt{AU}) = \frac{\alpha(\mathtt{mas})}{\pi_{abs}(\mathtt{mas})}. \tag{3.37}$$

If the observed star is a binary system, then the astrometric model of Equations 3.21 and 3.22 may incorporate Equations 3.31 and 3.32, providing the following model:

$$\xi = \xi_0 - \pi_{abs}P_\alpha - \mu_\alpha\Delta t - \alpha Q_\alpha, \tag{3.38}$$

$$\eta = \eta_0 - \pi_{abs}P_\delta - \mu_\delta\Delta t - \alpha Q_\delta. \tag{3.39}$$

3.5.3 Spectroscopy: Doppler Shift

In the spectroscopy experiment the quantity obtained from the measurements is the Radial Velocity (RV), which is the velocity of the star in the direction of the line of sight. The actual quantity measured is the Doppler shift of the spectra, which is related to the RV by the following expression:

$$v = c\frac{\Delta\lambda}{\lambda}, \tag{3.40}$$

with c the speed of light, $\Delta\lambda$ the shift in wavelength and λ the central wavelength at which the shift has been observed.

3.5.4 Spectroscopy: Radial Velocity for Keplerian Orbits

For systems containing only one companion, the radial velocity of the parent star's movement around the barycenter of the system is given by the first derivative of the radial component of its position. This is given by the projection of a Keplerian orbital velocity to observer's line of sight plus a constant systemic velocity Γ,

$$v = \Gamma + K[\cos(f + \omega) + e\cos\omega], \tag{3.41}$$

where ω is the argument of periastron, e is the eccentricity, K is the velocity semi-amplitude and f is the true anomaly. Ideally, Γ would provide a direct measure of the velocity of the entire system in the radial direction. However, for this work, we are only interested in velocity variations. Thus, in practice, the value of Γ absorbs all unaccounted for constants and does not reflect the actual velocity of the system.

The velocity semi-amplitude can also be written in terms of orbital elements,

$$K = \frac{2\pi}{P}\frac{a_s\sin i}{\sqrt{1 - e^2}}, \tag{3.42}$$

where i is the orbital inclination and a_s is the semi-major axis of the orbit of the star. Using the proportionality between the masses and semi-major axes, $a_b M_b = a_s M_s$, and Kepler's third law, we can rewrite Eq 3.42 as

$$\frac{M_b \sin i}{(M_b + M_s)^{2/3}} = \left(\frac{P}{2\pi G}\right)^{1/3} K\sqrt{1 - e^2}. \tag{3.43}$$

Note that we have introduced the indices s and b to distinguish between stellar and companion's parameters. Eq 3.43 provides a way to calculate the projected minimum mass $M_b \sin i$ of the companion with the assumption that there is a measurement of the stellar mass by other means (e.g. stellar atmospheric models). It is to be noted that this is a lower limit to the mass with the uncertainties mostly dominated by the determination of the stellar mass.

3.5.5 Spectroscopy: Multi-planet Keplerian RV Model

A system containing more than one companion results in a more complex orbital movement of the parent star around the barycenter. Strictly, this should be modeled using a full consideration of the N-body interactions in the system. However, for weak interacting companions, this orbital motion can be approximated by a linear sum of the Keplerian contribution from each companion j, producing a total RV perturbation given by

$$v_z = \Gamma + \sum_{j=1}^{N} K_j[\cos\left(f_j + \omega_j\right) + e_j \cos\omega_j], \tag{3.44}$$

where N is the number of companions in the system and the remaining parameters follow the same notation used in Equation 3.41.

3.5.6 Interferometry: Basics

In this section we discuss basic concepts to understand the principles behind an interferometric experiment. This discussion is based on Haniff (2007a), Haniff (2007b).

In observations of astronomical sources we are usually scarce of photons, hence we need to collect light using reflector or refractive lenses. The light is gathered and focused in order to obtain images. If one examines the resulting image of a point-like source, as seen by an unaberrated telescope with circular pupil, it is observed that light does not simply sum up, instead it presents a pattern of concentric rings, the Airy disk. This phenomenon occurs due to the interference between coherent electromagnetic waves (light) coming from the different points of the mirror/lens surface.

This pattern can be well described by the so-called spatial coherence function.

Now, if one uses an optical interferometer, which is composed of two (or more) optical telescopes that are far apart to collect light from the same source, and combine these two beams together, the result is a wave-like pattern, similar to that formed by a single dish optics. The difference here is that Airy disks are formed due to the circular shape of telescope mirrors, while the shape of an interferometer image pattern is determined by the slit. This technique known as interferometry is not in principle different than regular imaging, but on what concerns the observing techniques, data reduction and analysis it turns out to be very different.

The fundamental concept of interferometry for astronomy lies in answering the following question: what is the interferometric response (visibility) for a given source morphology? The source morphology is usually expressed by the source brightness distribution function, $I(\alpha, \beta)$, on the sky. The link between the brightness distribution and the response of an interferometer is the Cittert-Zernike theorem (HANIFF, 2007a), which states that for sources in the far field the normalized value of the spatial coherence or "visibility" function is equal to the Fourier transform of the normalized sky brightness distribution. This can be expressed mathematically as follows:

$$V_{r,norm}(u,v) = \frac{\int \int I(\alpha, \beta) e^{-2\pi i(u\alpha + v\beta)} d\alpha d\beta}{\int \int I(\alpha, \beta) d\alpha d\beta}, \tag{3.45}$$

where α and β are angular coordinates on the sky, u and v are spatial frequencies, or the coordinates in the reciprocal plane. Notice that spatial frequency (u, v) coordinates can be condensed into a vector, $\vec{f} = u\hat{u} + v\hat{v}$, where by convention component $\hat{u}$ points East and $\hat{v}$ points North. For each spatial frequency there is a corresponding baseline vector in the pupil, $\vec{B}$, those of which can be related in terms of the wavelength, λ, as follows

$$\vec{B} = \frac{0.648}{\pi} \lambda \vec{f}, \tag{3.46}$$

where the spatial frequency is in arcsec^{-1}, wavelength in μm and baseline in meters.

Equation 3.45 provides a way to obtain the coherence function (or visibility) from

the source brightness distribution. The reciprocal is also true, i.e. one can measure the coherence function in order to infer the brightness distribution, which is obtained by the inverse Fourier transform of Equation 3.45,

$$I_{norm}(\alpha, \beta) = \int_{-\infty}^{\infty} \int_{-\infty}^{\infty} V(u,v) e^{2\pi i(\alpha u + \beta u)} du dv. \qquad (3.47)$$

where $V(u,v)$ is the complex visibility function, which is normalized, thus $V(u,v) = \nu(u,v)/\nu(0,0)$, for $\nu(u,v)$ and $\nu(0,0)$ being complex visibility functions corresponding to $I(\alpha, \beta)$ and $I(0,0)$, respectively. In the next section we explain how to measure coherence functions in practice.

3.5.7 Interferometry: Measuring Visibility Functions

The way for measuring complex visibility functions in practice depends on which type of radiation is under study. For example, in the radio domain it is possible to measure directly the amplitudes and phases of the complex visibility function. However, for the optical domain (including infrared), the coherence time is extremely short, therefore it is still impossible to access these quantities directly. Instead the quantity to be measured is the squared visibility, which allows us to obtain the amplitude and phases indirectly. To grasp the idea of measuring visibilities in optical interferometry we refer to the Young's double slit experiment, where the intensity of a given point on the image plane is given by the modulus squared summation of the electric fields, E_1 and E_2, arriving from the two slits. This intensity is given by:

$$I = \langle |E_1|^2 \rangle + \langle |E_2|^2 \rangle + \langle 2|E_1||E_2| \cos \phi \rangle, \qquad (3.48)$$

where ϕ is the phase difference between the electric field components E_1 and E_2, and the angle brackets refers to the time average. The first two terms of Equation 3.48 are directly proportional to the square of visibility and can be directly measured from the intensity of the fringe pattern. The last term carries the oscillatory nature of the fringes. Therefore one can access phases of complex visibility functions from the light-dark modulation of fringe patterns. Notice that these phases are measured with respect to an offset of a whole fringe period.

The amplitude of visibility function can be obtained from the fringe contrast, also

known as "Michelson Visibility", which is given by:

$$V = \frac{I_{max} - I_{min}}{I_{max} + I_{min}}.$$ (3.49)

Therefore it is feasible to measure both amplitude and phases of the visibility (or coherence) functions with square-law detectors, like optical interferometers.

3.5.8 Interferometry: Visibility Model

From Equation 3.45 one can obtain the visibility from a brightness distribution of an observed source. The latter may be rather complex, thus resulting in a complex form for the visibility function. In practice interferometry presents a limitation when the (u, v) plane is not well sampled. The current optical interferometers have only a few elements, namely 2 to 3 telescopes. This implies in a very poor coverage of the (u, v) plane, therefore making it difficult to recover the true image of the source. There are techniques to increase the (u, v) coverage, such as by observing the same target at different sky positions (as the Earth rotates), or by observing within a range of wavelengths, but even though the coverage remains poor. Given this limitation, one usually needs to rely on very simple models that may provide conclusive results. Below we present a description of these models based on Berger & Segransan (2007).

The simplest model one can think of is a point-like source, for which the Fourier pair image/visibility model is given by:

$$
\begin{aligned}
I(\alpha, \beta) &= \delta(\alpha - \alpha_0, \beta - \beta_0), & (3.50) \\
V(u, v) &= e^{-2\pi i(u\alpha_0 + v\beta_0)}. & (3.51)
\end{aligned}
$$

This is an important model to use in the calibration of an interferometer. The response for an unresolved source, which is known to be punctual, is given by Equation 3.51. The model of a more complex brightness distribution may also be represented by a composition of point-like sources.

The other important models to consider here are the uniform and gaussian disk. These become useful when a given source is resolved by the interferometer. It is

common for calibrators since they are usually required to be bright sources in the visible, thus these are likely to be nearby stars. The gaussian disk model is given by:

$$I(\alpha, \beta) = \frac{1}{\Theta}\sqrt{\frac{4\ln 2}{\pi}}e^{-\frac{4\ln 2\rho^2}{\Theta^2}}, \tag{3.52}$$

$$V(u, v) = e^{-\frac{(\pi\Theta\sqrt{u^2+v^2})^2}{4\ln 2}}, \tag{3.53}$$

where Θ is the FWHM, and $\rho = \sqrt{\alpha^2 + \beta^2}$. The uniform disk model is given by:

$$I(\alpha, \beta) = \begin{cases} \frac{4}{\pi\Theta^2} & \text{if} \quad \rho \leq \Theta/2, \\ 0 & \text{if} \quad \rho > \Theta/2, \end{cases} \tag{3.54}$$

$$V(u, v) = 2\frac{J_1(\pi\Theta r)}{\pi\Theta r}, \tag{3.55}$$

where Θ is defined here as the disk diameter, $r = \sqrt{u^2 + v^2}$, and J_1 is the first order Bessel function.

3.5.9 Interferometry: Binary Model

Figure 3.2 shows a simple representation of the brightness distribution of a binary, like an exoplanet and its parent star. It also shows the astrometric binary parameters that we want to include in the visibility model.

The primary difference between the binary model and those shown in the last section is that the brightness distribution is no longer symmetric, what makes the visibility to be a complex function. This has another important consequence: the phase of the complex visibility function is no longer constant (zero or π). This allows us to obtain information about the source from models for either the phases ϕ or, if three or more baselines are used, the closure phase Φ. We discuss these models below.

The visibility model for a binary can be described as a composition of two sources, each represented by either a point-like or a disk model, as shown in the latter section.
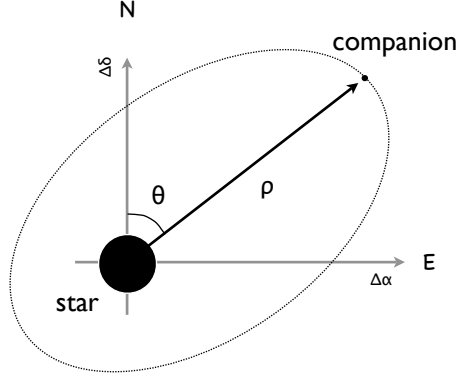
FIGURE 3.2 - Simple representation of the binary brightness distribution and the binary parameters.

This choice depends on the characteristics of the system in study.

The brightness distribution for a binary with two point-like sources is given by:

$$I(\alpha, \beta) = F_1 \delta(\alpha - \alpha_1, \beta - \beta_1) + F_2 \delta(\alpha - \alpha_2, \beta - \beta_2), \tag{3.56}$$

where (α_j, β_j) are the coordinates of component 'j', and F_j is the flux. In this case the visibility amplitude for each source is constant, but the corresponding visibility amplitude of the pair is not constant. This is given by the Fourier transform of Equation 3.56, which provides the unnormalized complex visibility,

$$\nu(u, v) = F_1 e^{2\pi i(u\alpha_1 + v\beta_1)} + F_2 e^{2\pi i(u\alpha_2 + v\beta_2])}. \tag{3.57}$$

The normalized squared visibility is then given by

$$|V(u, v)|^2 = \frac{\nu(u, v)\nu(u, v)^*}{|\nu(0, 0)|^2}, \tag{3.58}$$

which can be expanded to deliver the expression for the normalized squared visibility amplitude of a resolved binary pair with both unresolved components,

$$|V(u,v)|^2 = \frac{1 + f^2 + 2f \cos\left[(2\pi/\lambda)\vec{B}.\vec{\rho}\right]}{(1+f)^2}, \qquad (3.59)$$

where $f = F_2/F_1$ is the flux ratio, for the brightest component '1' at the center, $\vec{\rho}$ is the position vector of component '2' with respect to component '1' (primary). The projection of the baseline onto the position vector is given by $\vec{B}.\vec{\rho} = B\rho \cos(\theta - \theta_B)$. This introduces the astrometric binary parameters shown in Figure 3.2 into the visibility equation.

Equation 3.56 may not reflect the true brightness of the pair if any of the components are resolved. The more general expression for the complex visibility of a binary pair is given by:

$$V(u,v) = \frac{F_1 V_1(u,v)e^{2\pi i(u\alpha_1 + v\beta_1)} + F_2 V_2(u,v)e^{2\pi i(u\alpha_2 + v\beta_2)}}{F_1 + F_2}, \qquad (3.60)$$

where $V_j(u,v)$ is the normalized visibility for each individual component 'j'. One may introduce any visibility function for the components, such as the disk model.

For a system containing a faint companion (e.g. exoplanet or brown dwarf) around a star, for which the star visibility is V_*, the companion visibility is V_p, and the flux ratio is $f = F_p/F_*$, the squared visibility is given by:

$$|V(u,v)|^2 = \frac{V_*^2 + f^2 V_p^2 + 2f|V_*||V_p| \cos\left[(2\pi/\lambda)\vec{B}.\vec{\rho}\right]}{1 + f^2}. \qquad (3.61)$$

From Equation 3.61 we notice that if f is small, which is the case for a faint companion, the visibility reduces to the star's visibility. The precision required to measure such small flux ratios is what limits the current interferometers in detecting very faint companions. However, interferometric phases may present a detectable signal. The phase ϕ of a complex visibility function $V(u,v)$ is defined as follows

$$\tan\phi \equiv \frac{\mathrm{Im}V(u,v)}{\mathrm{Re}V(u,v)}. \qquad (3.62)$$

Therefore, one can write the phase model for a binary using Equation 3.60, which provides:

28

$$\tan \phi = \frac{fV_p \sin\left[(2\pi/\lambda)\vec{B}.\vec{\rho}\right]}{V_* + fV_p \cos\left[(2\pi/\lambda)\vec{B}.\vec{\rho}\right]}. \tag{3.63}$$

For small flux ratios except around the nulls one can approximate the above equation by:

$$\phi = \frac{fV_p \sin\left[(2\pi/\lambda)\vec{B}.\vec{\rho}\right]}{V_*} + n\pi, \tag{3.64}$$

where $n = 0$ if $V_* > 0$, and $n = 1$ if $V_* < 0$. We notice from Equation 3.64 that when the flux ratio is small, the phase is either equal to 0 or π, depending on the sign of the visibility of the star. However, at spatial frequencies where visibility becomes close to the flux ratio $V_* \sim f$, the phase assumes very different values. This happens at interferometric nulls of the star visibility function. If the baseline and wavelength are chosen adequately, then one could probe these regions and obtain information from the companion, even for very low values of flux ratio.

The closure phase (Φ), for an array with three elements, is defined as the sum of phases of the visibility component given by each pair of baselines, i.e.,

$$\Phi = \phi_{12} + \phi_{23} + \phi_{31}, \tag{3.65}$$

where each number represent a telescope. Therefore measuring Φ is equivalent to measuring three phases at the same time. The amplitude of the signal in this case depends on a combination of the three baseline orientations, which is given by the amplitude of the so-called bispectrum, which is defined as the triple product between the complex visibilities for the three baselines. The advantage of considering closure phases is that spurious atmospheric delays occurring on all baselines at the same time are automatically cancelled out when performing the summation in Equation 3.65. It means that, in principle, at least one of the sources of error that is normally present in phases, is being compensated when considering closure phases.

4 EXPERIMENTS DESIGN

In this chapter we describe the experimental set up and observing strategies for each of the following three experiments. 1. Doppler spectroscopy to obtain the Radial Velocities (RV). 2. Astrometry. 3. Infrared interferometry.

4.1 Optical Spectroscopy

4.1.1 The Experiment Overview

Spectroscopic measurements were carried out with the High Resolution Spectrograph (HRS) on the Hobby-Eberly Telescope (HET), McDonald Observatory, Texas, USA. Each target spectrum provides a measurement of the velocity of the star in the radial direction, which is obtained from the Doppler shift of the whole stellar spectrum with respect to some zero reference spectrum generated by a source situated at an inertial frame. We have used ThAr lamp emission spectrum produced in the laboratory as a first wavelength calibration reference. In order to improve the precision we have also used the iodine absorption cell method (BUTLER et al., 1996). In this method a low-pressure, temperature controlled cell with I_2 gas is positioned in the light path. The absorption of light by the I_2 gas produces a set of well known spectral features imprinted at the same time as the stellar spectrum. However they are produced with no wavelength shift with respect to the observatory frame. This provides a much better reference for wavelength calibration and also permit us to characterize the instrumental profile with great accuracy.

4.1.2 Goals

This experiment is aimed to provide a time-series of the HD 136118 radial velocity with higher cadence and better precision ($\lesssim 3\,\mathrm{m/s}$) than previous work (FISCHER et al., 2002). This enlarges the time coverage and improves the determination of the companion's orbit parameters. Also, it permits us to look for additional companions in the system. Apart from the results for HD 136118 we also aim to improve the reduction and analysis procedures, all of which are detailed in Chapters 5 and 6.

4.1.3 Instruments

Below we describe the technical details from the instruments used in our spectroscopic experiment. Most of this information has been obtained in the McDonald

Observatory webpage (http://www.as.utexas.edu/mcdonald).

4.1.3.1 HET

The Hobby-Eberly Telescope (HET) has been designed for spectroscopic survey work. It is a segmented mirror telescope with 91 Zerodur panels that provide a collecting area of $77.6\,\mathrm{m}^2$ and a filling factor of 98% (spherical), thus an effective aperture of $9\,\mathrm{m}$. Focal length is $13.1\,\mathrm{m}$. Its mounting has a fixed elevation axis at $37°$ zenith distance, prime focus tracker will follow objects when passing through the beam up to 1.5 hours. Azimuth is changeable by $360°$. HET site is at Ft. Davis (Latitude: $30°\,40'\,\mathrm{N}$. Longitude: $104°\,01'\,\mathrm{W}$. Elevation: $2240\,\mathrm{m}$), therefore all objects between declinations $-10°$ and $71°$ can be observed.

4.1.3.2 HRS

The HRS is an optical echelle spectrograph, which is detailed in Tull (1998). Figure 4.1 shows the HRS optical layout assembly. This instrument uses an R-4 (blaze angle of $75°$) echelle mosaic with cross-dispersing gratings to separate spectral orders. An all-refracting camera images onto a mosaic of two thinned and anti-reflection coated 2K x 4K Marconi CCDs with $15\,\mu\mathrm{m}$ pixels. The CCDs are abutted along their 4K side with a ~ 72 pixel dead space between them. This dead space is approximately parallel to the spectral orders. The HRS is a "white pupil" spectrograph using the 2-mirror collimator system pioneered by Hans Dekker and Bernard Delabre at ESO: Mirror M1, the main collimator, is an off-axis paraboloid used in auto-collimation, with the entrance slit at its focus. After the dispersed light is reflected from M1 the beam comes to an intermediate focus, offset from the slit by an amount controlled by the off-plane tilt of the echelle, which is $0.8°$. Mirror M2 has identical figure and focal length but is displaced off-axis by a distance equal to the separation of slit and intermediate focus. Resolving powers of $\mathrm{R} \sim 15,000$, 30,000, 60,000, and 120,000 are available by means of four effective slit widths. Spectral coverage is 420 - 1100 nm.

The parameters of the system are summarized in Figure 4.2, the HRS design parameters in Figure 4.3 and the HRS performance parameters in Figure 4.4.

4.1.4 Strategy and Observations

Our spectroscopic observations of HD 136118 included a total of 168 high resolution spectra, which were obtained between UT dates 2005 December 4 and 2008 May
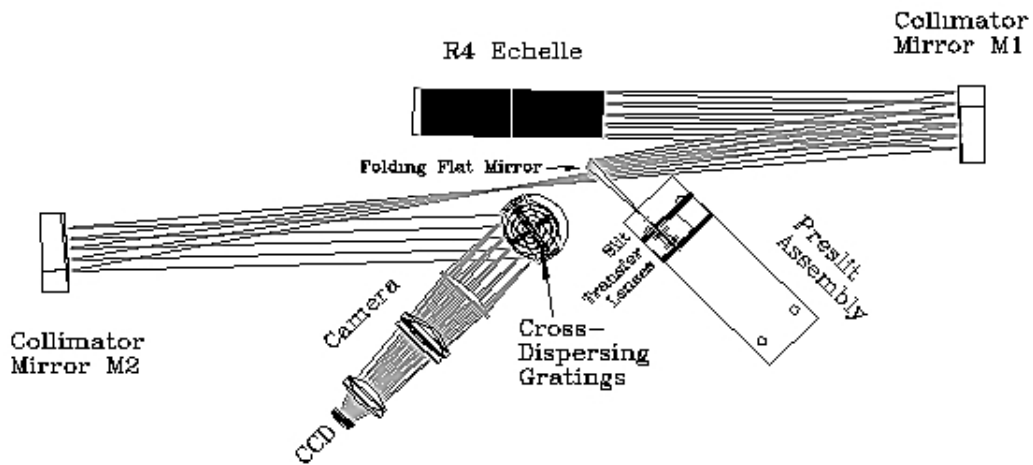
HRS Optical Layout

FIGURE 4.1 - HRS optical layout.

SOURCE: Tull (1998).

SCALE FACTORS FOR HET AND HRS		rgt 10/21/1999	scale.xls					
HET		**HRS**						
		Scale Factors[1]		**Resolving Power**				
Aperture, m	9.210	Blaze Angle deg.	75.07	**SlitWidth**		**Projected slit**		**Res Power**
Focal length, m	42.19	gr/mm	31.6056	µm	sec	mm	Pixels	R = λ/dλ
f/	4.581	Echelle WxL mm	210 | 836	500	1.00	125	8.3	30,003
Scale, "/mm	4.889	Rxφ arcsec	30,139	250	0.50	63	4.2	60,006
		Beam dia, m	0.179	125	0.25	31	2.1	120,012
Fiber Diameters		F Coll., m	2.000					
400 µm		f /	11.147					
1.96 sec		Slit scale, "/mm	2.009					
600 µm								
2.93 sec		F Cam., m	0.500					
Transfer Lenses		f /	2.79					
F1 (mm) =	30	CCD Scale, "/mm	8.036					
F2 (mm) =	73	CCD Pixel, µm	15 | 15					
Magnification =	2.433	CCD Size, pix	4096 | 4096					
[1] Based on magnification factor M=2.433 at the slit. Geometric projection factors, disregarding FRD.								

FIGURE 4.2 - HRS system parameters.

SOURCE: Tull (1998).

HRS Design Parameters

ELEMENT			Size	Blaze angle, etc.	Effective Blaze λ
R-4 Echelle		31.6 gr/mm	210x836	75.07°	"all"
Cross-Dispersing Grating	#1	316 gr/mm	204x254 mm	6.80°	610 nm m = 1
Cross-Dispersing Grating	#2	600 gr/mm	220x250 mm	9.53°	510 nm m=1
Collimator (off-axis parab.)	M1	f=2 m f/10	540x350 mm		
Collimator (off-axis parab.)	M2	f=2 m f/10	540x250 mm		
Refractive Camera		f= 0.5 m f/1.9	Aperture 28 cm	Field 88 mm	Pass-band 420-1100 nm
Star Fibers	#1	2.0"		400 µm	
	#2	3.0"		600 µm	
Image Dissectors*	#1	(7-Fiber	fiber	100 µm	
	#2	Bundles)	diameters	200 µm	
Image Detector		2 x (2048 x 4096 x15-µm) pixels EEV CCD Array **			

* Planned as a future upgrade of HRS.
** The gap between CCDs is approx. 1 mm, parallel to spectral orders.

FIGURE 4.3 - HRS design parameters.

SOURCE: Tull (1998).

HRS Performance Parameters

R x φ ***	30,000"					
Effective Slitwidth	1.00"	0.50"	0.25"			
	500 µm	250 µm	125 µm			
Resolving Power	8.3 pixels	4.2 pixels	2.1 pixels			
	30,000	60,000	120,000			
X-Grating	#1 (316 gr/mm)			#2 (600 gr/mm)		
Grating Tilt	27.5°	30.5°		31.5°	34.5°	37.5°
Spectral Coverage per CCD height	410-780 nm	710-1090 nm		420-620 nm	580-790 nm	740-950 nm
Order Separation @ λ	4.6" @ 420 nm	13" @ 700 nm	34" @ 1.1 µm	9.3" @ 420 nm	26" @ 700 nm	50" @ 940 nm

*** R = Resolving Power, φ = Slit width in arcseconds

FIGURE 4.4 - HRS performance parameters.

SOURCE: Tull (1998).

20. Multiple observations were taken most nights, so the velocities obtained on the same night may be combined, producing individual measurements of the stellar Radial Velocity (RV) at 61 different epochs.

The spectrograph was used in the $R = 60,000$ mode with a $316 \, \text{lines/mm}$ echelle grating. The position of the cross dispersion grating was chosen so that the central wavelength of the order that fell in the break between the two CCD chips was $5936 \, \text{Å}$. The temperature controlled cell containing low pressure iodine (I_2) gas was placed in front of the spectrograph slit entrance during all the exposures. The exposure times were nominally $120 \, \text{s}$, but were increased on a few nights due to bad seeing conditions. In addition to the program spectra we have also obtained HD 136118 template spectra. For these we removed the I_2 cell, the resolution was set to $R = 120,000$, and the exposure times were $230 \, \text{s}$.

Our RV data combined with previously published velocities from Lick Observatory (FISCHER et al., 2002) produces a total data set that spans $10.3 \, \text{yr}$. This corresponds to about 3 times the orbital period of the known companion, $P \sim 1190 \, \text{d}$.

4.2 Astrometry

4.2.1 The Experiment Overview

Astrometric measurements were obtained with the Fine Guidance Sensor 1r (FGS-1r) instrument aboard the *Hubble Space Telescope* (*HST*). As an interferometer working with a 2.4 m telescope in space, the FGS has a potential capability for measuring relative stellar positions with sub-millisecond of arc precision, with a dynamical range up to 12 magnitudes. The primary goal of this experiment was to obtain FGS-1r relative astrometry of stars with known radial velocity variations due to unseen low-mass companions. The FGS has the capability of measuring the reflex motion due to companions with planetary and brown dwarf masses at relatively wide orbits, with perturbation orbit size of order of $\alpha \gtrsim 0.5$ mas. Below we give an overview of the instrumental set up and strategies.

4.2.2 Instruments

4.2.2.1 *HST*

The *HST* is an optical space telescope that was deployed in low-Earth orbit by the crew of the space shuttle Discovery (STS-31) on 25 April 1990. Since then it has passed through four servicing missions for repairing and upgrading. These efforts are hoped to keep the telescope fully functioning at least until 2014 and perhaps longer.

The *HST* is a 2.4 m reflecting aplanatic Cassegrain telescope of Ritchey-Chrètien design. The collecting area is $4.5 \, \mathrm{m}^2$, and the focal length is 57.6 m. It weighs 11,110 kg, and is currently in a near-circular low-Earth orbit, at height 559 km, orbital period of 96 - 97 minutes, orbit velocity of 7,500 m/s, and acceleration due to gravity of $8.169 \, \mathrm{m/s}^2$.

It is equipped with six science instruments, which operate in ultraviolet, optical and infrared wavelengths. The instruments are the following:

NICMOS - infrared camera/spectrometer

ACS - optical survey camera (partially failed)

WFC3 - wide field optical camera

COS - ultraviolet spectrograph

STIS - optical spectrometer/camera

FGS - three fine guidance sensors

We are particularly interested in the FGSs, which we describe in more detail in the following section.

4.2.2.2 FGS

The FGS is a two-axis white-light optical interferometer aboard *HST*. A schematic view of its optical train is shown on Figure 4.5. This instrument has been designed to work as a guider for the Space Telescope, requiring a remarkable astrometric precision, which makes it suitable for scientific research as well.

The whole instrument has three FGSs operating at the same time, of which two (FGS2 and FGS3) are used for guiding. FGS1r is currently being used for science (before SM-4). A detailed description about the FGSs can be found in Nelan et al. (2010). Figure 4.6 shows a scheme of the field-of-view (FOV) of the three FGSs on the focal plane of the telescope.

Figure 4.7 shows the Koester prism, the device responsible for the interference of light collected by the telescope. The light coming outward from each side of the prism is focused by a lens into photomultiplier tubes (PMT-A and PMT-B). Their measured photon counts (A and B) can be combined by the following expression $S = (A - B)/(A + B)$, which gives the response of the interferometer. The read position can be changed by performing slight rotations on a secondary mirror, which is read by an encoder. Then the angles are translated to the telescope focal plane (pickle) coordinates (X or Y). This gives the position in one direction. The light beam is split into two identical prisms rotated by 90°, providing positions in two orthogonal directions. Astrometric measurements are made by scanning S over a range of positions. For example, the response $S(X \text{ or } Y)$ for a point-like source is given by the curve shown in Figure 4.6. This is the FGS interferometric fringe. Extended sources like resolved stellar disks or binary stars show different patterns for the S-curve. These can be modeled giving direct measurements of the light distribution of these objects. In our work we are particularly interested in highly accurate measurements of relative stellar positions in a field which only requires the measure-
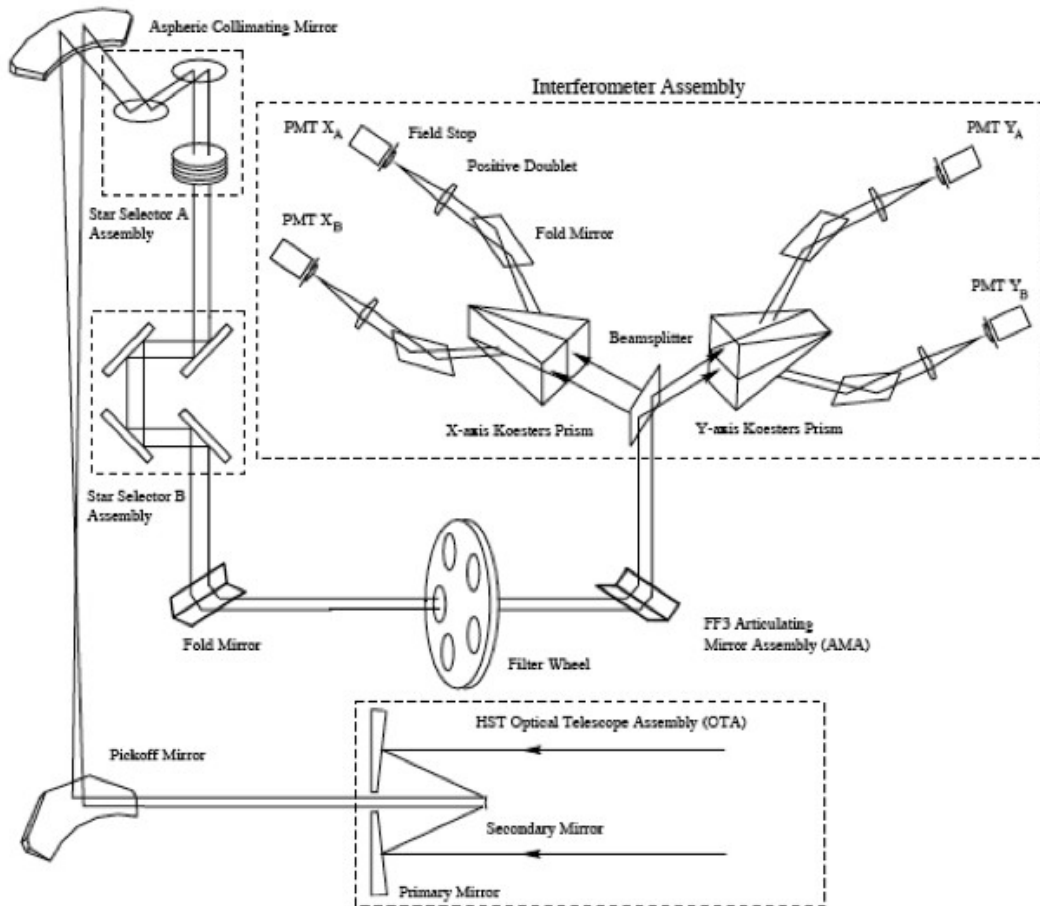
FIGURE 4.5 - FGS1r optical train schematic.

SOURCE: Nelan et al. (2010).

ment of the photo-center of each star (POSITION mode) and not the morphology of the entire S-curve (TRANSFER mode).

4.2.3 Strategy and Observations

HD136118 data were obtained with the FGS in fringe-tracking POSITION mode. A neutral density filter (F5ND) was applied when observing HD 136118 due to its brightness. For the reference stars we used the clear filter (F583W). All observations were secured under 2-gyro guiding, an operational mode dictated by gyro failures on *HST*. This mode results in major constraints on *HST* roll angle and observation dates. This restriction no longer applies since the last servicing mission (SM-4) has
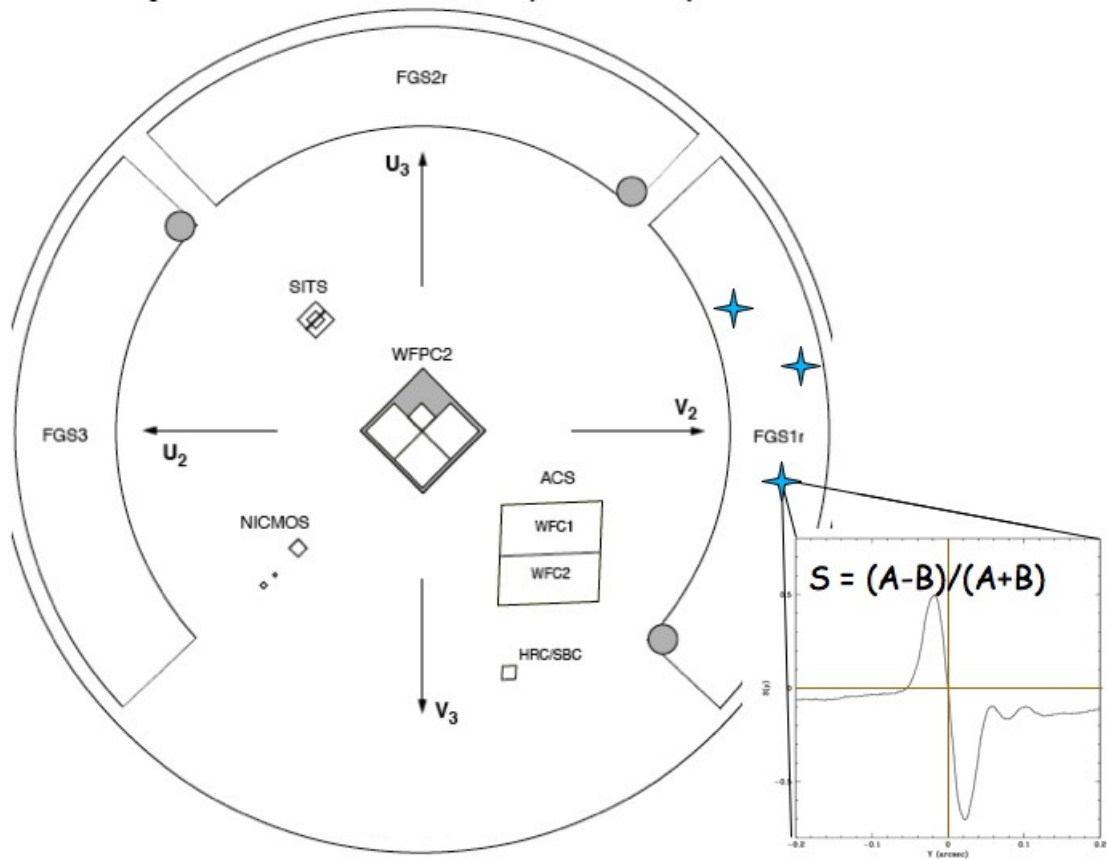
FIGURE 4.6 - Great circle: FGS field-of-view on the *HST* focal plane (projected onto the sky). Right panel: FGS-1r S-curve response for a point-like source.

SOURCE: Nelan et al. (2010).

replaced all the six gyroscopes.

The proposal was to obtain a group of observations (a group is six data sets = six orbits) at two epochs in Cycle 14 and one epoch in Cycle 15 to space the observations over a time span of about a year. Each group would be secured within two weeks. The HD 136118 field has a sufficient number of guide stars, and these guide stars are bright (V > 14.5). Thus, this target was relatively bullet-proof as regards two-gyro operations. Two-gyro operations had one scheduling consequence. Rather than acquire all three epochs within one Cycle, the two-gyro visibility windows required that we waited until a year after the first epoch to secure that last data sets (i.e., wait for the window of opportunity to roll around once again). Obviously the three-gyro mode would be preferable, because the parallactic ellipse would be better sampled.
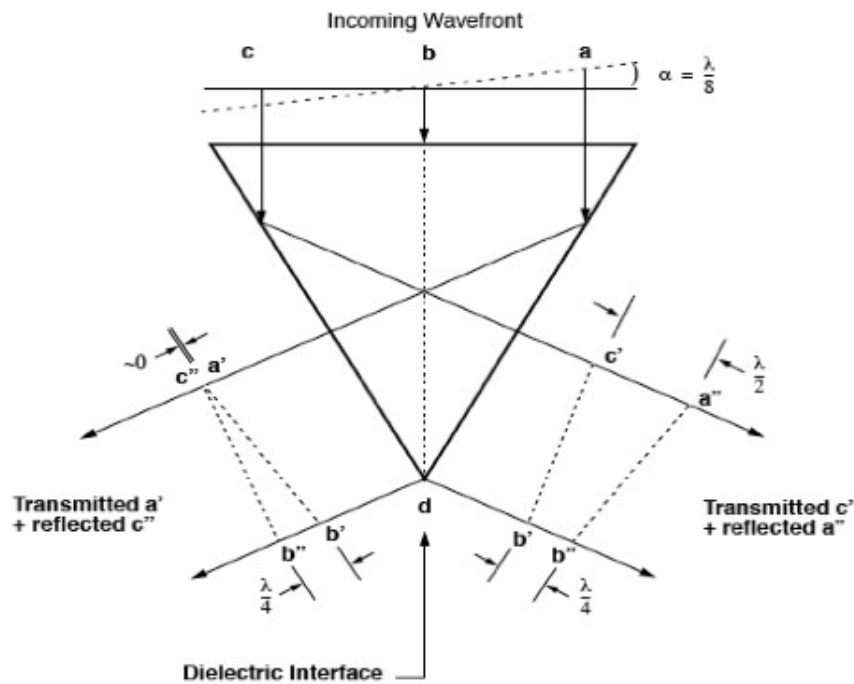
FIGURE 4.7 - Constructive and destructive interference in the Koester prism.

SOURCE: Nelan et al. (2010).

But, because we had an HIPPARCOS parallax in hand to use as Bayesian prior, two-gyro pointing control was adequate.

Table 4.1 shows the dates of observation, the number of measurements, N_{obs}, and the *HST* Roll angle for each visit to the HD 136118 field. Our data sets span 1.8 yr, covering about 55% of the HD 136118 b's orbital period.

TABLE 4.1 - Log of astrometric observations.

Epoch	Date	N_{obs}	HST Roll
1	2005/Jun/15	4	58.00
2	2005/Jun/16	4	58.00
3	2005/Jun/17	4	58.00
4	2005/Jun/18	4	58.00
5	2005/Jun/19	4	58.00
6	2005/Jun/24	4	59.10
7	2006/Mar/02	4	261.00
8	2006/Mar/10	4	264.17
9	2006/Mar/15	4	266.00
10	2006/Mar/22	4	269.15
11	2006/Apr/03	4	274.00
12	2006/Apr/07	4	280.41
13	2007/Mar/03	4	261.00
14	2007/Mar/09	4	263.67
15	2007/Mar/15	4	266.00
16	2007/Mar/24	4	269.74
17	2007/Apr/01	4	274.00
18	2007/Apr/08	4	280.70

4.3 Infrared Interferometry

4.3.1 The Experiment Overview

This experiment was meant to be a preliminary study of what we consider a promising technique to obtain information of high-contrast binaries, like brown dwarfs and exoplanet companions. Infrared interferometry in this context is still under development. For this reason, as it will be shown, it still presents a lot of open issues to be explored in future work.

Our interferometric measurements were carried out with the Astronomical Multi-BEam combineR (AMBER), instrument fed by the three 8.2 m Unit Telescopes (UTs) at the Very Large Telescope Interferometer (VLTI), Chile. In this experiment we obtained measurements of infrared low-resolution spectrally dispersed interferometric fringes of HD 33636, which is a solar type star with an RV-detected exoplanet candidate companion (see Chapter 2). HD 33636 has been observed in the same fashion as HD 136118, as part of the FGS/*HST* and HRS/HET observing programs. We have selected HD 33636 for the interferometric experience due to its larger companion mass, thus resulting in a lower contrast, easier to detect interferometrically.

4.3.2 Goals

The primary goal of this experiment was to obtain spectrally dispersed squared visibilities and interferometric phases for HD 33636 in a single quick observing run. The more specific objectives are outlined below.

- Confirm the mass and the orbital parameters of the lower mass companion to HD 33636.

- Investigate the visibility and differential phase signal in order to look for any spectral signatures of the companion.

- Demonstrate and evaluate the use of AMBER+FINITO+UTs to better characterize RV-detected low-mass companions.

- Validate our FGS astrometry results.

Some more general projected objectives of this experiment were:

- Once the use of AMBER+FINITO+UTs/ATs is established to obtain/estimate true mass, this method can be used to effectively filter out "true" exoplanet candidates for future astrometric programs like PRIMA and SIM.

- Some of these exoplanet companions may turn out to be brown dwarfs (true mass between $13\,M_J$ and $72\,M_J$). This will help us in a better understanding of the brown dwarf desert (if real).

4.3.3 Instruments

4.3.3.1 VLTI

The VLTI is one of the largest optical facilities for astronomy. Located on Cerro Paranal, Chile, it is a complex of four 8.2 m fixed Unit Telescopes (UTs) and another four movable 1.8 m Auxiliary Telescopes (ATs), all of which can be used in single mode observations or can be combined into two or three elements of an optical interferometer array. The six baselines spanned by the UTs ranges from 47 m to 130 m, while for the movable ATs it spans from 8 m to 202 m. The interferometric science instruments work primarily in the near- and mid-infrared wavelength. The four UTs are all equipped with the adaptive optics system MACAO (ARSENAULT et al., 2004).

4.3.3.2 AMBER

AMBER is a near-infrared, interferometric instrument, used to combine simultaneously the beam coming from up to 3 telescopes. A documentation of this instrument is found in the regularly updated user manuals published in the ESO/AMBER homepage, `http://www.eso.org/sci/facilities/paranal/instruments/amber/doc`, latest version by Merand et al. (2010). A much more detailed description of AMBER instrumental set up, data products and data reduction can be found in Petrov et al. (2007), Robbe-Dubois et al. (2007), and Tatulli et al. (2007).

To understand the basic idea of AMBER we present Figure 4.8, which shows a sketch of the AMBER instrument showing how the beam-combination is performed. Figure 4.9 presents an AMBER sample reconstituted image, using three telescopes, of a standard calibrator. Both Figures 4.8 and 4.9 have been obtained from Tatulli et al. (2007).

The entire light path inside AMBER is rather complex, nevertheless we summarize this process as follows. The beam coming from each telescope is split into the near infrared J, H and K fractions of the light. This is done with dichroic mirrors. Each beam is fed separately into a set of J, H and K single-mode optical fibers for the spatial filtering. The output light of each fiber set, corresponding to each telescope, is collimated and split into two portions, one for the ordinary channels (P1, P2 and P3) and another for the interferometric channel (IF), see Figures 4.8 and 4.9. The interferometric portions from all telescopes are focused into a common point, forming an Airy pattern that contains the interferometric fringes. The interferometrically combined beams, as well as the ordinary portions of each separate beam, enter a standard long-slit spectrograph that disperses the light vertically. The spectrograph can be set into three spectral resolutions: $R = 30$ (LR), $R = 1500$ (MR) and $R = 12000$ (HR). The wavelength coverage is $1 - 2.5\,\mu$m. Images are recorded by an infrared CCD detector. This description is, of course, over-simplified. We refer the reader to the literature for further details.
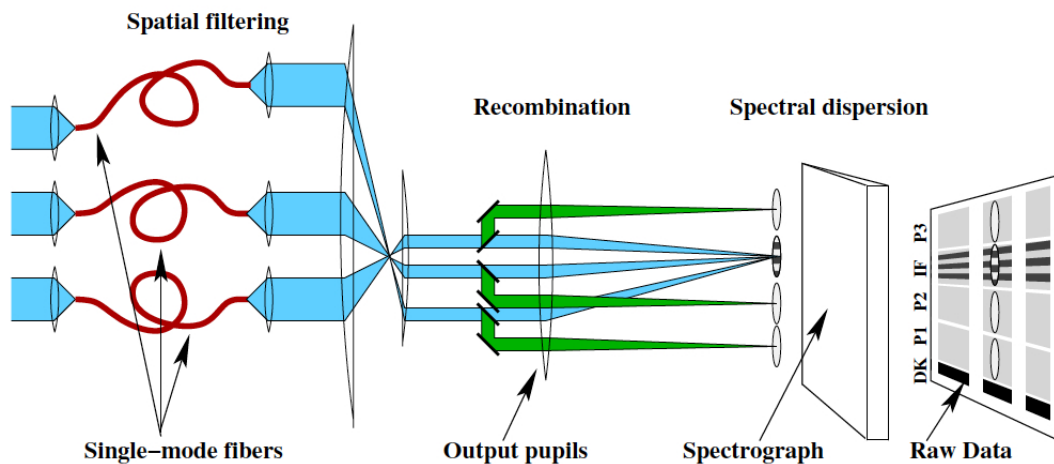
FIGURE 4.8 - Simplified optical setup of AMBER instrument.

SOURCE: Tatulli et al. (2007).

4.3.3.3 FINITO

The 2008 Science Verification (SV) run of AMBER was created in order to validate the Fringe-tracking Instrument of NIce and Torino (FINITO). FINITO is the first
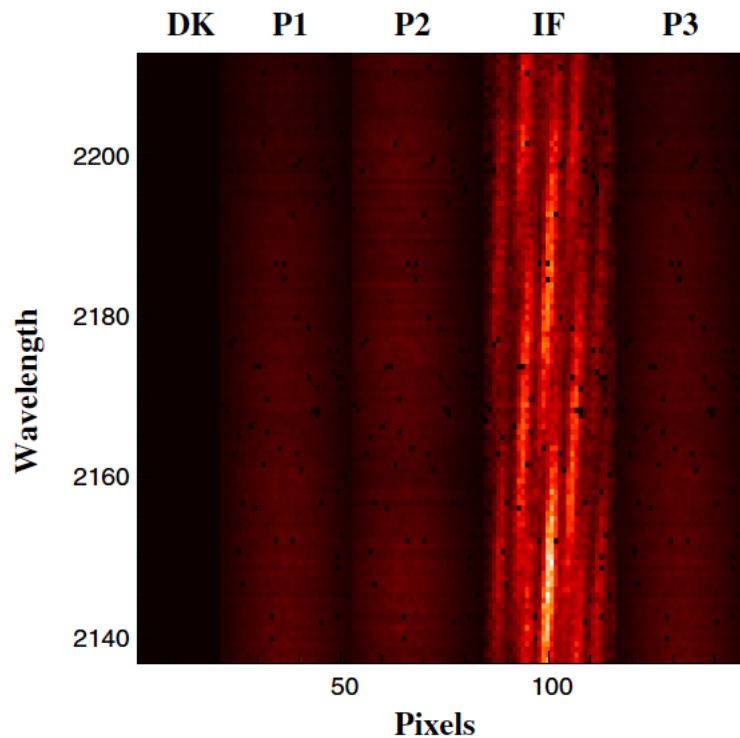
FIGURE 4.9 - AMBER sample image of an exposure of a calibration source. DK is the
dark channel, P1, P2 and P3 are the ordinary chanels from each telescope
and IF indicates the interferometric channel, where the fringe pattern is
recorded. The wavelength dispersion is on the vertical direction.

SOURCE: Tatulli et al. (2007).

generation VLTI fringe sensor. The basic idea behind FINITO is that interferometric
fringes are strongly affected by atmospheric variability. This causes blurring and
loss of fringe information for very short integration times, limiting interferometric
observations for only a few bright targets. Without FINITO any exposure time
longer than the atmospheric coherence time ($\sim 10\,\mathrm{ms}$) becomes impractical. The
task of FINITO is to operate as a fringe tracking unit that measures the optical
path difference variation along time, caused by atmospheric turbulence. This unit
uses interferograms produced by two combined telescope beams. Information is then
delivered to the delay line control loop, which performs slight mechanical corrections
that counteract atmospheric variations. FINITO increases the practical integration
time to a few hundred seconds, improving instrumental sensitivity by as much as
5 magnitudes. A more detailed description of FINITO is found in Corcione et al.
(2003), Gai et al. (2004).

4.3.4 Strategy and Observations

The interferometric observations of HD 33636 were obtained with U1, U2 and U4, using AMBER+FINITO in the Low Resolution (LR) mode. The observations have been carried out in UT 2008 Oct 14. The largest baseline used was the U1-U4, with 116 m. The seeing was around 1" at an airmass of ~ 1.2.

Our observing strategy was as simple as it is required for a typical SV run. We proposed to use the shortest practical telescope time that would provide any detectable information from the companion to HD 33636, or at least to set a limit of detection. We requested a total of 3 hours and 30 minutes of observations with AMBER+FINITO+UTs. According to the latest AMBER User Manual, it would take about 70 minutes to observe one calibrated visibility point with the UTs. We proposed 3 calibrated points, then it would take 3 x 70 min = 210 min = 3h30min. If three measurements were not possible we proposed to have a minimum of two pairs of Cal/Sci observations. Notice that one calibrated point means a pair of interferometric observations, comprising one point for the Science (Sci) object bracketed by two Calibrators (Cal). The actual observations provided us with 5 Sci sequential points and five useful sets, each containing 5 Cal sequential points in one night. Table 4.2 shows the log of interferometric observations.

Since our main goal was to measure absolute visibilities and perhaps absolute closure phases, we proposed to use the smallest Detector Integration Time (DIT) possible. In interferometry it is a major concern to have Cal observations as close as possible in space and time to the Sci observations. This requirement is important to guarantee that a minimum systematic error from the Optical Path Delay (OPD) is introduced due to the Earth rotation or to the difference in the observing direction. We discuss better this topic in the data analysis section.

TABLE 4.2 - Log of interferometric observations.

Set	Object	UT Date	Category
1	HD 19637	2008-10-14 05:42:14.224	Cal
1	HD 19637	2008-10-14 05:43:45.093	Cal
1	HD 19637	2008-10-14 05:45:15.374	Cal
1	HD 19637	2008-10-14 05:46:45.983	Cal
1	HD 19637	2008-10-14 05:48:16.336	Cal
2	HD 19637	2008-10-14 06:44:55.493	Cal
2	HD 19637	2008-10-14 06:46:26.107	Cal
2	HD 19637	2008-10-14 06:47:57.475	Cal
2	HD 19637	2008-10-14 06:49:27.920	Cal
2	HD 19637	2008-10-14 06:50:59.078	Cal
3	HD 33636	2008-10-14 07:11:28.056	Sci
3	HD 33636	2008-10-14 07:13:47.387	Sci
3	HD 33636	2008-10-14 07:16:06.996	Sci
3	HD 33636	2008-10-14 07:18:26.313	Sci
3	HD 33636	2008-10-14 07:20:46.033	Sci
4	HD 34137	2008-10-14 07:35:31.496	Cal
4	HD 34137	2008-10-14 07:37:53.126	Cal
4	HD 34137	2008-10-14 07:40:13.257	Cal
4	HD 34137	2008-10-14 07:42:33.701	Cal
4	HD 34137	2008-10-14 07:44:54.276	Cal
5	HD 34137	2008-10-14 08:00:32.489	Cal
5	HD 34137	2008-10-14 08:02:02.980	Cal
5	HD 34137	2008-10-14 08:03:33.305	Cal
5	HD 34137	2008-10-14 08:05:04.751	Cal
5	HD 34137	2008-10-14 08:06:35.237	Cal
6	HD 36134	2008-10-14 09:26:40.496	Cal
6	HD 36134	2008-10-14 09:28:10.942	Cal
6	HD 36134	2008-10-14 09:29:41.273	Cal
6	HD 36134	2008-10-14 09:31:11.962	Cal
6	HD 36134	2008-10-14 09:32:42.283	Cal

5 DATA REDUCTION

5.1 Optical Spectroscopy

5.1.1 Raw Data

The spectroscopic data arrive in standard FITS format. In each FITS file there are two images, one for each CCD chip. The longer wavelength part of the spectrum falls in CCD 1, which we also call the RED CCD. The shorter wavelength part falls in CCD 2, the BLUE CCD.

Below one can find a list of raw image files for a typical date of observation:

README.hrs	hrs620040.fits.Z	hrs620041.fits.Z
hrs620042.fits.Z	hrs620043.fits.Z	hrs620044.fits.Z
hrs620051.fits.Z	hrs620053.fits.Z	hrs620054.fits.Z
hrs620055.fits.Z	hrs620057.fits.Z	hrs620059.fits.Z
hrs620085.fits.Z	hrs620086.fits.Z	hrs620087.fits.Z
hrs620090.fits.Z	hrs620091.fits.Z	hrs620092.fits.Z

The files above are spectra of either the science target or the calibration, all of which are discriminated by their "OBSTYPE" keyword in the header. There can be basically six different types of files:

- ZERO - spectra taken with the shutter closed. There are normally a few of these images, so they can be combined in order to estimate the average zero-level in the CCD.

- FLAT - spectra of an incandescent light source. It is also usual to find many flat exposures for a date. These consist of bright and continuous spectra, which can be used in many steps of the reduction. For example, for calibrating the differences in pixel sensitivity, for finding the position of each spectral echelle order, and for measuring the global blaze illumination function.

- FLAT+I2 - spectrum of an incandescent light source with the iodine cell in the light path. There is usually just one exposure of this type. This is in fact an absorption spectra of the iodine gas, which is used for obtaining

49

the instrumental profile.

- ThAr - spectra of a Thorium-Argon lamp. This is an emission spectra that produces many well known features that can be used as wavelength calibrators.

- OBJECT - spectra of the science target. This type of image is not present in all dates. The reason for this is that the object is usually observed with the iodine cell in. Observations like this are made for obtaining object template spectra only. These are normally higher signal-to-noise images, and in some cases higher resolution.

- OBJECT+I2 - spectra of the science target with the iodine cell in the light path. There are usually a couple of images of this type, namely 1 to 3, depending on the weather conditions and the telescope time allocated for the project. These are typically lower signal-to-noise images, which provide the main scientific results, the wavelength shift of the stellar spectra with respect to the iodine spectra.

5.1.2 Data Reduction for Obtaining Radial Velocities

The HD 136118 and HD 33636 RV data presented in our analysis have been reduced using a pipeline written in IDL^{TM} (short for Interactive Data Language) which is detailed in Bean et al. (2007), hereafter Bean's Pipeline (BP). BP performs the CCD reduction and the optimal order extraction for all individual spectra using the REDUCE package (PISKUNOV; VALENTI, 2002). For measuring the radial velocities from the target spectra it uses an independent adaptation of the techniques described in Valenti et al. (1995) and Butler et al. (1996).

In order to understand the procedures involved in the reduction of these echelle spectral data, that aims to obtain radial velocities at the level of precision for detecting exoplanets, we have worked in an independent investigation of every step of reduction. Our procedures have been assembled in a pipeline called ASTROSPEC. The ASTROSPEC is under development and unfortunately it still lacks computational efficiency for reducing large amounts of data, as it is required. This still prevents us from comparing ASTROSPEC and BP results. Nevertheless, the ASTROSPEC reduction is discussed in detail below. It should be noted that our implementations are aimed to obtain efficient methods with least user interaction in the sense that

it could be run automatically. Some preliminary tests have been performed and the results are very encouraging.

5.1.3 The Automatized Pipeline for Spectra Reduction (ASTROSPEC Package)

As an attempt to develop a more efficient tool and also for learning the procedures and caveats involved in the reduction of spectroscopic data, we have developed an independent pipeline, the ASTROSPEC package, for the reduction of HRS data to obtain high-precision radial velocities. The main frame of this streamline is built in a C-shell script, which can be visualized from the chart in Figure 5.1.

Pipeline	Scripts	Codes	Required Files
	./pipeline.sh		
Preparation of Data	./HET_prep.sh	split_hrs_list, makelists, ccdproc, imcombine	Raw data, myprocfile, myprocfile_1, myprocfile_2
Pre-Processing	./prep_flat.sh ./prep_data.sh	clean_bright_strip, extract_flat, extract_blaze, imarith	Images split into CCD1 and CCD2: Master flats, bias-subtracted images, mask_1.fits, mask_2.fits
Optimal Extraction	./extract.sh	extract_sum	Reduced echelle spectra images (-bias, /flat, *mask)
Normalization	./normalize.sh	normspec_img, cleanspc, imcombine, imarith	OUTSPEC FITS images
λ-Calibration	./calibrate_wl.sh	wlcal_img	thar_ref.dat, guess.dat, thar_1.fits, thar_2.fits
Measure RV (Iodine method)	./get_rv.sh	get_rv	NORM_OUTSPEC images, I2_template.dat, obj_template.dat ord.cal files

FIGURE 5.1 - ASTROSPEC pipeline flowchart.

Below we provide the description of each step followed by ASTROSPEC.

5.1.3.1 Preparation of data

The preparation of data is the very first step in the reduction. The script for this stage is `HET_prep.sh`. This employs routines to organize images and give them the first treatment, like trimming and bias subtraction. Below we outline the main steps followed by `HET_prep.sh`.

- Split a raw image into two new images holding the same rootname and adding the suffixes '`_1.fits`' and '`_2.fits`', one for each CCD chip. Figure 5.2 shows a pair of images for a typical flat-field exposure.
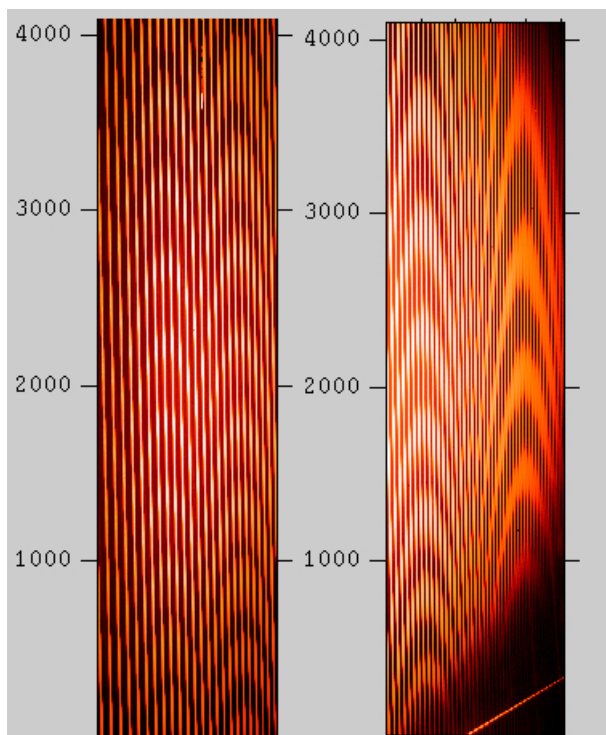
FIGURE 5.2 - Pair of a single flat-field exposure of echelle HRS spectra. The images are respectively the RED CCD (left) and BLUE CCD (right).

- Create a list of files for each observation type (OBSTYPE).

- Combine zero images (delete individual images) (`imcombine`).

- Subtract zero from all images (`CCDProc`).

- Combine flat-field images into a master frame, but do not discard the individual frames. (`imcombine`).

- Organize images into new directories. Figure 5.3 presents a scheme of the directory tree where ASTROSPEC is mounted.
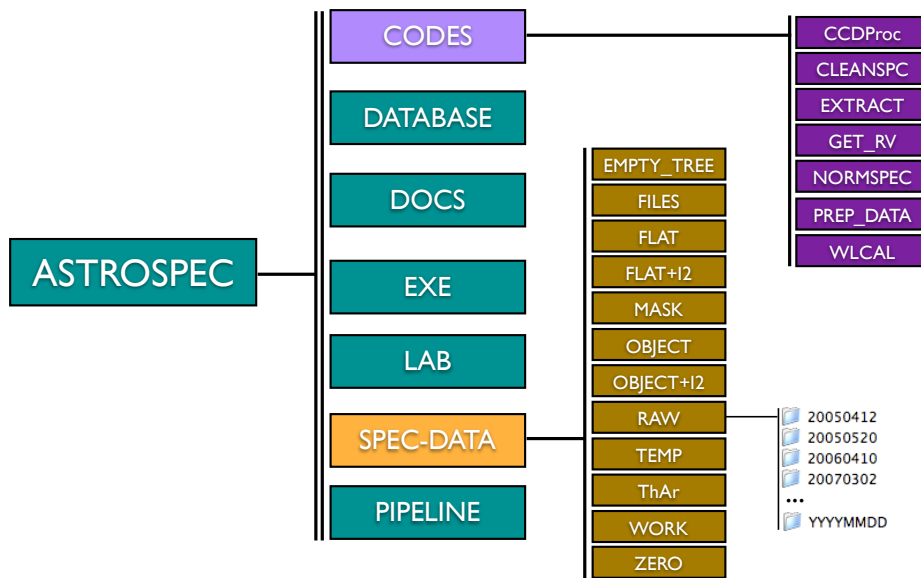
FIGURE 5.3 - Directory tree of ASTROSPEC.

5.1.3.2 Pre-processing

In the pre-processing phase we make use of flat-field images to obtain important calibrations, and these are used to apply the proper corrections to the data.

The three initial steps for the preparation of flat-field reducing tasks are performed within the script `prep_flat.sh` and are explained below.

- First the routine `clean_bright_strip` performs the cleaning of a bright nuisance feature appearing in the bottom of BLUE CCD flat images. This step is particularly important to avoid malfunctioning of the algorithm that automatically detects echelle orders.

- The routine `extract_flat` detects spectral orders and the regions within which signal is stronger than a given threshold. For these regions, the routine calculates the normalized pixel-by-pixel sensitivity variations. The space between orders with negligible signal is set to unit. This routine returns an output `date_flat_CCDNUM.fits` image. Figure 5.4 presents a sample piece of the normalized flat-field extracted with `extract_flat`.

- Finally the routine `extract_blaze` selects a set of points that represents the overall illumination (blaze) function. It fits a two-dimensional poly-
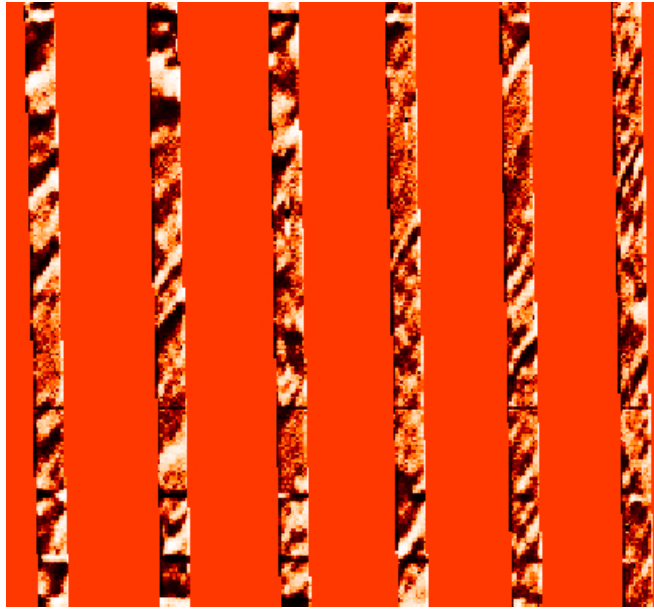
FIGURE 5.4 - Sample piece of a normalized flat-field.

nomial to these points and returns an output `date_blaze_CCDNUM.fits` image. Figure 5.5 presents a pair of blaze function images.

Once obtained the 'flat' and the 'blaze' functions, one needs to apply these corrections to the images. This is performed within the script `prep_data.sh`. It simply divides each object image by the normalized flat-field and by the blaze function. At the end of this stage it still permits one to apply masks to the data. Note that there is a directory "MASK" where one can find the mask images named `mask_1.fits` and `mask_2.fits`.

5.1.3.3 Extraction of Spectra

This is an important stage of the reduction process. In this stage the spectral echelle orders are extracted into N_o 1-D spectra, where N_o is the number of orders. The pipeline script for this is `extract.sh`, which runs the routine `extract_sum`. This routine detects order positions, enumerates orders, finds the useful area for extraction, and performs the extraction of spectra. The output is saved in the OUTSPEC image files.

The extraction algorithm calculates the sum of mean counts of pixels within a given interval along the dispersion direction. Namely, each flux point in the output spec-

54
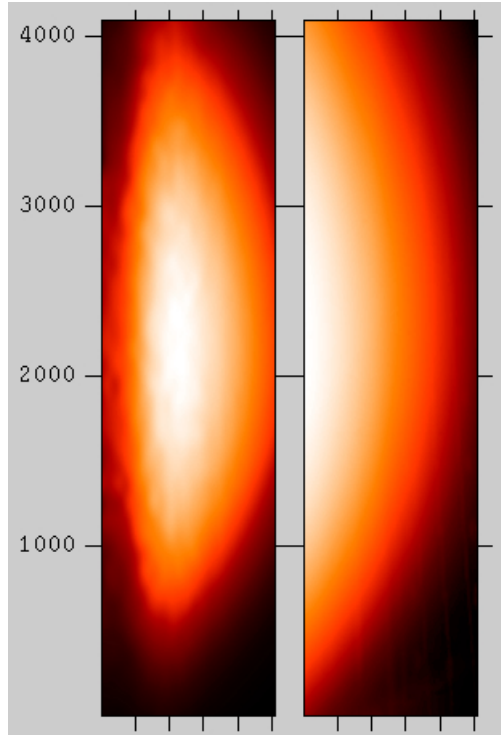
FIGURE 5.5 - Example of the blaze function for CCD 1 (left) and CCD 2 (right).

trum, f_j, for a given row j, is calculated by the following expression:

$$f_j = \sum_{i=i_0-N_s/2}^{i_0+N_s/2} \left(\sum_{j'=j-M_s/2}^{j+M_s/2} \frac{S_{ij'}}{M_s} \right), \tag{5.1}$$

where S_{ij} is the counts of a pixel at the detector position (i, j), with i being the column number and j the row number. i_0 is the column pixel at the photocenter of an order, N_s is the slit width (extraction aperture) in pixels, and M_s is the sample size, i.e. the number of neighbor pixels within which the average count is calculated. This operation is performed for each row, providing one point in the spectra. Figure 5.6 illustrates how this operation is performed.

As an example of the effects of parameter M_s in the extraction, in Figure 5.7 we present a piece of the spectrum of a given order. We show the extraction performed for 5 different values of M_s. Notice that larger values of M_s smooth out the spectrum but also make it less noisy. It seems that a low value of M_s, such as $M_s = 3$, is a reasonable choice.
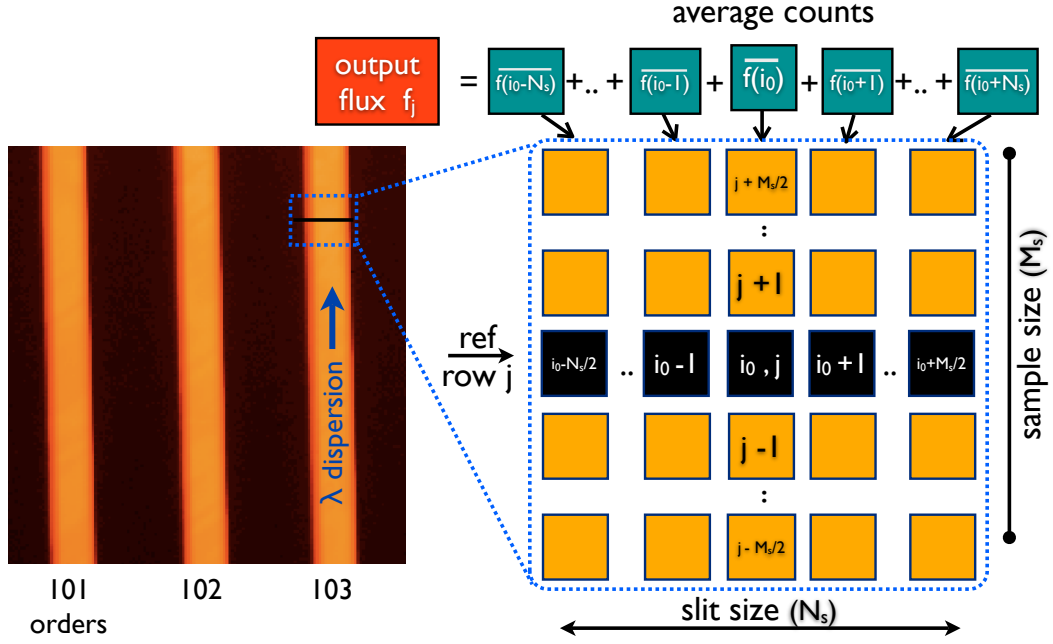
FIGURE 5.6 - Extraction scheme.

We have also inspected the effects of N_s in the quality of the extraction. Figure 5.8 presents a region of a given order, in which we have performed the extraction with 5 different aperture sizes, $N_s = 7, 9, 11, 13$, and 15. Notice that the depth of features increases for larger values of N_s, therefore the signal-to-noise ratio (SNR) is increased. On the other hand, the depth of features does not change significantly from $N_s = 13$ to 15. This means that after a certain limit value, as N_s increases, more pixels in the region between orders are included, thus adding more noise to the overall flux. Based on this we chose the value $N_s = 15$ for the slit aperture size.

A couple of other approaches have been tested for the extraction. The one presented here seems to be the most reliable so far. However, further improvements with alternative approaches may provide better results, specially on what concerns the detection and exclusion of bad pixels. In our approach the bad pixels are blindly included in the summation, and therefore they add noise to the spectra, or as in most of the cases they spoil the entire point evaluation, even though the majority of points bears valid information. One could use, for example, the deviation from the mean to estimate whether a pixel is an outlier, and then it could be replaced by a simple interpolation. This approach has not been tested yet, but may be explored in future research.
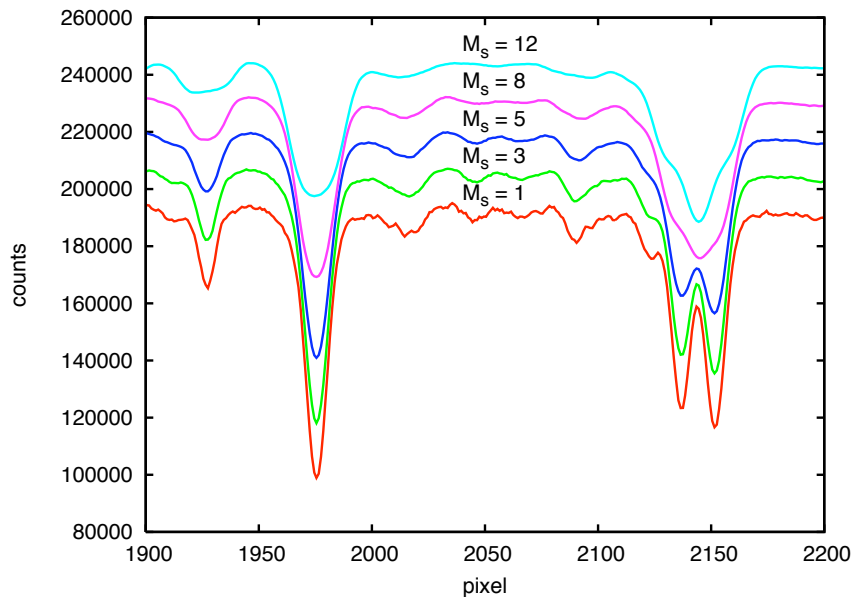
FIGURE 5.7 - A sample piece of an extracted spectrum where it has been adopted 5 different values for the sample size, $M_s = 1, 3, 5, 8$, and 12. Each spectrum was shifted for the better visualization.

5.1.3.4 Normalization

Each one-dimensional spectrum needs to be calibrated both in flux and wavelength. This section deals with the flux calibration. For the scientific goals of our experiment it is not important to perform an absolute calibration of the flux. The quantity to be measured, the wavelength shift, depends exclusively on the measurement of narrow absorption features in the spectra. Therefore the entire continuum flux emission may be identified and removed. The identification of this continuum envelope is the bulk idea of the normalization algorithm, which will be explained below.

The script to perform the normalization is `normalize.sh`, which runs two routines, `cleanspc` and `normspec_img`, iteratively.

The `cleanspc` identifies and cleans out spurious features like cosmic rays and hot pixels. The outliers are replaced by a local interpolation.

The `normspec_img` reads a spectrum row from the OUTSPEC file, then it searches
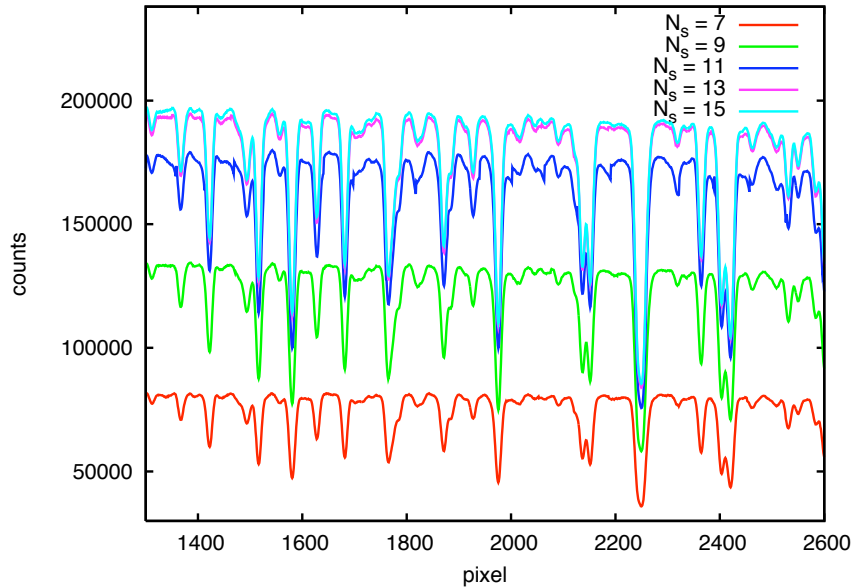
FIGURE 5.8 - A sample piece of an extracted spectrum where it has been adopted 5 different values for the aperture size, $N_s = 7, 9, 11, 13$, and 15.

for maximum points that better describe the overall shape of the continuum. Either a spline or a polynomial function is fit to these points. All data points are normalized by the fitted curve. This routine has firstly been designed to be used on absorption spectra, however it has already been adapted to normalize emission spectra. The latter may be used to extract scattered light and to change the scale of an emission spectrum.

The automatic search for maximum points is the key point of this program. This step is particularly important because it provides the source of data points to feed the fitting algorithms. Therefore this should represent very well the shape of the continuum function. This continuum is not necessarily the continuum emission, but a combination of any (may be many) low frequency information imprinted along with the spectra. We link below the steps followed by the program to search for the maximum points:

1. Read spectra data.

2. Set a box with n_b data points, where n_b is an input parameter of `normspec_img`.

3. Perform a robust linear fit in a box containing $3 \times n_b$ points. Move n_b points forward and perform another fitting. Move again and so on until the end of data points. The last box may contain less than $3 \times n_b$ points, therefore it takes all remaining data points plus the necessary amount of points before them to complete $3 \times n_b$ points.

4. Calculate the standard deviation (σ) of residuals from the fit line inside each box of n_b points. The first and second boxes make use of the same fit line. The last box and the one before also use the same fit line.

5. Select points lying at less than 1σ away from the fit line. Outlier points have their values replaced by a simulated data following a normal distribution with mean lying on the fit line and with dispersion σ. Then perform again a robust fit of a line to these points.

6. Find five maximum positive deviations from the fit line inside each box containing n_b points.

7. Choose the maximum that better represents the upper level to normalize the spectrum. The five maximum points found in step 6 are evaluated. If the higher maximum is lower than $3 \times \sigma$, then assume this and discard the other four. However if it is greater than $3 \times \sigma$, tests the second maximum, and so on until the fifth point. Finally if the fifth point did not pass the condition, then it assumes the level as equal to $3 \times \sigma$ above the fit line.

8. Reset all fit lines to their respective upper level (fit line + maxpoint). Where maxpoint is chosen in step 7.

9. Calculate the average of each fit line inside each box. This provides one global maximum for each box.

10. Export max dataset to the fitting routines. The fit can be either polynomial using a Levenberg-Marquardt minimization algorithm or a third order spline interpolation.

Figure 5.9 shows an example of a spectral order, the continuum envelope found by the `normspec_img` algorithm and a spline interpolation through these points. Figure 5.10 presents the normalized spectrum, now with relative fluxes scaled between [0,1].
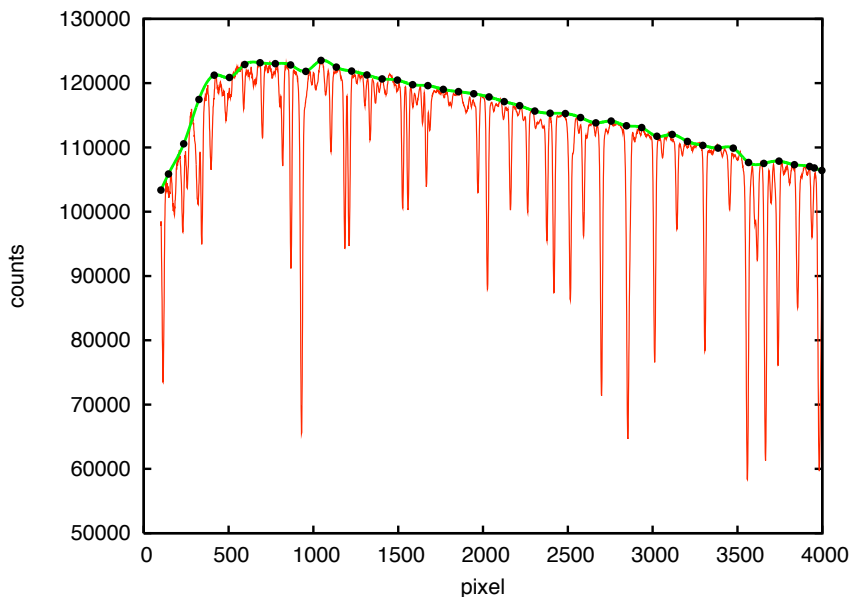
FIGURE 5.9 - Example of the normalization of a given spectral order. The full circles represent the maximum points found by the normalization algorithm, the green line represents the spline interpolation through the maximum points. The spectrum is shown in red.

Figure 5.11 presents the HD 136118 OUTSPEC images containing the calibrated spectra for both CCD chips.

5.1.3.5 Wavelength Calibration (Th-Ar)

The wavelength calibration is of chief importance for the determination of radial velocities. This section deals with the initial calibration using Th-Ar emission lines as the reference standards. Further refinement in the calibration will be made using the Iodine method, however the results in the latter strongly depend on a fine previous calibration. For this reason we have been careful in this stage. Below we describe the methods employed for the wavelength calibration.
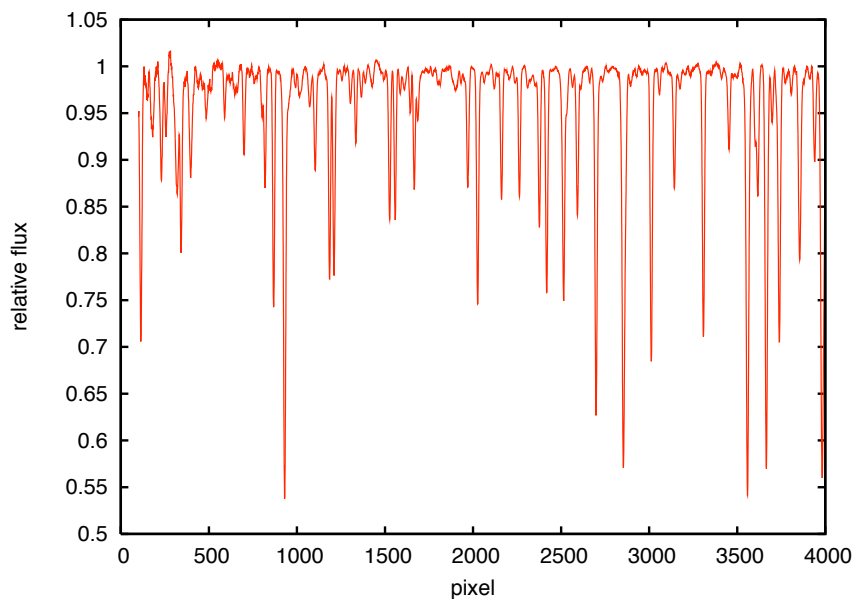
FIGURE 5.10 - Normalized spectrum after running `normspec_img`.
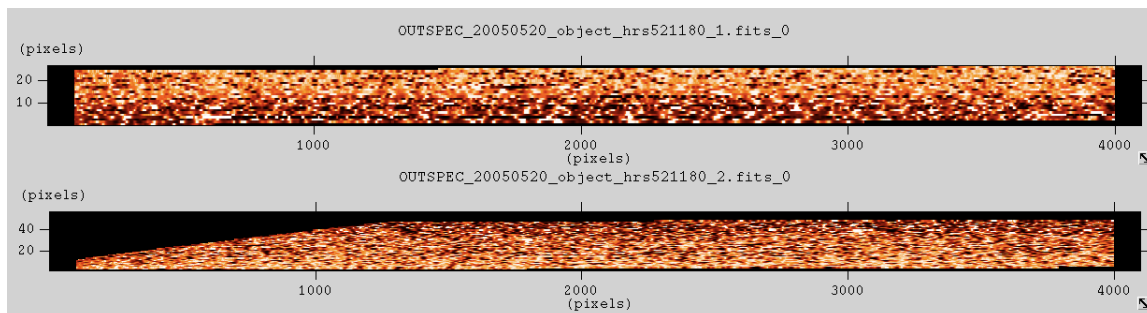
FIGURE 5.11 - OUTSPEC normalized spectral images of HD 136118 for both the RED CCD (top) and the BLUE CCD (bottom).

The script for this stage is `calibrate_wl.sh`, which runs the routine `wlcal_img`. This will delivery a set of calibration files, one for each order. Each of these files is named with the order number and the extension '`.cal`', for example the order 101 will delivery the file '`101.cal`'. The algorithm to perform the calibration is described below:

1. Read the following data files: a) Th-Ar OUTSPEC normalized spectra file

61

obtained at the same conditions as the program spectra. b) Program OUT-SPEC normalized spectra file. c) File `guess.dat`, which contains a list of positions of Th-Ar lines in units of pixel and the correspondent wavelength. d) A full catalogue of Th-Ar lines, `thar_ref.dat` (LOVIS; PEPE, 2007).

2. Get rid of saturated spectral lines. It firstly uses the `trace_ord` algorithm (which is the same used to find echelle spectral orders). The threshold must be very high, so it will only detect very broad and strong features, which are characteristic of saturated lines. Then it fits a Gaussian profile to the line. This is obviously not the best model, but is enough to place a scale within which the feature will be deleted. We have used 10 times the FWHM as the radius around the center, which places a boundary within which the feature is cut off. The cut itself is done by replacing the flux with zero.

3. GUESS FIT - In this step it reads the line positions in the `guess.dat` file and performs a Gaussian fit to each of these lines in the observed Th-Ar spectrum. The fit positions (in pixels) against the predicted positions (in wavelength) provide the data for the first calibration model.

4. POLY FIT - Fits a polynomial function to the line positions. The fitting is tested with several polynomial orders, varying from 1 to 7. The one with lowest chi-square is selected.

5. Apply calibration to the observed Th-Ar spectrum.

6. With new calibrated data, a new fitting of line positions is performed. Now all features in `guess.dat` plus the features in the catalog file are taken.

7. The new fitted positions are stored and the statistical moments are calculated. Since some bad fitted lines are expected, an algorithm to filter out all features presenting parameters with high deviations ($> 3\sigma$) from the median is applied. It is worth to mention here that we do not use the regular definition of RMS. The reason is that outliers (always present) brings the RMS to an unrealistic value of the quality of our fitted lines. Instead we use the Root Median of Squared Residuals (RMSR), defined as follows; $\text{RMSR} = \sqrt{\texttt{Median}(\texttt{residuals}^2)}$.

8. Re-iterate from step 4 to refine the calibration.

Although the `wlcal_img` routine already has one built-in iteration it may be run iteratively with the same dataset. Previous calibration in the file `ord.cal` are searched, and additional calibration is added to the end of these files. Notice that the new calibration will only be added if it improves the fit. Below is an example of the contents of a typical calibration file for order 101, `101.cal`:

```
3   5993.87109375    0.03058147   -0.00000142
5    0.53082484     -0.02510870    0.00041834   -0.00000295   0.00000000746
```

The first integer number in each line tells the polynomial order and the remaining numbers in the line are the coefficients derived in the fit.

Figure 5.12 shows the entire Th-Ar observed spectrum displaying all orders together after calibrated using `wlcal_img`. Figure 5.13 presents a piece of the calibrated Th-Ar spectrum showing two orders, 115 and 116, and the reference Th-Ar spectrum (LOVIS; PEPE, 2007) for comparison. Notice that each order has been calibrated independently and their overlay regions present a good agreement in the positions of Th-Ar lines.

5.1.3.6   Measuring Radial Velocities (Iodine Method)

The traditional way for obtaining radial velocities from stellar spectra is performed by first identifying spectral lines and then measuring their positional shifts, in units of wavelength. Since each spectrum may present many lines, the shifts are averaged and converted to velocities through Equation 3.40. We use a different approach, the iodine method (BUTLER et al., 1996), which is briefly described below.

The main idea of this method is to introduce a known source of spectral features that permits one to precisely calibrate the spectra. This idea was introduced by Campbell & Walker (1979), where they used the hydrogen fluoride (HF) gas as a source of calibrating features. The application of this method is better explained in Campbell et al. (1988). The HF presents the drawback of being a hazardous gas. We use the iodine (I_2) gas instead, which is introduced in a thermally controlled low pressure cell, positioned in the beam path of light collected by the telescope. To work well as wavelength calibrators these sources should contain a large quantity of well known absorption lines, and it is desirable that the gas is not contaminated with

63
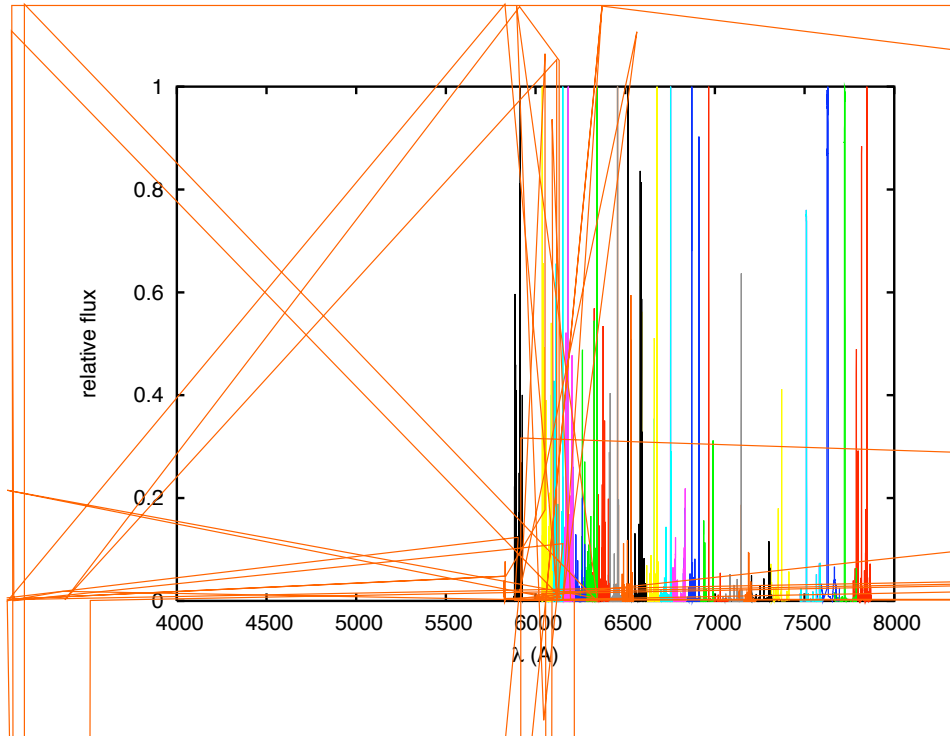
FIGURE 5.12 - Th-Ar entire calibrated spectrum.

other substances, which would produce additional nuisance features in the spectra. As a concern for practical application of this method, it should be noted that by introducing a substance in front of the beam path, a considerable amount of light is absorbed and wasted, thus more photons are needed in order to obtain the usual signal-to-noise ratio. This implies in limiting the method for bright sources, or the need for larger telescope apertures.

Below we discuss how to implement this method to obtain the radial velocities based on Butler et al. (1996).

TABLE 5.1 - Description of spectral data quantities.

Symbol	Source	Comment
I_{I_2}	flat $+$ I$_2$	Iodine transmission spectrum observed with an incandescent source of light (flat-field lamp).
I_{S+I_2}	object $+$ I$_2$	Object spectrum observed through the iodine cell.
T_{I_2}	I$_2$	Iodine template spectrum, e.g. Salami & Ross (2005).
I_S	object	Object template spectrum.

64
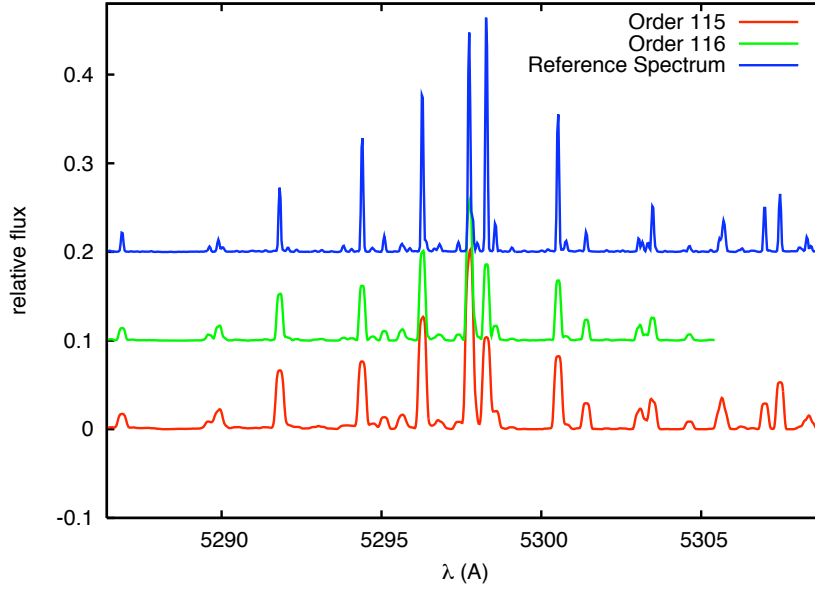
FIGURE 5.13 - Th-Ar calibrated spectrum for order 115 (red line) and 116 (green line), and the reference spectrum (blue line).

Table 5.1 presents the definition and description of each spectral data quantity to be used in the calibration process. These quantities can be related through the following expressions,

$$I_{I_2}(\lambda) = k_1 \left[T_{I_2}(\lambda) * \mathrm{IP} \right] + C_1, \tag{5.2}$$

$$I_{S+I_2}(\lambda) = k_2 \left[T_{I_2}(\lambda) I_S(\lambda + \Delta\lambda) * \mathrm{IP} \right] + C_2, \tag{5.3}$$

where we have introduced normalization and offset constants, k_1, k_2, C_1, C_2, and the Instrumental Profile, IP. The sign "$*$" represents convolution.

I_{I_2} and I_{S+I_2} can be directly observed every night, and T_{I_2} can be obtained from a catalogue. We have used the iodine template available in Salami & Ross (2005). The stellar template, I_S, is somewhat more difficult to obtain in the literature. Therefore, in order to obtain our own template, we have performed additional higher resolution

and better signal-to-noise observations of the target star without the iodine cell. The wavelength calibration of this template is performed in the same fashion, i.e. using the iodine method.

The method itself consists of modeling an IP function that better fits the observed data involved in Equation 5.2. This IP is used to "smudge" the iodine and stellar template spectra, in Equation 5.3. A wavelength shift, $\Delta\lambda$, is applied in the stellar template spectra, and the maximum correlation between the synthetic and observed spectra is searched.

Let us focus now on an important part of this method, the determination of the IP function. The IP is a transfer function that specifies how the instrument performs the smearing of sharp features. The blurring caused by the IP is a combination of many factors that we do not necessarily need to know in order to measure and use it. We make the assumption that it remains constant over the same region of the detector and over time during the same night of observation. The IP can essentially be measured from Equation 5.2, but this is not as simple as it seems since it involves an operation of deconvolution, which may be performed by means of many different numerical methods, each presenting pros and cons. Valenti et al. (1995) present two methods, a NonLinear Least Squares (NLLS), and the Singular Value Decomposition (SVD) method. They also mention a Fast Fourier Transform (FFT) method, which is not explored. Endl et al. (2000) presents a method based on the Maximum Entropy Deconvolution (MEM). As a first test for our pipeline we have chosen to use the NLLS method due to its simplicity. Below we discuss how this method has been implemented and the issues raised in the implementation.

The convolution operation in its integral form is given by the following:

$$I * F = \int_{-\infty}^{\infty} I(\lambda - \lambda')F(\lambda')d\lambda'. \tag{5.4}$$

In practice it is more convenient to apply this expression in the pixel space, represented here by the variable x, as presented in Valenti et al. (1995),

$$g(x) = \int_{-\infty}^{\infty} \phi(x - x')f(x')dx', \tag{5.5}$$

where $g(x)$ represents any observed spectrum, $f(x')$ the internal known function and $\phi(x - x')$ describes the IP. The normalization of $f(x')$ is preserved by requiring that

$$\int_{-\infty}^{\infty} \phi(x - x')dx' = 1. \tag{5.6}$$

Moreover Equation 5.5 can be rewritten in its discrete form

$$g_i = \sum_{j=qi}^{q(i+1)-1} \left(\sum_{j'=j-p}^{j+p} f_j \phi_{j-j'} \right), \tag{5.7}$$

where p is the number of pixels within which the function ϕ is considered, and q is the number of sub-pixels that fit inside an oversampled detector pixel. This oversampling operation is arbitrary, but is highly recommended, since the resolution of a template is usually better than an observed spectra. By limiting the sampling to the detector's sampling one would be losing template information, which may affect the measurement of the IP function.

The NLLS method requires the IP to be a parametric peak function. We use a normalized Gaussian profile with only one parameter, σ, to describe the IP. However, the IP does not necessarily need to be a symmetric function. In fact, the actual IP is often asymmetric as presented in Valenti et al. (1995), where they model the IP with a central Gaussian plus a sum of 4 to 10 satellite constrained Gaussians, which should account for eventual asymmetries in the real IP. We call attention to the fact that by adding additional weigh to one of the sides of an IP one could be introducing a bias in the measurement of the wavelength shift. Notice that the wavelength shift is obtained simultaneously with the IP parameters. In BP's pipeline it's adopted a similar approach as in Valenti et al. (1995). In ASTROSPEC we model the IP with a single Gaussian. Figure 5.14 presents the analytical IP modeled with multiple Gaussians obtained for a typical chunk, which demonstrates that by fitting multiple Gaussians one may introduce bias to the wavelength calibration. Another drawback is that the fitting process becomes much slower. Figure 5.15 presents a chunk of the observed iodine spectra, the iodine template, the model, and the residuals, which has a rms of 0.2%.

We built the routine `gen_template` to perform the wavelength calibration of a list
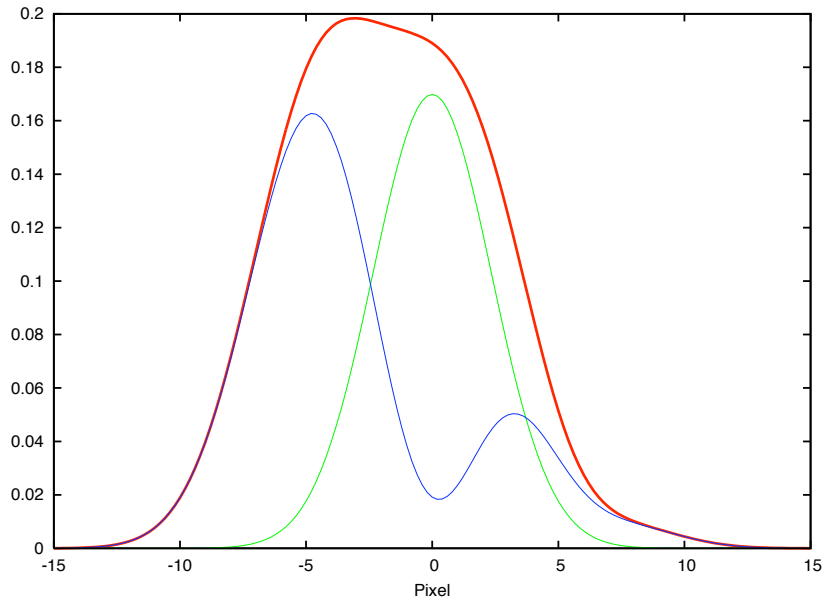
FIGURE 5.14 - Instrument Profile (IP) model (red). We have used a parameterized model comprising a central Gaussian (green) plus 10 satellite Gaussians (blue).
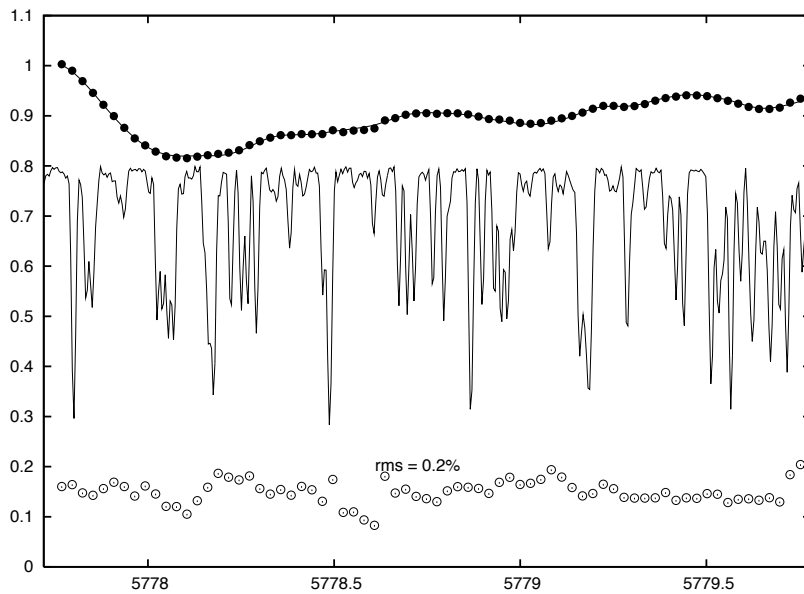
FIGURE 5.15 - Sample chunk 2 Å wide showing the template I_2 spectra (solid thin line), the observed flat+I_2 spectra (filled circles) and the fit model (solid line connecting solid circles), and ten times the residuals (open circles).

of spectra using the iodine method. This routine fits the model given by Equation 5.2 to the reference flat-field + iodine spectral data (I_{I_2}). The fit is not performed

for the entire order at once, rather it splits each order into chunks 3 Å wide. For each chunk it searches the wavelength shift and scaling factors that provide the best fit model (minimum χ^2). Hence the calibration is applied to the same region of all other spectra taken at the same night. This procedure is employed either to build the object template spectrum or to prepare the other spectra for extracting the radial velocities.

Finally the routine `get_rv` performs the last operation for obtaining the radial velocity, which is basically made in two-steps; first it calculates the cross-correlation between the flat+iodine spectrum obtained on the night of observation (I_{I_2}) and the flat+iodine spectrum used to calibrate the template (I'_{I_2}),

$$(I_{I_2} \otimes I'_{I_2})(\Delta\lambda_1) = \int_{-\infty}^{\infty} I_{I_2}(\lambda) I'_{I_2}(\lambda + \Delta\lambda_1) d\lambda. \tag{5.8}$$

The maximum correlation gives the instrumental delay, $\Delta\lambda_1$. This is a wavelength shift calibration, which may be caused, for example, by instrumental changes between the two dates of observation. The second step is similar to the latter, but now we calculate the cross-correlation between the observed object+iodine spectrum (I_{S+I_2}) and the product between the flat+iodine and the object template spectra, $I_{I_2} \times I_S$. Now the maximum correlation, i.e.,

$$\max\{[I_{S+I_2} \otimes (I_{I_2} \times I_S)](\Delta\lambda_2)\}, \tag{5.9}$$

gives the wavelength shift, $\Delta\lambda_2$, of the object spectrum with respect to the template date. We search for the maximum correlation by calculating the correlation for many shifts and then we fit a second order polynomial to find the maximum. The final calibrated wavelength shift is obtained by adding the two shifts,

$$\Delta\lambda = \Delta\lambda_1 + \Delta\lambda_2. \tag{5.10}$$

Hence the wavelength shift can be converted to velocity through Equation 3.40. The whole useful part of each spectrum provides hundreds of chunks, each of which provides an independent measurement of the velocity in the radial direction. On Figure 5.16 we present the radial velocity measured for more than 500 chunks. These

are absolute measurements obtained from 3 exposures from the object + iodine, and 3 exposures from the object only, thus it provides 9 independent measurements for each chunk.
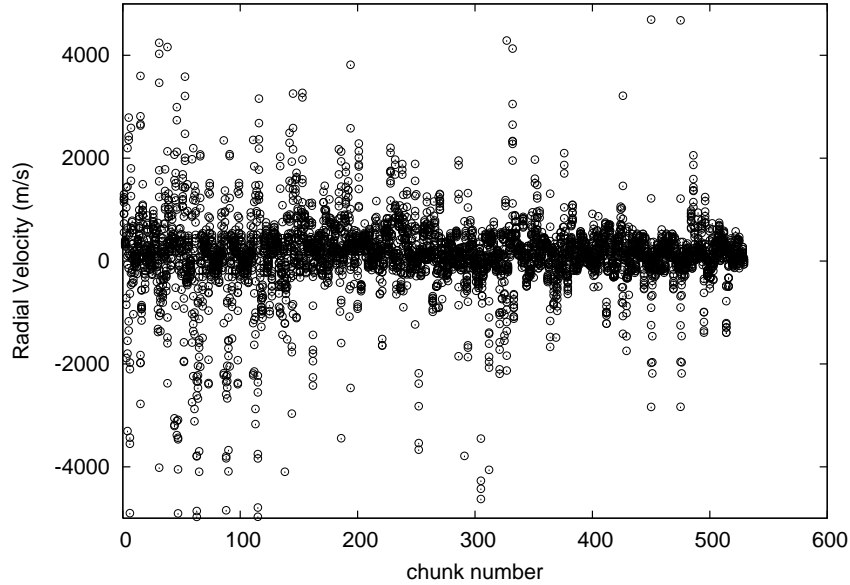
FIGURE 5.16 - Radial velocities measured from 530 chunks from the blue part of the spectra. These points include data from 3 HD 33636 + I_2 spectra and 3 HD 33636 template spectra for the same night.

Finally we can apply the statistics to obtain the central value for the radial velocity. First we adopted a robust method, which provides $\Delta v = 157.2 \pm 5.7\,\text{m/s}$. Then the regular average and standard deviation, which provide $\Delta v = 123 \pm 11\,\text{m/s}$. This result is outstanding since we obtained an error in the radial velocity that is comparable to the result obtained by BP's pipeline, and also that is sufficient for the detection of very low amplitude variations caused by exoplanets on their parent stars.

5.2 Astrometry

5.2.1 FGS Raw Data

FGS astrometry data obtained from the *HST* archive arrive in FITS format. These must be converted to GEIS (stands for Generic Edited Information Set) format before processing. As it was mentioned in Section 4, the FGS instrument is part of HST's pointing control system. Thus the contents of the FGS data are determined solely by the engineering telemetry format. Differently from other instruments, the FGS is linked to the HST engineering stream and not to the science instruments stream.

The data file rootnames follow the HST convention as appear in Shaw et al. (2009). For example in the name "fpppss01m", 'f' stands for the FGS instrument, 'ppp' and 'ss' correspond to the HST program ID and visit ID, '01' corresponds to the exposure number and 'm' corresponds to the source of transmission, which is in this case "merged real time and tape recorded". As an example, we have the following files that were generated by an exposure of a typical FGS observation:

- `f9d2320am_a1f.fits`, `f9d2320am_a2f.fits`, `f9d2320am_a3f.fits` - FITS data files, one for each FGS.

- `f9d2320am__cvt.dmh` - File containing scheduling and support data relevant to the observation.

- `f9d2320am.a1h`, `f9d2320am.a2h`, `f9d2320am.a3h`, `f9d2320am.a1d`, `f9d2320am.a2d`, `f9d2320am.a3d` - Data files converted to GEIS format.

Thus for each FGS observation a support file (extension `.dmh`) and three sets of GEIS files, one for each FGS (2,3 and 1r), are generated. Header files (ending with 'h') contain keywords that will help to interpret data files and the data files (ending with 'd') contain an instantaneous record of the following 19 quantities:

- PMTXA, PMTXB, PMTYA and PMTYB. These are the photon counts from the four photomultiplier tubes. They are stored in the groups 1 through 4.

- SSENCA and SSENCB. These are the values of the two star selector servo angles, stored in the groups 5 and 6.

- There are 13 status flags extracted from the engineering telemetry. Each of these flags can only assume binary values (1=ON and 0=OFF) and are stored in the same group 7.

Each group of data is not a single record of a quantity, rather it has a given number of samples of the observed quantity. The number of samples for each quantity is determined by the exposure time and by the sample frequency. The sample frequency is nominally 40 Hz for quantities in groups 1 through 6 and 6.67 Hz for quantities in group 7.

A more detailed and complete description of data formats and contents of FGS data files can be found in the FGS Data Handbook (NELAN et al., 2010) and in the *HST* Data Handbook (SHAW et al., 2009).

5.2.2 Calibration of FGS Data

In order to obtain high astrometric precision (~ 1 mas) with FGS it is absolutely necessary to perform a careful treatment of the data. In this section we briefly describe the standard data reduction procedures and give a bit more details on the non-standard procedures we used to calibrate our data. Note that the following procedures are only valid for observations in the Position Mode.

We can identify and correct for errors that arise in FGS Position Mode observations at three different levels:

1. **Observation Level** - errors associated with each individual FineLock acquisition and tracking sequence.

2. **Visit Level** - errors involved in constructing a virtual plate for a given FGS astrometric visit.

3. **Field Level** - errors that arise when comparing virtual plates of the same field taken during different visits.

For level 3, we use GaussFit (JEFFERYS et al., 1988) models, which will be described in Chapter 6. For levels 1 and 2 there are two pipeline processors, first `calfgsa` and then `calfgsb`, which are used to process the Position Mode data. Below we describe each of these processing tools.

1. `calfgsa`

   This is an IRAF task that performs the low level processing (conversion) to extract information of a single observation in a stand-alone fashion, i.e. ignoring other observations belonging to the same HST visit.

   `calfgsa` first reads raw GEIS files and inspect the flags and status bits (group 7) to determine if the observation was successful. Then it reads the encoder angles (groups 5 and 6) and the PMT counts (groups 1 - 4). These are used to compute the median centroid of each star in the Instantaneous Field of View (IFOV), for data obtained during the FineLock/Data Valid (FL/DV) interval (when the FGS was tracking the star's interferometric fringes). Data collected during the slew to the target is used to estimate the background contribution, which is subtracted from the PMT counts obtained for the target.

   Therefore, `calfgsa`'s task is basically to convert the raw telemetry encoder positions to instantaneous detector coordinates, (x, y), using a static set of parameters. The product from `calfgsa` is a file named as *rootname*`.tab`. This file contains (x, y) FGS coordinates of the centroid of the star's position in an exposure, along with data needed for further processing by `calfgsb`.

   All of these procedures are repeated for the identical time interval in all three FGSs (the astrometer and the two guiders).

2. `calfgsb`

   The processor `calfgsb` first reads TAB files from `calfgsa`. Then it applies two observation-level corrections, the LTSTAB and OFAD, which are better explained below.

   The conversion of raw telemetry encoder positions to instantaneous detector coordinates makes use of several parameters, such as the lever arm length, and offset angles, which are known to vary in time. These changes are monitored and updated multiple times a year by the Long Term Stability Monitor (LTSTAB) program. The corrections due to these changes are performed by the LTSTAB calibration, which is part of the `calfgsb` processor.

   The Optical Field of Angle Distortions (OFAD) are responsible for the largest source of error in reducing star positions from observations with

the FGS. This is an aberration of the optical telescope assembly and can be modeled by a two dimensional fifth order polynomial (JEFFERYS et al., 1994). The coefficients for this model are obtained through a self-calibration performed with observations of a selected star field in M35. These have been systematically measured and updated for many years. The description of the OFAD calibration and its previous analysis can be found in Jefferys et al. (1994), Whipple et al. (1995), McArthur et al. (1997), McArthur et al. (2002), and McArthur et al. (2005).

OFAD calibrations have been made upon observations in 1993, 1994, 1995 (for FGS 3), 2000, 2008 (for FGS-1r), and the LTSTAB have been performed between the OFAD calibrations to maintain the calibration. This is basically done by measuring scale-like changes. Notice that for this work we have used a non-published (2008) up to date OFAD calibration.

After performing the corrections above for all exposures, `calfgsb` starts the visit level processing. In this stage it will perform essentially two corrections, one based on the guide stars, which are those observed by the guiding FGSs, and another based on the check star, which is the one with more exposures observed by the astrometer FGS (in our case FGS-1r). The first is referred to as *dejittering* and the second as *drift corrections*.

– **De-jittering**. During a nominal visit, while the astrometer FGS sequentially measures the positions of the targets, the other two FGSs guide the telescope. They track the same guide star in FineLock. Therefore `calfgsb` uses the guide star data to remove effects due to spacecraft translation and roll differences between each exposure. The dejittering correction is normally very small ($\sim 1\,\mathrm{mas}$), but sometimes can get as high as $\sim 5\,\mathrm{mas}$.

– **Drift Corrections**. The astrometer FGS (in our case the FGS-1r) must observe at least two check stars (usually 4). The check stars are observed many times during the visit. These eventually drift across the FGS field-of-view. To remove this drift, `calfgsb` fits a low-order polynomial (linear, quadratic, or quadratic with rotation) to the check stars path along the visit. Since the exposures are executed sequentially, the drift correction may be removed from all exposures.

The output file produced by `calfgsb`, the "AST" file, will have the suffix '`_ast`'.

This file is in GaussFit ASCII table format, where the reduced astrometric positions and related information for all exposures are recorded.

Finally, the field-level corrections will take place. These are discussed in the following section. The analysis that involves field-level correction also involves the determination of some physical parameters, like the proper motion and parallax, therefore it will be treated in more detail only in Chapter 6.

5.2.3 Astrometric Reduction

We call this section as "Astrometric Reduction" because most of the procedures adopted here are the same used in classical astrometric reduction of conventional images. In fact the AST file permits to construct a virtual plate.

Three main calibrations should be taken into account in the field-level corrections:

- **Lateral Color** - color-dependent error in the measured positions.

- **Cross Filter Effect** - apparent change in the measured position as function of the filter selected for the observation.

- **Plate Constants** - scaling, rotation and offset constants to adjust all visit frames to the reference frame.

Besides these three corrections one should also model simultaneously the parallax and proper motion components for each object, as explained in Chapter 3. Therefore, given the positions (x', y') measured by FGS-1r we build a model that accounts for positional changes occurring systematically in all reference stars from date-to-date. This is accomplished by solving an overlapping plate model which includes scaling-rotation (C_1, C_2, C_3, C_4) and offset (D_1, D_2) constants, which are constrained to an arbitrary frame adopted as the reference (the constrained plate). This is the 6-parameter model, however in some cases, where the number of reference stars is not sufficient, one should opt for a 4-parameter model, with two scaling-rotation and two offset constants. Therefore the model is given by the standard coordinates of each visit:

$$\xi_0 = C_1 x' + C_2 y' + D_1, \tag{5.11}$$

$$\eta_0 = C_3 x' + C_4 y' + D_2. \tag{5.12}$$

Notice that the lateral color and cross filter effects have not been included yet. These corrections depend on the color and the difference in magnitude between the reference stars. The model that includes the lateral color and cross filter effects is also given by Equations 5.11 and 5.12, but with x' and y' given by

$$x' = x + lc_x(B - V) - \Delta XF_x, \tag{5.13}$$

$$y' = y + lc_y(B - V) - \Delta XF_y, \tag{5.14}$$

where x and y are the astrometer FGS coordinates, $(B - V)$ represents the color of each star, lc_x and lc_y are the lateral color corrections, ΔXF_x and ΔXF_y are the cross filter corrections in x and y. There are currently only two filters available that are supported by the OFAD calibration, the F5ND and the F583W. For fainter targets (V > 8), F583W is the recommended filter. For brighter targets (V < 8), F5ND filter is more appropriate. Therefore, whenever both filters are used in the same observing program, the cross filter correction should be performed.

Equations 5.11 and 5.12 can be replaced in Equations 3.38 and 3.39, forming the complete equations of condition. These comprise a set of two equations for each star and for each visit, all of which must be solved simultaneously. Since the field-level corrections have to be modeled together with some physical parameters, like the parallax, proper motion, and the perturbation orbit, we leave this discussion to the following chapter.

Note on the HST Roll Angle:

The plate constants should account for eventual field rotations among visits with respect to one reference plate. However, the *HST* has to spin around its own axis in order to provide the orientation for which the solar panels will collect the Sun light more effectively. Therefore, in some cases, the orientation of plates may become so

different that it messes up the minimization algorithms, which might get lost easily. In order to avoid this, one needs to rotate all plates to roughly the same orientation. The expression to rotate counterclockwise any given position (X, Y) in the FGS-1r frame to the (ξ, η) standard coordinates in the sky frame, is given by:

$$
\begin{aligned}
\xi &= X \cos(R) - Y \sin(R), &(5.15)\\
\eta &= X \sin(R) + Y \cos(R), &(5.16)
\end{aligned}
$$

where R is the relative angle between the FGS internal orientation and the spacecraft roll angle, `Roll`, given by $R_{FGS1r} = (\texttt{Roll} - 90°)$ (for FGS-1r) and $R_{FGS3} = (\texttt{Roll} - 270°)$ (for FGS-3). In order to rotate from a given frame i of a plate with roll angle R_i to the reference frame with roll angle R_0, one has to apply Equations 5.15 and 5.16, with $R = (R_i - R_0)$.

5.3 Infrared Interferometry

The processing of interferometric AMBER data is rather complex and it is not the scope of this work to deal with this here. We make use of available tools, all of which are well supported by the team of specialists from the European Southern Observatory (ESO) and affiliated organizations. The principles of interferometric reduction with AMBER/VLTI is fully described in Tatulli et al. (2007). Below we discuss in summary the pathway for obtaining the interferometric observables from AMBER raw data.

5.3.1 Reduction of the AMBER/VLTI Data

Raw interferometric data downloaded from the ESO server (http://archive.eso.org) are in FITS format. In order to reduce AMBER data one needs both the SCIENCE and CALIB category files. The SCIENCE files comprise the OBJECT (Sci), DARK, and SKY types. The CALIB files comprise OBJECT (Cal), DARK, SKY, and the maintenance files, which are given by the WAVE and 3P2V (or 2P2V for two-telescopes mode) types. These files together with the AMBER_BADPIX and AMBER_FLATFIELD files contain all information to allow AMDLIB processors to extract uncalibrated interferometric observables from scientific data. The latter two files are supported by the ESO engineering team and

can be downloaded from the ESO server.

AMDLIB is a package of C programs developed specifically to process AMBER data. The front-end program called GASGANO permits one to access and run the pipeline recipes from the AMDLIB library. Once GASGANO is set up it practically processes data itself. One just needs to load FITS files in GASGANO, inform which routine is to be used, and run the processor. More information about the AMDLIB recipes can be found in Duvert et al. (2008).

Figure 5.17 presents a snapshot of GASGANO window showing the HD 33636 Sci and Cal loaded data. The Cal data are interferometric exposures for the stars HD 19637, HD 34137, and HD 36134. Notice that besides the Sci/Cal (OBJECT) data, there are also DARK and SKY data, which are exposures taken right before and after every set of program exposures, which are needed for calibration.
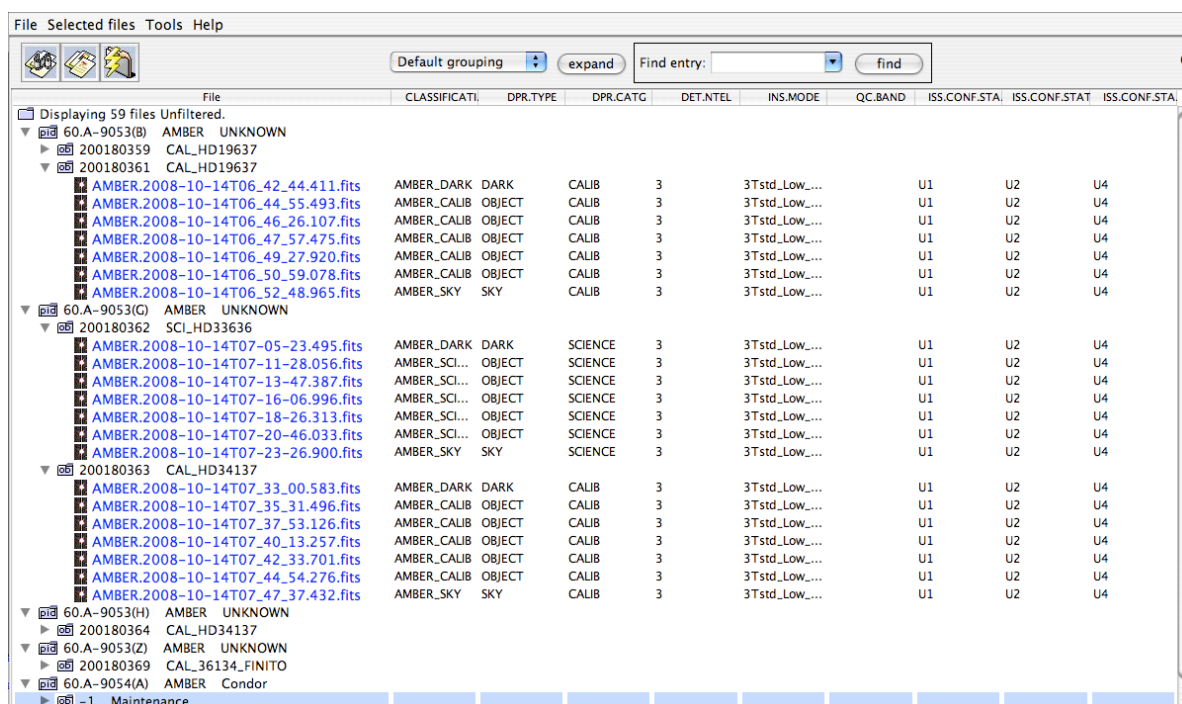
FIGURE 5.17 - Gasgano window showing the interferometric data.

To run the reduction pipeline one needs to select files used by the recipe, and go to menu Select Files ⇒ to recipe ⇒ Load recipe ⇒ "recipe name".

The first important AMBER pipeline recipe to be run is the "amber_p2vm", which is used to create a pixel to visibility matrix (TATULLI et al., 2007). To run this routine one needs to load AMBER files of the following six categories: AMBER_BADPIX, AMBER_FLATFIELD, AMBER_2P2V, AMBER_2WAVE, AMBER_3P2V, and AMBER_3WAVE. These are loaded in the "maintenance" group, as shown in Figure 5.18. The bad-pixel map and flat-field files are provided by ESO engineering support. The product of the amber_p2vm recipe is the P2VM file, which is used by the "amber_SciCal" routine.
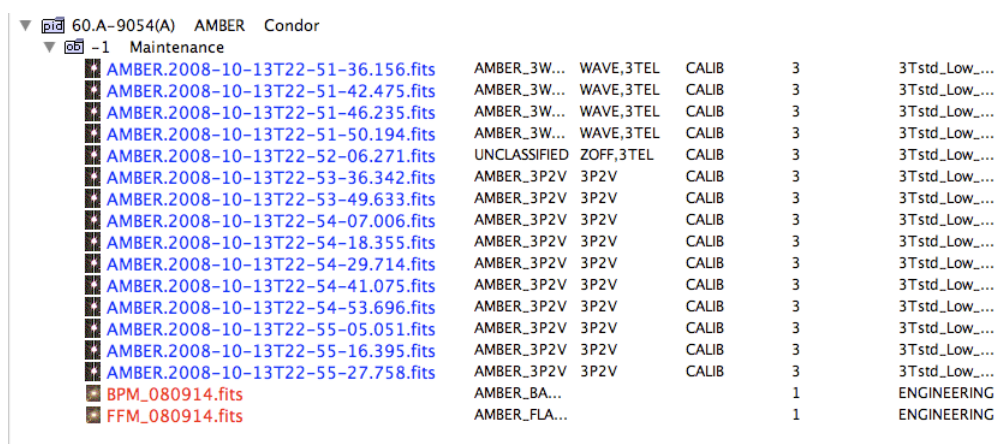
FIGURE 5.18 - Gasgano snapshot window showing the loaded maintenance files of the following categories: AMBER_2P2V, AMBER_2WAVE, AMBER_-3P2V, AMBER_3WAVE, AMBER_BADPIX, and AMBER_FLAT-FIELD. These data are used by routine "amber_p2vm".

The AMBER pipeline recipe "amber_SciCal" is used to calculate raw (uncalibrated) visibilities from interferometric observations. The files needed by this routine are the ones listed in Figure 5.17 (SKY, DARK, BADPIXEL, FLATFIELD, SCI, or CAL) plus the P2VM file. Notice that amber_SciCal must be run separately for each target, and for each date. The products are written in files with names "amber_-xxxx.fits", each of which is in the OI-FITS format (PAULS et al., 2005). For each observation there will be three of these files, one for each infrared band: J, H, and K. These files carry the primitive header information, reduction parameters, and the resulting uncalibrated interferometric observables. We have developed independent tools to extract and handle these data from OI-FITS files. The resulting visibilities and phases, as well as the calibration process are described below.

5.3.2 Calibrating Interferometry Visibility Data

An important feature of interferometry is that the observation of calibrators is as important as the science object observations. The instrumental effects can be condensed in a transfer function, which gives the point-source response of an interferometer, and can be obtained through observations of calibrators. This is only possible when the interferometric model for calibrators is well understood. The calibrators are usually well known previously studied targets. Our calibrators have been provided by the ESO "search calibrator tool" (*SearchCal*) (BONNEAU et al., 2006). Table 5.2 lists information from our interferometric calibrators, all of which has been used in the analysis of HD 33636 data. Information listed in Table 5.2 has been obtained from Mérand et al. (2005).

TABLE 5.2 - Information for the interferometric calibrators.

Object ID	RA (2000)	Dec (2000)	π_{abs} mas	Spec Type	V mag	J mag	H mag	K mag	Θ_{LD} mas	Θ_J mas	Θ_H mas	Θ_K mas	σ_Θ mas
HD 34137	05:15:11.9	+01:33:22	3 ± 1	K2III	7.20	4.89	4.36	4.18	0.825	0.786	0.798	0.802	± 0.011
HD 19637	03:10:27.0	+26:53:46	8 ± 1	K3III	6.04	3.86	3.24	3.04	1.333	1.274	1.292	1.298	± 0.017
HD 36134	05:29:23.7	-03:26:47	7.0 ± 0.8	K1III	5.81	3.90	3.21	3.12	1.201	1.148	1.164	1.170	± 0.016

SOURCE: Mérand et al. (2005).

Prior to the reduction we investigate whether Sci and Cal sources are resolved or not by the interferometer. The transmitted spatial frequencies observed in our experiment range from $50\,\text{arcsec}^{-1}$ to $550\,\text{arcsec}^{-1}$ approximately. Therefore there is a cut-off at the maximum transmitted frequency f_{max}, which limits the detection of structures with size inferior than f_{max}, i.e. the star apparent diameter will be detected by the interferometer if $\Theta \gtrsim 1.818\,\text{mas}$. From Table 5.2 we notice that all calibrators have apparent sizes relatively close to this value, therefore one should consider a model that accounts for the size of calibrator sources, like the uniform disk model (Equation 3.55). For unresolved sources one should use Equation 3.51, which provides a constant value for the visibilities. Figure 5.19 presents the uniform disk model for the squared visibility (V^2) of calibrators listed in Table 5.2. We have also included in this figure a plot of the V^2 model for HD 33636. The apparent angular diameter Θ (in seconds of arc) of HD 33636 has been estimated through the following expression:

$$\Theta = \frac{R}{107.5 \; d}, \tag{5.17}$$

where R is the physical radius in units of $R_\odot$, and $d = 1/\pi_{abs}$ is the distance in parsecs. Both radius and distance for HD 33636 are presented in Table 2.2.
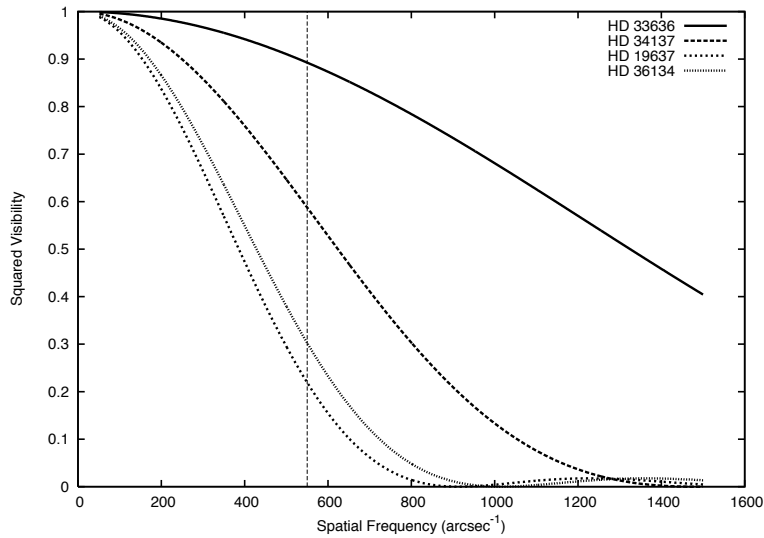
FIGURE 5.19 - Uniform disk model for the squared visibility of calibrators listed in Table 5.2 and the Sci object, HD 33636. Dashed vertical line shows the cut-off frequency for our experiment.

In order to calibrate our interferometric data we have followed the procedure described in Boden (2007), which is shortly discussed below.

Figures 5.20, 5.21, and 5.22 present the data for the three baselines of the raw squared visibilities for the two Cal objects and for HD 33636. We can clearly notice that visibility for all targets follow basically the same pattern. This common pattern is due to the instrumental transfer function, which is also known as the 'system visibility'. In fact the visibilities shown in Figures 5.20, 5.21, and 5.22 contain the signal for each target multiplied by the system visibility. The latter is assumed to be constant within the same baseline, within the same spectral band, and over observations performed within a short time interval.
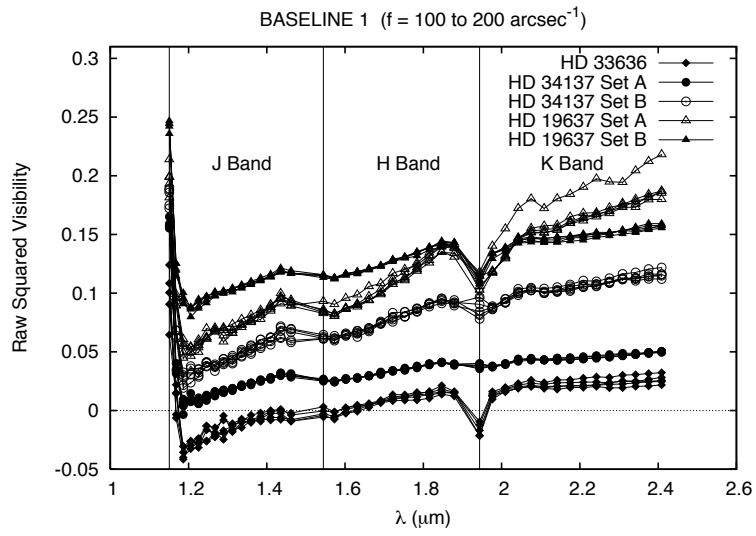
FIGURE 5.20 - Baseline 1 raw squared visibility data for the two calibrators, HD 34137 and HD 19637, and for the science target, HD 33636.
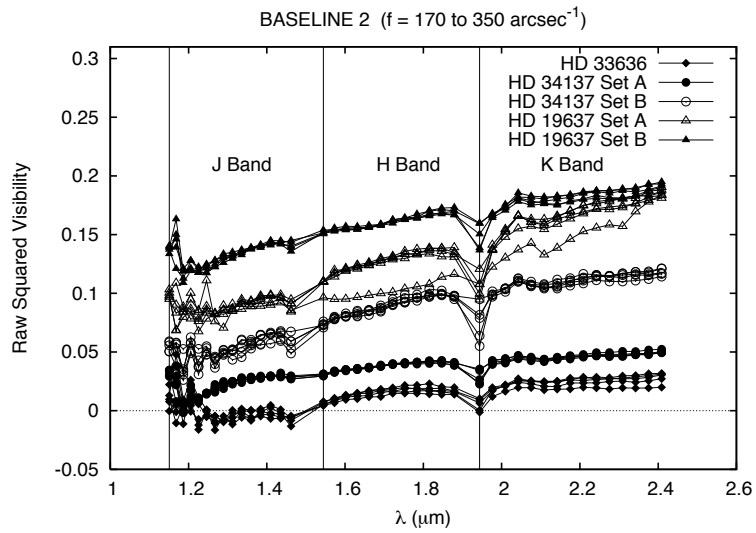
FIGURE 5.21 - Baseline 2 raw squared visibility data for the two calibrators, HD 34137 and HD 19637, and for the science target, HD 33636.
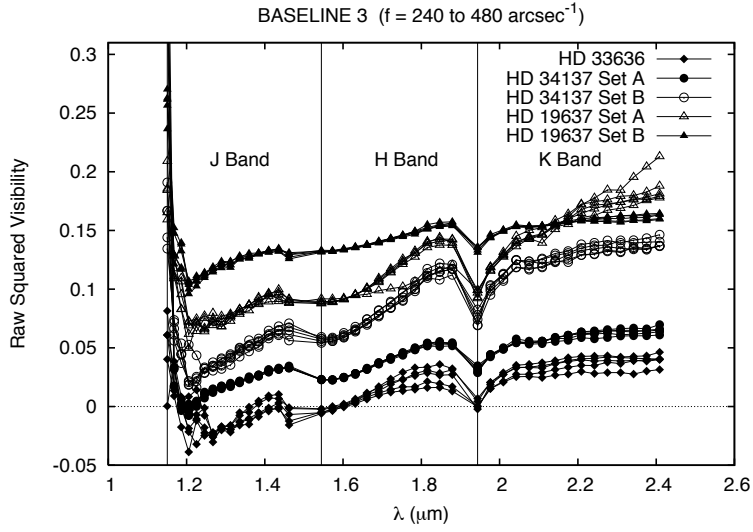
FIGURE 5.22 - Baseline 3 raw squared visibility data for the two calibrators, HD 34137 and HD 19637, and for the science target, HD 33636.

The transfer function, V_{sys}^2 (system visibility) can be obtained from Cal objects through the following equation:

$$V_{sys}^2 = \frac{V_{m-cal}^2}{V_{i-cal}^2}, \tag{5.18}$$

where V_{i-cal}^2 is the intrinsic target visibility, V_{m-cal}^2 is the measured target visibility. Notice that the intrinsic visibility of calibrators is assumed to be known, which are given by the curves provided in Figure 5.19.

Finally, the Sci target calibrated visibility can be obtained through the following expression:

$$V_{c-sci}^2 = \frac{V_{m-sci}^2}{V_{sys}^2}, \tag{5.19}$$

where V_{m-sci}^2 is the measured Sci object visibility.

Before performing the calibration we have to evaluate the data quality. By making

an eyeball inspection of Figures 5.20, 5.21, and 5.22 we could notice that data labeled as 'HD 34137 set B' and 'HD 19637 set A' (open marks), for some reason, at least for the baseline 1, present systematic disagreement with respect to the remaining curves. Observations usually bracket the Sci target with two calibrators, and these two data sets are the ones more distant in time, which may cause some discrepancy in the system visibility. The two data sets taken closest in time to the Sci data, 'HD 34137 set A' and 'HD 19637 set B', shows better agreement. The calibrator HD 36134, which has been observed further in time, is a bright target and presents an excellent agreement with the other calibrators. Therefore we have also included this in our analysis.

These systematic effects can be inspected by looking at the behavior of the system visibility of each data set with respect to the mean system visibility. Figure 5.23 presents a plot of the mean deviation from the average (solid line) and their standard deviation (dashed line). We notice that for the H and K bands, these deviations increase significantly. This may introduce larger errors in the determination of the system visibility and consequently in the Sci calibrated visibility points. In order to check whether any specific data set is causing these effects, we have plotted in Figure 5.24 the system visibility for each set (discontinued lines) and the average of all data sets (thick solid line). It is clear that some sets are exceedingly deviant from the mean. For this reason we have filtered out the calibrator data sets listed in Figure 5.25.

Finally we employ Equations 5.18 and 5.19 to obtain the calibrated visibilities. In order to validate our results we have calibrated two calibrator's data, HD 19637 and HD 36134. This procedure turns the calibrator into Sci target and automatically excludes it from the calibrator list. The last cosmetic operation performed in our data is a σ-cut, where we have excluded points with error larger than a certain threshold. For HD 19637 we have selected points with $\sigma_{V^2} < 1.5$ and for HD 36134 with $\sigma_{V^2} < 2.0$. Figures 5.3.2 and 5.27 present the median taken every 15 calibrated squared visibilities points (solid circles with error bars), and the uniform disk fit model for HD 19637 and HD 36134, respectively. We have obtained the fit angular sizes, $\Theta_{\mathtt{HD19637}} = 1.452 \pm 0.035\,\mathrm{mas}$ and $\Theta_{\mathtt{HD36134}} = 1.362 \pm 0.029\,\mathrm{mas}$, which we consider in good agreement with the values listed in Table 5.2, given that we have not used a λ-dependent model. Figure 5.28 presents HD 33636 data, which we have reduced in exactly the same way as the two calibrators listed above. The disk model is also
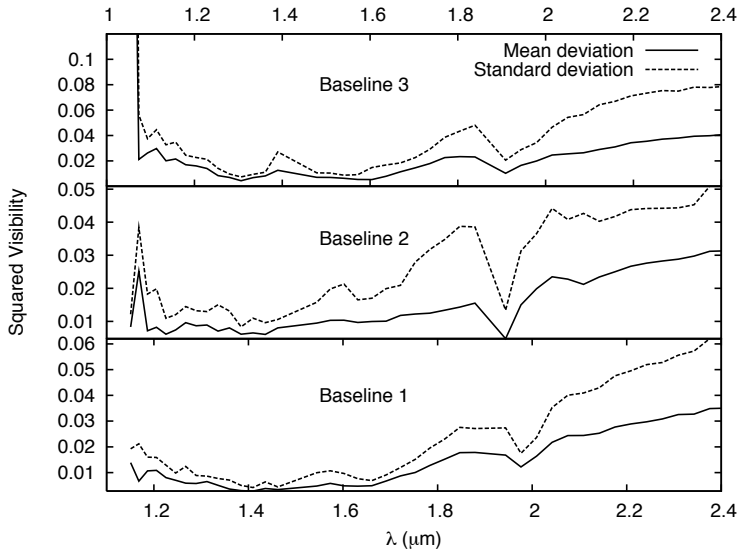
FIGURE 5.23 - Solid lines show the mean difference between each point and the average, $\overline{\Delta V^2}$. Dashed lines show the standard deviation.

shown. We can clearly notice a disagreement between data and the predicted model for an isolated disk-like source. This implies the need of an additional component to explain the brightness morphology, like the binary. This will be explored in the data analysis chapter.

5.3.3 Calibrating Interferometry Phase Data

The calibration of interferometric differential phases (ϕ) and closure phases (Φ) is conceptually similar to the calibration of visibilities. The brightness distribution of calibrators is symmetric, thus the complex visibility function is real. From Equation 3.62 we notice that either the phases or closure phases for calibrators follow a step-like function, where it has constant values, 0 or π, depending on the range of spatial frequency. The change from 0 to π, or vice-versa, occurs at every null of the visibility function. As one can see from Figure 5.19 the maximum spatial frequency sampled by our experiment falls before the first interferometric visibility null of all calibrators. Thus we do not need to concern about the phase inversion in this calibration.

Therefore, in order to obtain the relative calibrated phases for the target $\phi_{cal-trg}$, one just needs to divide the target raw phase $\phi_{raw-trg}$ by the calibrator raw phase
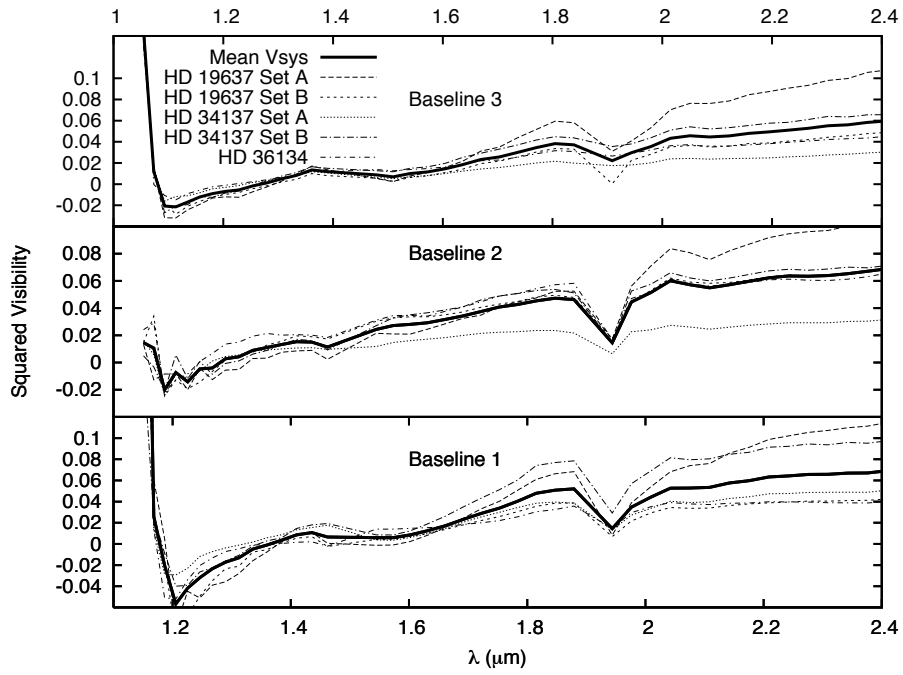
FIGURE 5.24 - System visibility, V_{sys} (transfer function), for all calibrators as indicated in the legend. The thick solid line is the average of all data sets.
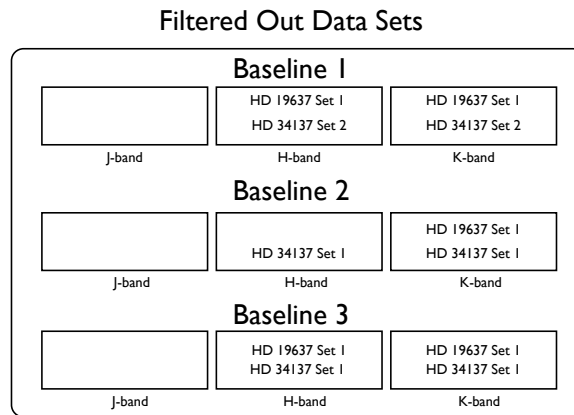
FIGURE 5.25 - List of calibrator data sets that have been filtered out for calibrating interferometric data.

$\phi_{raw-sys}$, so
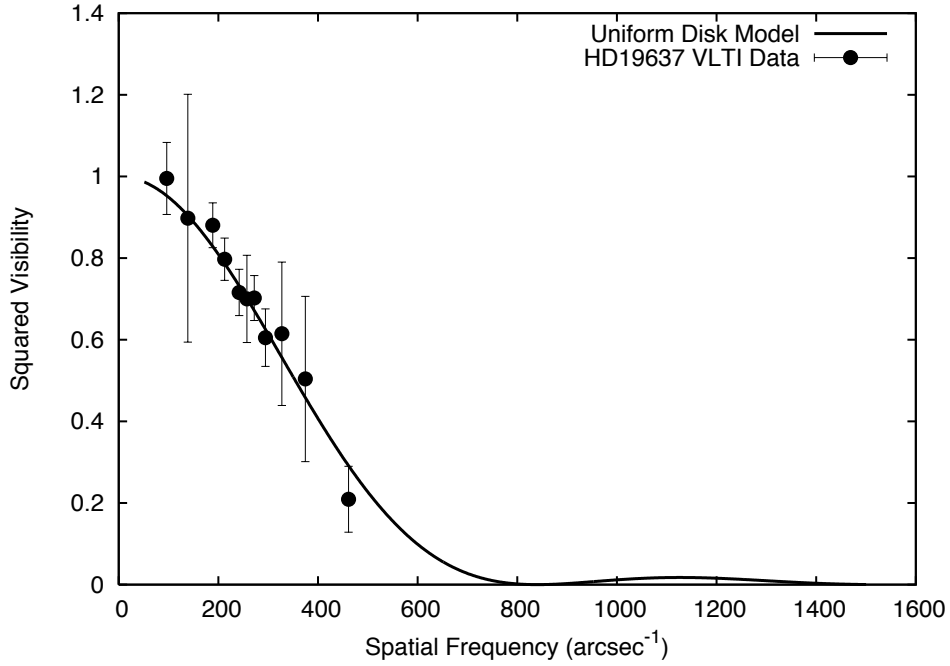
FIGURE 5.26 - HD 19637 squared visibility data (filled circles) and the disk model fit (solid line). Data points with $\sigma_{V^2} > 1.5$ have been cut off. The fit angular diameter for HD 19637 is $\Theta = 1.452 \pm 0.035 \, \text{mas}$.

$$\phi_{cal-trg} = \frac{\phi_{raw-trg}}{\phi_{raw-sys}}. \qquad (5.20)$$

Since we have observations from three calibrators, we calculate $\phi_{raw-sys}$ through the average of raw phases from all calibrators at a given spatial frequency. The OI-FITS files also provides the closure phase data, so one does not need to combine phases from the three baselines. Instead one can directly obtain the closure phase value and perform the calibration in exactly the same way as for the phases. The calibrated phases and closure phases for HD 33636 are presented in Chapter 6.
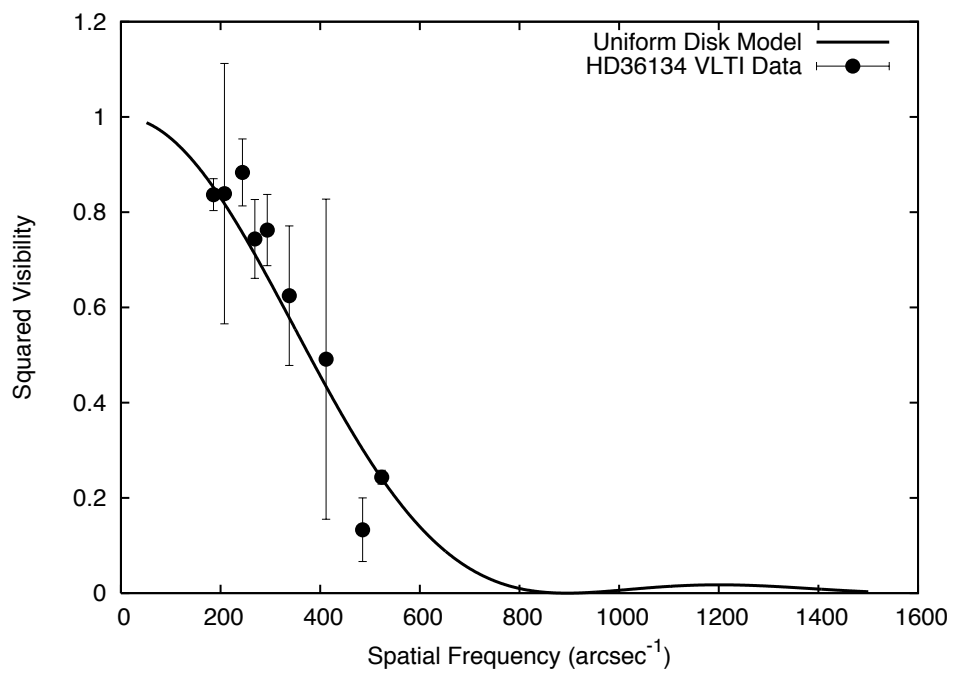
FIGURE 5.27 - HD 36134 squared visibility data (filled circles) and the disk model fit (solid line). Data points with $\sigma_{V^2} > 2.0$ have been cut off. The fit angular diameter for HD 36134 is $\Theta = 1.362 \pm 0.029\,\mathrm{mas}$.
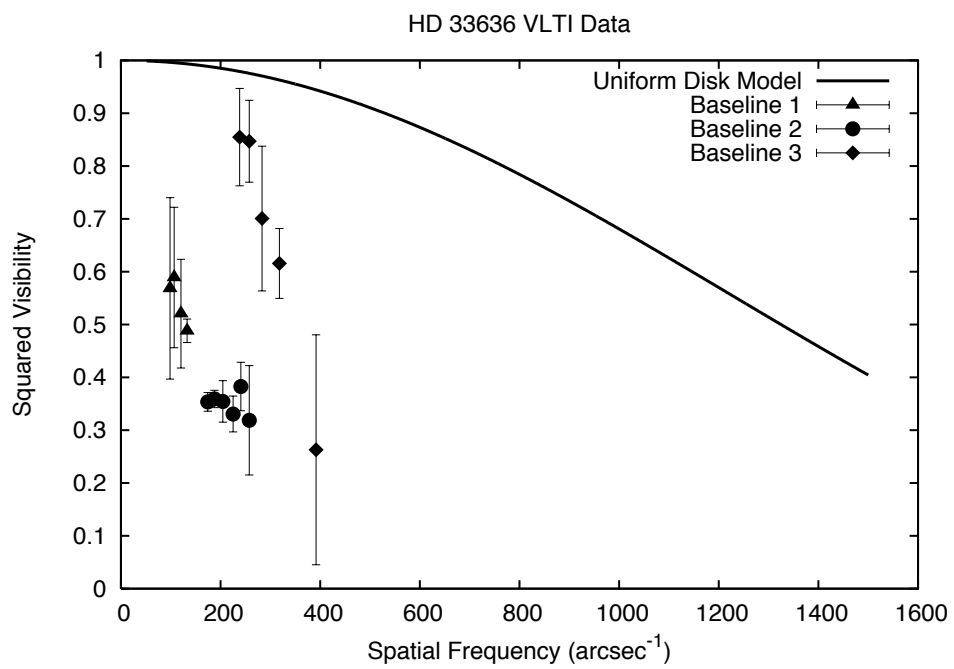
FIGURE 5.28 - HD 33636 squared visibility data is represented by triangles (baseline 1), circles (baseline 2), and diamonds (baseline 3). The disk model for the derived angular size of HD 33636, $\Theta = 0.383$ mas, is also shown (solid line).

6 DATA ANALYSIS

This section is a description of the data analysis to obtain the physical parameters of the systems in study, and comprises the primary results of this work. The main scientific target in our analysis is HD 136118, but we also present a reassessment of HD 33636 previously published radial velocity and astrometry data, for which we have applied the same methodology as for HD 136118. We obtained interferometric data only for HD 33636, which will be included in our analysis and discussed at the end of this chapter.

The spectroscopic RV data obtained with HRS/HET are combined with previously published data, all of which are used to model the system's parameters simultaneously along with FGS astrometry, spectro-photometric parallaxes, and all available information in the literature. This is made in such a way that parameters are constrained and therefore consistent with all datasets. The uncertainties play an important role since they define the degree of influence of each data set in the final results. This will become more clear as we present our results. The data sets with better precision and/or better sampling can be, in some cases, analyzed alone in order to provide a first solution, which is used as prior in the search for a more complete solution, including all data sets. This procedure restricts some parameters ranges within which minimization algorithms will search for the best solution.

Our results were obtained using GaussFit (JEFFERYS et al., 1988) programs, which is an efficient system for solving least-square problems. GaussFit allows one either to employ a regular Levenberg-Marquardt (LM) method or, if desirable, a robust method (HOLLAND; WELSCH, 1977; HUBER, 1981; REY, 1983). The robust method is preferable when the data set is contaminated with outliers. However, there is an issue when one wants to compare the goodness of fit between the two methods. The definition of χ^2 is different in each approach. For this reason we will mostly present the χ^2 obtained from both LM and robust solutions, but the results had ultimately been obtained through the robust method. It will be made explicit in the text when using a different approach.

6.1 Radial Velocity Analysis

The RV data alone already provides important information about the system. This analysis is usually employed for most of the exoplanet candidates found by the

RV method. We present below an analysis of RV data alone for HD 136118 and HD 33636.

The first step in the RV analysis is to separate reduced velocities by their instrument, telescope, and/or site of observation. This segmentation of data must be done because each data set provides a different value for the zero level, which is an offset parameter, Γ (Equation 3.41). Eventually, one should also separate data that has been obtained with the same instrument. This should be done whenever there are reasons to believe that something could have introduced a different offset in part of the data. This might happen, for example, in observations performed after some critical maintenance operation in the spectrograph. A situation like this may not interfere in the instrument's relative precision but may affect the zero level, therefore one should take it into account by introducing a different Γ for each portion of the data. Of course there is a drawback in which as more pieces you split your data as more relative information you lose.

Tables 6.4 and 6.5 present HD 136118 RV data obtained from HET/HRS (MARTIOLI et al., 2010) and from the Lick Observatory (FISCHER et al., 2002). Tables 6.6, 6.7, 6.8, and 6.9 present HD 33636 RV data obtained from HET/HRS (BEAN et al., 2007), Lick Observatory (BUTLER et al., 2006), Keck Observatory (BUTLER et al., 2006), and from the Elodie spectrograph at Observatoire de Haute-Provence (PERRIER et al., 2003), respectively.

The model used to fit RV data is given by Equation 3.41. As we mentioned, we use GaussFit programs to perform this fit. However, if you just input the data with a model given by Equation 3.41, and try to run GaussFit without a good set of initial parameter values, the search for the minimum χ^2 will probably fail. The reason for this is that minimization algorithms get lost easily. It may sometimes either get stuck in a local minimum or enter an infinite loop when doing an outbound search for parameter values. In particular, we found that angular quantities often present problems for minimization algorithms like LM.

HD 136118 and HD 33636 are two systems with RV-detected exoplanet candidate companions. A previous analysis of these companion's orbits made by Fischer et al. (2002) and Bean et al. (2007) provide a solution for the RV orbital parameters of HD 136118 b and HD 33636 b. We adopt these solutions as our initial set of parameters. Figures 6.1 and 6.3 present the Γ-subtracted radial velocities as function of

time, and the best-fit models for the RV orbit of each companion. Figures 6.2 and 6.4 present the same plots folded with the companion's period. The residuals are shown in the bottom panel of each figure.
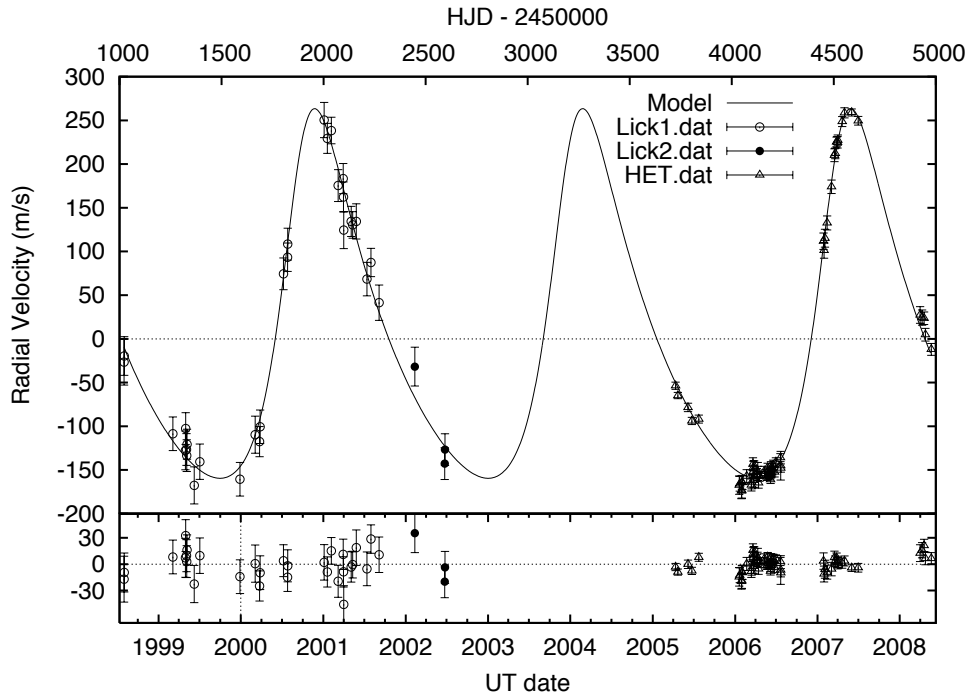
FIGURE 6.1 - HD 136118 radial velocities as function of time and the best-fit model.

Tables 6.1 and 6.2 present the orbital parameters obtained from the fit, the derived minimum masses and semimajor axes, where we have assumed the parent star masses $M_{\text{HD136118}} = 1.24 \pm 0.07\,M_\odot$ (FISCHER et al., 2002) and $M_{\text{HD33636}} = 1.02 \pm 0.03\,M_\odot$ (TAKEDA et al., 2007), and the statistical quantities from the residuals.

Notice that in this analysis we have not considered the possibility of additional companions to these systems. In fact Bean et al. (2007) have investigated this and found no additional companions to HD 33636. Below we discuss the HD 136118 data.

From Table 6.1 we note that the RMS of HET residuals for HD 136118 is about 2.5 times larger than for HD 33636 (shown in Table 6.2). Given that both data sets have been obtained under similar conditions, and that both stars are relatively
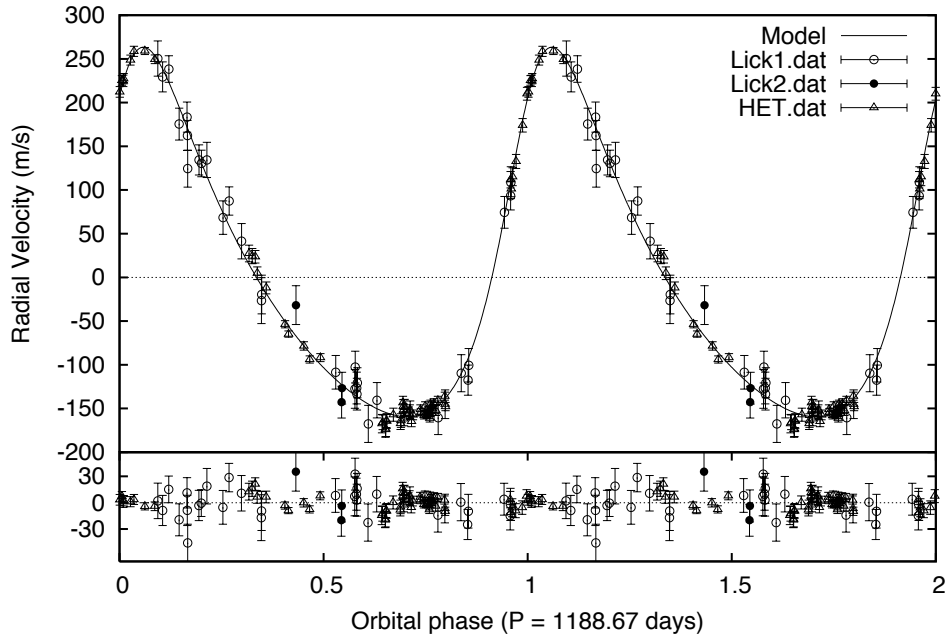
FIGURE 6.2 - HD 136118 radial velocities and the best-fit model in the phase diagram. Folding period is $P = 1188.67$ days.

similar on what concerns the velocity errors, it is likely that an unaccounted source of systematic error is increasing the dispersion of the residuals of HD 136118 above the expected level of usual HET noise. The reduced chi-square, χ_{ν}^2, for HD 136118 HET data is 1.58 and for Lick data is 0.94. A χ_{ν}^2 close to unit indicates satisfactory agreement between the dispersion of residuals and the individual errors. Therefore this agreement seems not to be as definitive for the HET as it is for Lick data.

We first check whether the residuals follow a Gaussian distribution and inspect the errors involved. Figure 6.5 shows the histogram of distribution of residuals for the two individual datasets separately, Lick and HET, and also for both datasets combined (hereafter "ALL"). We can see the different dispersion for each dataset. We note that each individual dataset, either HET and Lick, are not following exactly a normal distribution. We call attention to the fact that the dispersion on HET residuals is about three times larger than the error (~ 3 m/s) estimated from previous work (BEAN et al., 2007, e.g.). This discrepancy may be identified with an unaccounted for
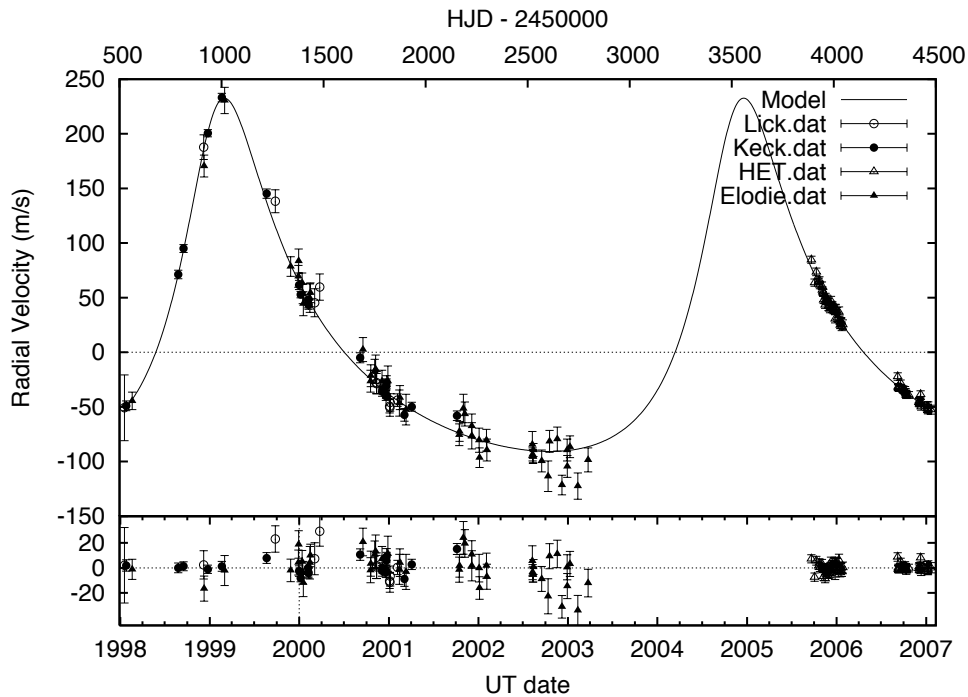
FIGURE 6.3 - HD 33636 radial velocities as function of time and the best-fit model.

systematic effect. Below we investigate the detection limits for any further periodic signal that could still be present in the data.

6.1.1 Limits on Additional Periodic Signals in the HD 136118 RV Data

The customary method for searching periodic signals in unevenly spaced data is by means of the Lomb-Scargle Periodogram (LSP) (SCARGLE, 1982). Figures 6.6 and 6.7 show the LSP of residual RV data for two different datasets respectively: ALL and HET. The sets are analyzed separately because they have different errors (see Table 6.1). The power in the LSP is weighted by the overall variance, therefore if one mixes two sets with different variances it would result in an overestimated power for higher levels of noise. The downside of analyzing datasets separately is that sampling becomes different as you have different time coverage and it may affect the signal detectability for some frequencies.

Fischer et al. (2002) show that the LSP for Lick data does not seem to present any
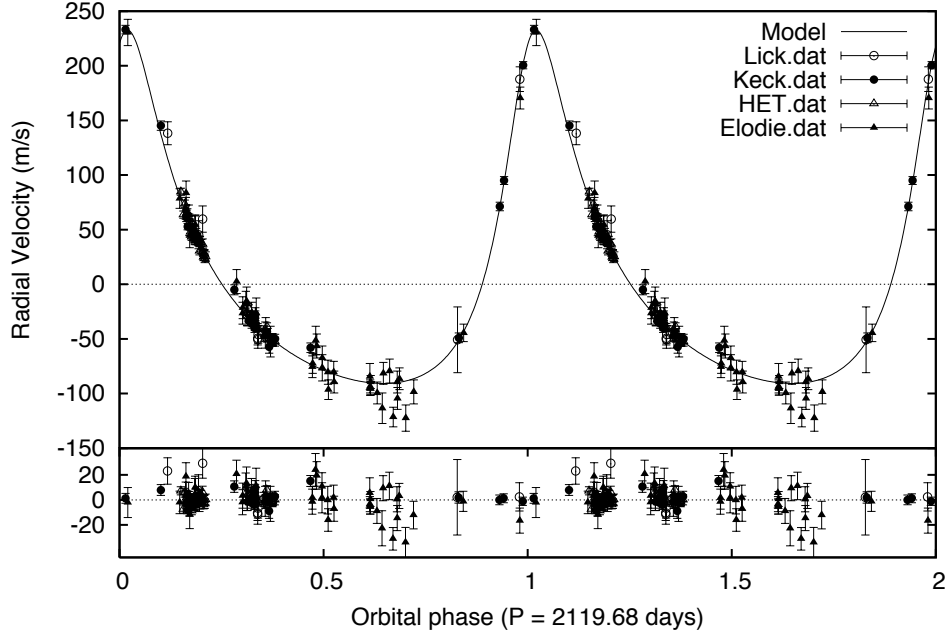
FIGURE 6.4 - HD 33636 radial velocities and the best-fit model in the phase diagram. Folding period is $P = 2119.68$ days.

expressive power. The LSP for HET dataset (Figure 6.7) shows some peaks at the limit where False Alarm Probability (FAP) is as low as about 1%. The combined dataset also shows some power below the level of 1% FAP. This indicates that either there is still an unaccounted periodic signal or the sampling for those frequencies is poor. The latter may be analyzed by the method we describe below.

We introduce a quantity to evaluate how much we can trust some high power found at a given frequency based on sampling for that frequency. We call this quantity the Amount of Information in the Phase Diagram (AIPD). It is defined by the following expression,

$$I = -\sum_{i=1}^{N_b} p_i \ln p_i / \ln N_b, \qquad (6.1)$$

where N_b is the number of bins in the phase diagram, p_i is the probability of finding

TABLE 6.1 - HD 136118: RV best-fit parameters.

Orbital parameters:

P (days)	$=$	1188.7	$\pm$	2.1
T (JD)	$=$	2450614	$\pm$	7
e	$=$	0.33	$\pm$	0.01
ω (°)	$=$	317.4	$\pm$	1.0
K $(\mathrm{m\,s^{-1}})$	$=$	211.4	$\pm$	1.5

Derived parameters:

$\mathrm{M}\sin i$ $(\mathrm{M_J})$	$=$	12.1	$\pm$	0.5 (3.82%)
$\mathrm{M}\sin i$ $(\mathrm{M_\odot})$	$=$	0.0115	$\pm$	0.0004 (3.82%)
$\mathrm{a}\sin i$ (AU)	$=$	2.35	$\pm$	0.16 (6.90%)

Systemic velocities $(\mathrm{m\,s^{-1}})$:

Γ_{Lick1}	$=$	1	$\pm$	4
Γ_{Lick2}	$=$	-10	$\pm$	13
Γ_{HET}	$=$	486.3	$\pm$	1.4

Statistical quantities:

$\chi^2 = 116.74$	DOF $= 88$
$\chi^2_\nu = 1.33$	
$\mathrm{RMS}_{Lick} = 16.58\ \mathrm{m\,s^{-1}}$	
$\mathrm{RMS}_{HET} = 8.26\ \mathrm{m\,s^{-1}}$	

a data point within a given bin i, and may be calculated by $p_i = n_i/N$, where n_i is the number of points inside the bin i and N is the total number of data points. Note that the dependence on the period arises from the construction of the phase diagram. This quantity is normalized and therefore it varies from 0 to 1. When $I = 0$ it means that all data points are found within a single bin in the phase diagram and hence sampling for that frequency is very poor. On the other hand when $I = 1$ it means that probability p_i is the same for every bin and data is equally distributed along all bins. This gives you an ideal coverage of the phase diagram. We call attention to the fact that AIPD does not measure the statistical significance of the number of data points but only the significance of how well distributed are these points in the phase diagram. Therefore an issue of concern is the choice of an adequate N_b. We suggest the choice is made in the same fashion as when you build a traditional histogram for inspecting probability distributions. Our choice of N_b is that of $N/N_b > 30$ data-points-per-bin. If N is small such that makes $N_b < 10$ then we assume $N_b = 10$.

Figures 6.6 and 6.7 also show a plot of AIPD (in the plot it is multiplied by 20 and shifted for the sake of visualization). We notice that some of the high power periods

TABLE 6.2 - HD 33636: RV best-fit parameters.

Orbital parameters:

P (days)	=	2120	$\pm$	8
T (JD)	=	2451196	$\pm$	6
e	=	0.477	$\pm$	0.007
ω (°)	=	337.0	$\pm$	1.4
K (m s^{-1})	=	161.4	$\pm$	1.8

Derived parameters:

$\text{M} \sin i$ (M$_J$)	=	9.1	$\pm$	0.2 (2.30%)
$\text{M} \sin i$ (M$_\odot$)	=	0.0087	$\pm$	0.0002 (2.30%)
$\text{a} \sin i$ (AU)	=	3.23	$\pm$	0.13 (4.02%)

Systemic velocities (m s^{-1}):

Γ_{Lick}	=	-38	$\pm$	3
Γ_{Keck}	=	-32.8	$\pm$	1.4
Γ_{HET}	=	-0.1	$\pm$	2.7
Γ_{Elodie}	=	155.1	$\pm$	1.8

Statistical quantities:

$\chi^2 = 184.17$	DOF = 137
$\chi^2_\nu = 1.34$	
$\text{RMS}_{Lick} = 13.06$ m s^{-1}	
$\text{RMS}_{Keck} = 6.03$ m s^{-1}	
$\text{RMS}_{HET} = 3.35$ m s^{-1}	
$\text{RMS}_{Elodie} = 11.87$ m s^{-1}	

in the LSP also present a decreasing on the AIPD, which means a deficit of sampling for those periods. This is evident for the 1 yr period where there is always lack of data for some part of the phase diagram. If you fold the 1 yr phase diagram twice there will still be some lack of data coming from the 1 yr sampling problem. This can be seen from the smaller decreases at half year period. Although it is smaller it may still affect the LSP. If one disregards the powers at periods which are close integer fractions of a year there will be no significant power left on the LSPs.

However, the existence of an additional signal cannot be ruled out by looking only at the LSP for the following reason. If the signal comes from an orbit which follows the RV model (Equation 3.41), then it may be considered solutions for eccentric orbits instead of strict sine and cosines as in the LSP. An alternative periodogram using the orbit solution is explored in Gregory (2007). We propose a strategy to find a possible hidden signal in our particular case, although it could be expanded and applied for any other system.
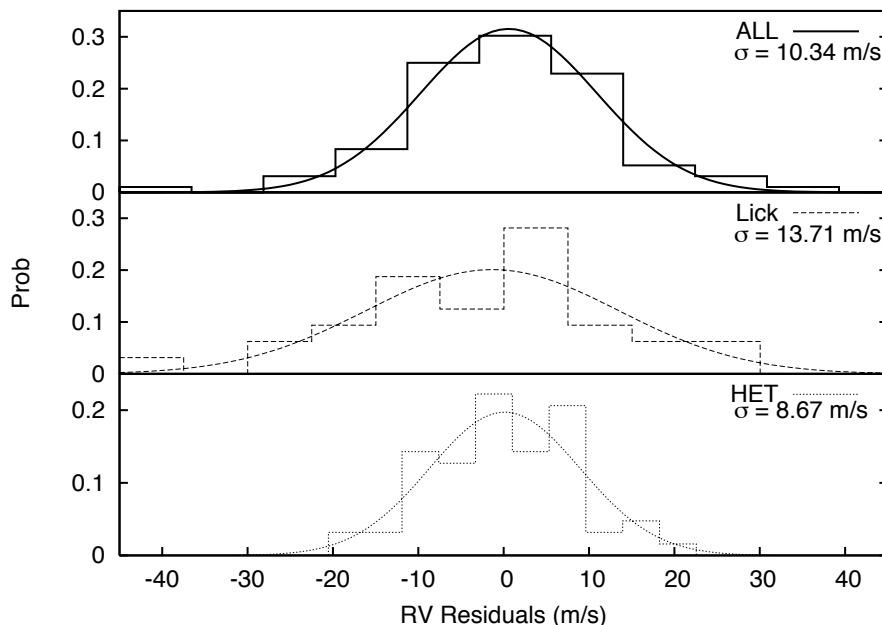
FIGURE 6.5 - Histogram of HD 136118 RV residuals from 1-companion model for 3 datasets: all combined (ALL) (top panel), Lick (middle panel) and HET (bottom panel).

Our strategy consists in making multiple attempts to model the RV, using a 2-companion model (linear superposition of two Keplerian orbits), and keeping the trial periods as constants in the fitting process. This process forces the minimization algorithm to search for the best solutions for each chosen period. This approach could result in a lower χ^2 when including a hidden periodic component. Figure 6.8 shows a χ^2 map over a range of periods for a 2-companion model fitting RV HET and Lick data simultaneously. The grid point resolution is 1100×90, which means a step on the trial periods of about ~ 0.3 day for both components. From Figure 6.8 we can see a region around 255 days where we found an island of lower χ^2 (darker regions), which indicates the presence of an additional signal. We note that the relatively high power peak at ~ 95 days in the LSP (see Figure 6.6) is now ruled out, because any attempt of fitting a secondary orbit with this period results in larger χ^2. This approach does not prove the existence of another companion in the system. Rather it shows an effective way of finding solutions that are considerably improved by adding
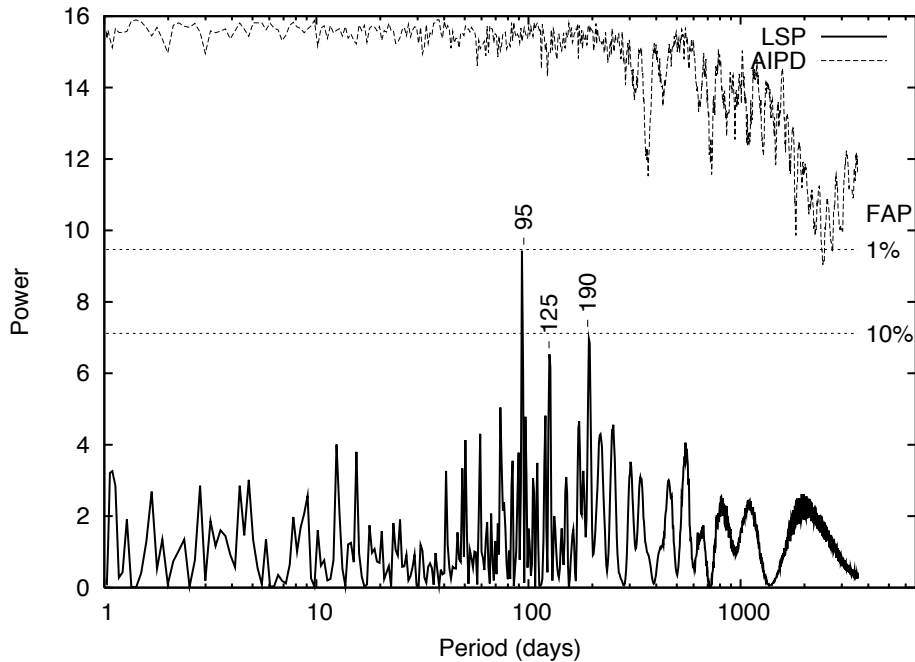
FIGURE 6.6 - Lomb-Scargle periodogram for RV residuals from 1-companion model and using all datasets combined (solid line). The thresholds for false alarm probability of 1% and 10% are plotted in dotted lines. Above it is shown the AIPD (see text) for the same dataset (dashed line). The AIPD here is multiplied by a factor 20 and shifted for the sake of better visualization.

a weak periodic signal that could not be detected in the LSP. Moreover, our model uses Keplerian orbits, which look not only for a periodic signal but for a signal with the shape of an orbit.

Then, we performed a refined fit using the LM method and then a robust fit method for a 2-companion model with an additional signal with period of about 255 days. This solution presents a significant improvement of 30% on the χ^2 if compared to the 1-companion model (see Tables 6.1 and 6.3). The parameters for a 2-companion model are shown on Table 6.3. The σ dispersion for HET data is now in agreement with that we expected. Figure 6.9 shows the HD 136118 radial velocities as function of time and the best-fit two-companion model. Figures 6.10 and 6.11 show the phase diagram of RV data and the respective component orbit model. The reality of this additional companion to the system will be discussed in Chapter 7. The parameters
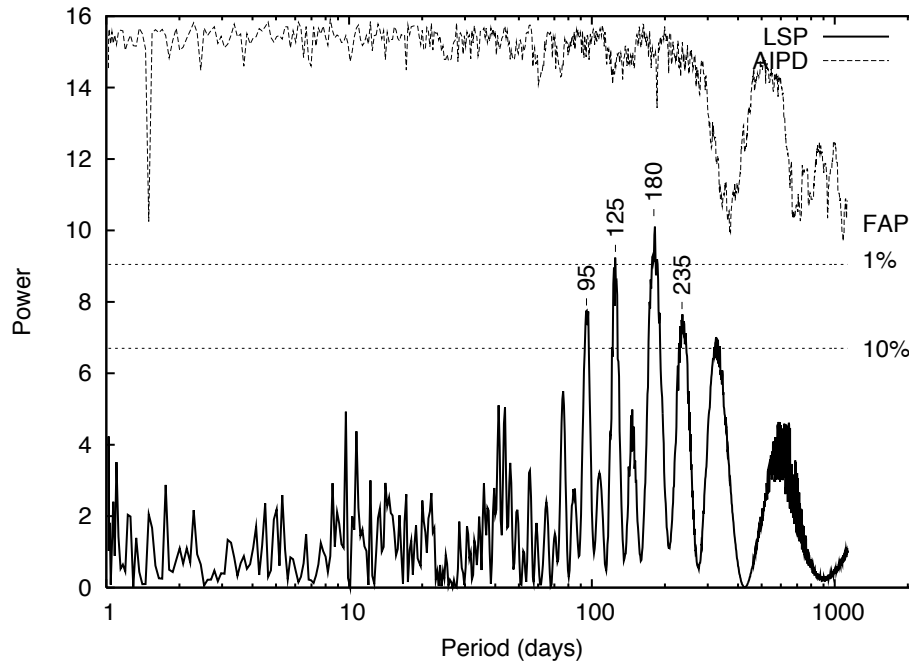
FIGURE 6.7 - Lomb-Scargle periodogram for HET RV residuals from 1-companion model (solid line). The thresholds for false alarm probability of 1% and 10% are plotted in dotted lines. Above it is shown the AIPD (see text) for the same dataset (dashed line). The AIPD here is multiplied by a factor 20 and shifted for the sake of better visualization.

adopted in the following sections are those from a 2-companion model. The modelling of the second component in the RV has a very marginal effect on the parameters of the astrometric detection, so it is not "polluting" our result.
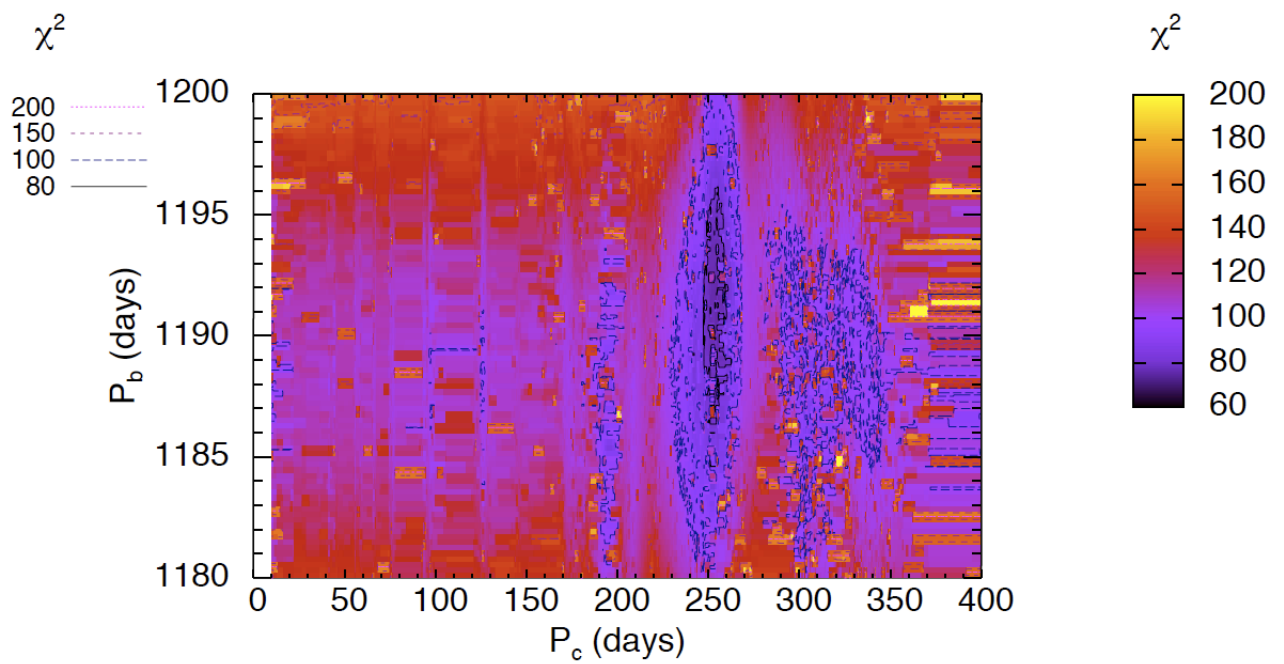
FIGURE 6.8 - χ^2 map from a 2-companion fit model for HET and Lick data. The grid
resolution is about $0.3\,\mathrm{day}$ (1100×90 points). Contour lines show four
different levels of χ^2. The best fit solution has the lowest value at $\chi^2 = 76.6$.

TABLE 6.3 - HD 136118: RV best-fit parameters for a two-companion model.

	HD 136118 b	Nuisance orbit
Orbital parameters:		
P (days)	1191.5 ± 1.9	254.1 ± 1.7
T (JD)	2450609 ± 6	2453759 ± 10
e	0.348 ± 0.009	0.41 ± 0.13
ω (°)	316.4 ± 1.1	190 ± 19
K (m s^{-1})	216.7 ± 1.5	10.9 ± 1.8
Derived parameters:		
$M \sin i$ (M$_J$)	12.3 ± 0.5 (3.82%)	0.36 ± 0.06 (18.01%)
$M \sin i$ (M$_\odot$)	0.0117 ± 0.0004 (3.82%)	0.00034 ± 0.00006 (18.01%)
$a \sin i$ (AU)	2.35 ± 0.16 (6.89%)	0.84 ± 0.24 (28.01%)
Systemic velocities (m s^{-1}):		
$\Gamma_{Lick1} = 0.1 \pm 4$		
$\Gamma_{Lick2} = -10 \pm 11$		
$\Gamma_{HET} = 486.2 \pm 1.2$		
Statistical quantities:		
$\chi^2 = 74.44$	DOF $= 83$	
$\chi^2_\nu = 0.90$		
RMS$_{Lick} = 15.60$ m s^{-1}		
RMS$_{HET} = 5.60$ m s^{-1}		
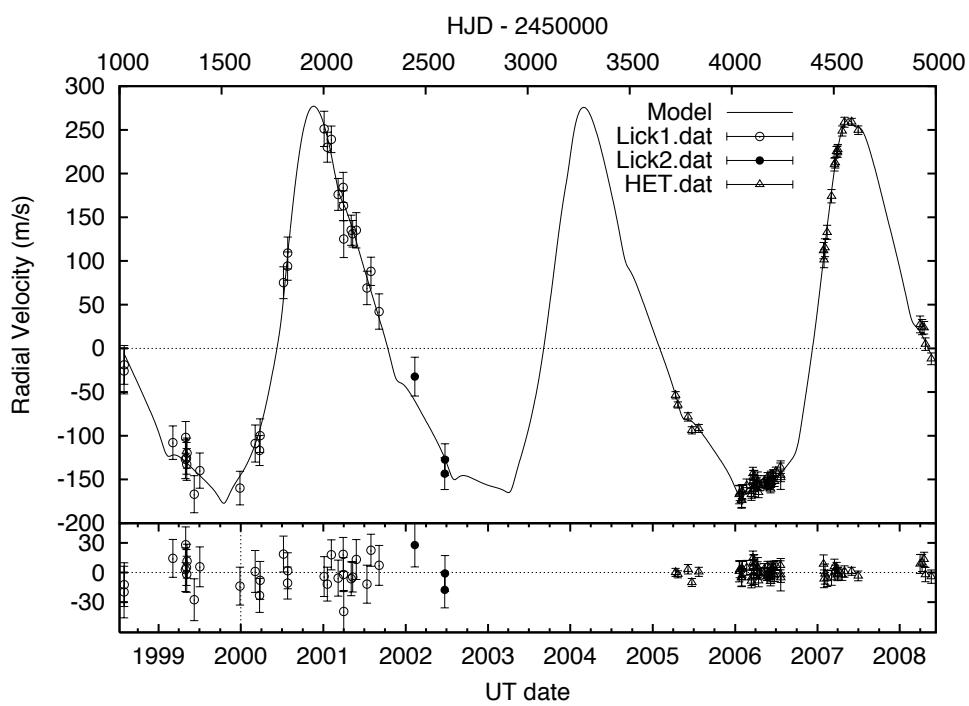
FIGURE 6.9 - HD 136118 radial velocities as function of time and the best-fit two-companion model.
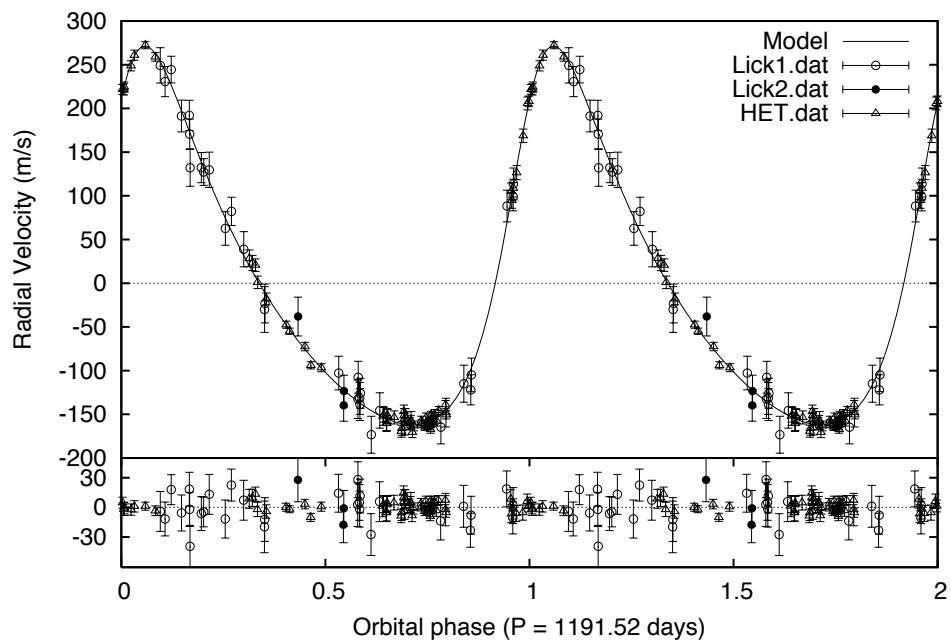
FIGURE 6.10 - Phase diagram folded with period 1191.52 days. RV HET (filled circles) and Lick (open marks) data subtracted the "nuisance orbit" model. Solid line shows the best fit HD 136118 b orbit model. Residuals from the 2-companion model is plotted in the bottom panel.
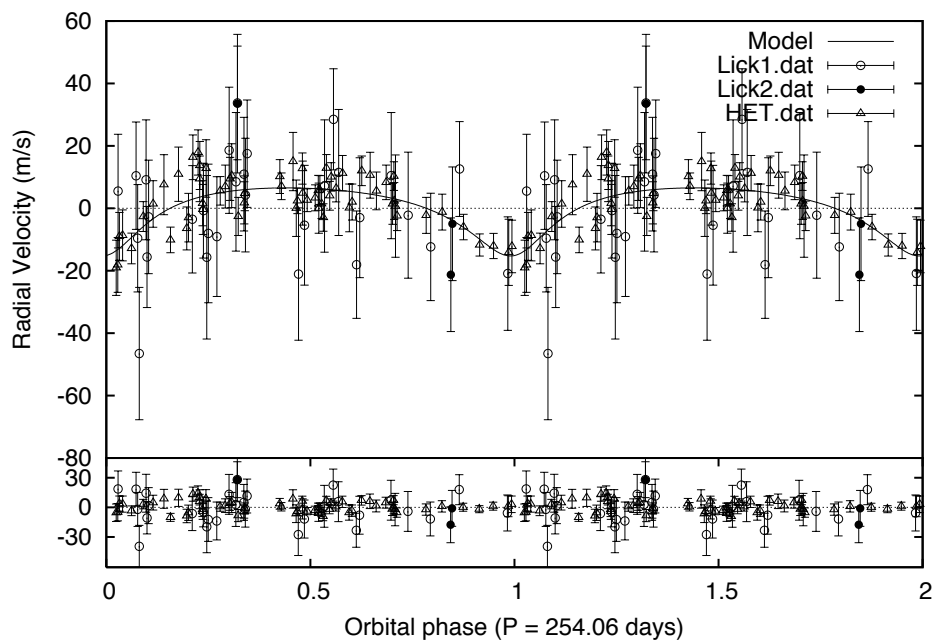
FIGURE 6.11 - RV HET (filled circles) and Lick (open marks) residuals from HD 131168 b orbit model and the best fit "nuisance orbit" model plotted in the phase diagram folded with period 254.06 days. Residuals from the 2-companion model is plotted in the bottom panel.

TABLE 6.4 - HET relative radial velocities for HD 136118.

HJD - 2450000	RV (m/s)	$\pm\sigma$ (m/s)
3472.831	432.6	4.1
3482.881	421.4	3.5
3527.763	407.8	4.8
3544.727	392.4	4.1
3575.630	394.6	4.6
3755.051	319.0	10.6
3757.041	320.5	8.4
3765.026	312.2	8.8
3766.026	313.0	8.8
3767.020	321.9	7.7
3769.011	321.9	8.2
3787.982	329.2	7.5
3808.904	319.1	6.9
3809.909	322.5	7.8
3815.886	342.9	7.3
3816.898	334.4	7.3
3816.965	338.7	7.7
3818.873	324.5	8.0
3820.897	337.5	9.2
3832.840	331.2	6.9
3835.853	333.6	6.9
3836.858	334.6	10.2
3840.895	321.5	6.1
3844.909	328.9	5.6
3866.774	335.1	5.4
3867.754	332.1	4.3
3877.724	328.3	4.1
3880.810	339.0	5.0
3883.778	329.3	3.7
3888.700	330.7	4.2
3890.679	333.3	4.9
3891.682	333.7	4.6
3892.689	329.5	4.7
3893.768	325.2	4.4
3895.744	341.4	4.4
3897.749	332.9	4.6
3898.678	339.1	4.5
3901.740	336.0	4.3
3905.734	341.8	5.7
3911.730	333.9	5.8
3917.689	345.5	4.8
3938.639	341.2	16.4
3937.648	350.4	4.6
3939.631	338.5	4.7
4129.036	598.0	9.3
4131.023	587.5	9.0
4135.035	601.4	10.3
4144.998	619.0	8.0
4164.019	660.3	7.7
4176.992	696.4	7.3
4180.889	698.6	6.1
4186.887	711.6	5.5
4190.869	711.2	6.5
4191.864	713.7	5.9
4211.816	734.9	5.8
4221.789	744.9	5.7
4253.699	745.3	4.0
4282.631	735.8	4.9
4556.884	513.6	9.6
4565.914	510.6	8.7
4574.895	509.8	7.2
4580.893	491.0	7.2
4606.803	474.3	6.7

TABLE 6.5 - Lick relative radial velocities for HD 136118.

set	HJD - 2450000	RV (m/s)	$\pm\sigma$ (m/s)
1	1026.698	-26	26
1	1027.688	-19	22
1	1243.013	-108	19
1	1298.905	-127	22
1	1299.820	-102	18
1	1303.868	-126	18
1	1304.818	-133	18
1	1305.833	-120	17
1	1337.757	-167	21
1	1362.751	-140	20
1	1541.094	-160	19
1	1608.003	-109	21
1	1627.902	-117	17
1	1629.891	-100	19
1	1733.725	75	18
1	1751.729	94	16
1	1752.682	109	18
1	1914.096	251	20
1	1928.092	230	17
1	1946.039	239	15
1	1976.046	176	18
1	1998.971	184	17
1	1999.933	163	17
1	2000.978	125	21
1	2033.907	135	17
1	2040.850	131	15
1	2056.871	135	20
1	2103.736	69	19
1	2121.686	88	16
1	2157.646	42	20
2	2316.050	-42	22
2	2448.778	-153	18
2	2449.751	-137	18

TABLE 6.6 - HET relative radial velocities for HD 33636.

HJD - 2450000	RV (m/s)	$\pm\sigma$ (m/s)
3633.938	85.6	3.2
3646.908	64.7	3.3
3653.901	74.5	3.5
3663.872	65.8	2.9
3666.841	66.9	3.2
3668.833	62.5	3.4
3676.839	61.8	3.5
3678.810	58.0	2.9
3680.805	56.1	3.0
3682.797	55.4	3.2
3683.812	48.8	3.3
3689.922	44.3	3.2
3691.790	51.9	3.0
3692.789	47.8	2.9
3696.771	47.4	3.0
3697.768	50.3	2.9
3700.760	47.3	2.6
3703.752	43.0	4.0
3708.862	43.2	3.3
3709.879	40.5	3.4
3713.724	48.2	3.9
3714.870	43.7	3.9
3719.698	41.3	4.1
3719.844	43.1	3.9
3724.819	41.2	3.4
3724.822	39.7	3.6
3730.667	31.5	3.7
3731.674	40.8	3.5
3732.665	41.4	3.5
3738.661	38.7	3.1
3739.646	32.5	3.4
3746.623	37.7	4.7
3748.633	30.4	3.7
3751.752	25.9	3.4
3753.748	28.9	3.7
3754.612	28.6	3.7
3755.602	28.7	3.6
3757.751	24.6	3.9
3762.592	26.2	4.4
3985.980	-21.3	3.4
3987.965	-31.4	2.7
3988.970	-30.3	2.7
3989.969	-31.3	2.7
3990.963	-32.3	2.7
3997.952	-27.1	2.7
4007.922	-33.6	2.8
4008.905	-32.9	3.1
4014.901	-35.0	2.7
4015.906	-33.7	3.3
4018.887	-35.4	3.0
4019.878	-36.6	2.8
4020.875	-38.4	3.0
4021.873	-37.5	3.0
4031.847	-38.2	3.1
4072.738	-45.0	3.4
4073.736	-43.6	3.0
4075.863	-46.1	3.0
4076.728	-44.4	3.1
4079.719	-37.6	3.3
4080.844	-45.4	3.0
4081.859	-48.9	3.2
4105.656	-48.5	4.0
4106.773	-50.6	3.7
4108.781	-50.5	3.9
4109.775	-51.8	3.7
4110.787	-48.8	4.3
4121.610	-51.6	4.1

TABLE 6.7 - Lick relative radial velocities for HD 33636.

HJD - 2450000	RV (m/s)	$\pm\sigma$ (m/s)
831.736	-87.6	30.1
1154.792	150.9	11.3
1447.032	101.4	10.5
1607.684	8.5	12.8
1628.629	22.9	12.0
1859.945	-65.5	9.3
1860.907	-64.6	10.2
1913.782	-86.2	6.1
1914.844	-87.5	7.9
1915.801	-82.7	8.0
1945.718	-80.6	5.7

TABLE 6.8 - Keck relative radial velocities for HD 33636.

HJD - 2450000	RV (m/s)	$\pm\sigma$ (m/s)
838.759	-82.1	4.5
1051.103	38.1	3.9
1073.040	61.9	3.6
1171.845	167.4	3.3
1228.803	200.0	3.9
1412.107	112.1	4.3
1543.900	28.5	4.2
1550.886	19.7	2.9
1580.836	15.2	4.7
1581.868	11.6	4.0
1582.785	10.3	4.1
1793.120	-38.1	4.6
1882.934	-69.1	4.3
1884.085	-67.0	4.0
1898.032	-73.2	3.9
1899.045	-71.6	3.6
1900.065	-63.7	3.7
1901.014	-60.9	3.4
1973.749	-90.4	5.8
2003.746	-83.0	4.1
2188.139	-91.2	4.4

TABLE 6.9 - Elodie relative radial velocities for HD 33636.

HJD - 2450000	RV (m/s)	$\pm\sigma$ (m/s)
863.326	112	8
1156.524	327	10
1240.334	387	12
1509.583	235	9
1541.427	226	10
1542.398	240	11
1556.390	220	9
1559.405	210	9
1561.436	201	11
1588.345	206	13
1590.350	211	9
1804.677	159	11
1835.654	130	10
1836.669	135	10
1852.600	139	11
1856.583	141	13
1882.499	130	10
1901.483	125	10
1906.538	130	14
1953.349	110	12
1955.316	115	11
1980.304	104	14
2197.668	81	10
2198.655	84	9
2214.610	105	13
2220.600	100	11
2248.517	89	11
2248.529	80	12
2278.421	76	11
2280.447	60	9
2308.439	76	10
2310.396	67	10
2495.887	72	12
2496.927	63	6
2497.924	61	6
2498.909	61	6
2499.928	67	6
2533.656	57	10
2559.661	43	14
2565.653	75	10
2597.588	77	11
2616.528	35	9
2637.481	67	10
2638.454	52	10
2649.414	70	10
2681.431	34	12
2723.309	58	11

6.2   Astrometry Analysis

Figure 6.12 and 6.13 provide sample images of the HD 136118 and HD 33636 field-of-view. The reference stars used for astrometry are indicated.
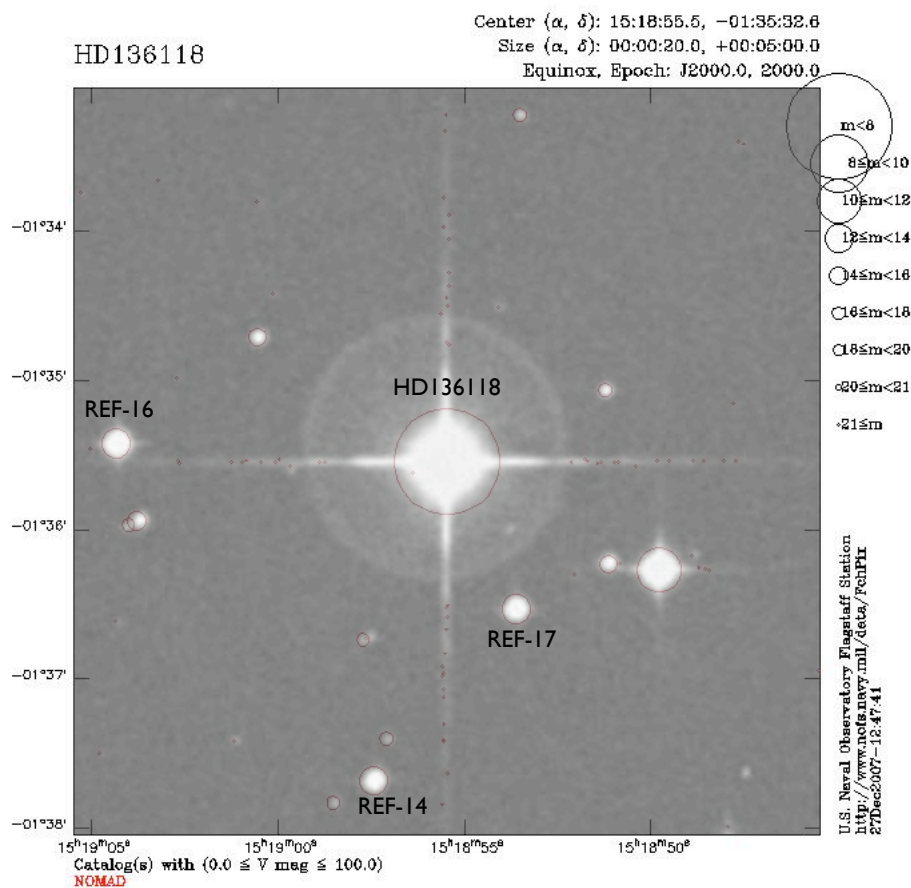
FIGURE 6.12 - HD 136118 field-of-view. Source: image from the Science and Engineering Research Council Survey (SERC), Space Telescope Science Institute (STSI), digitized with the Plate Densitometer Scanner (PDS). This is superimposed on the Naval Observatory Merged Astrometric Dataset (NOMAD) catalog. These were obtained through the Aladin previewer and the SIMBAD database.

The astrometry analysis consists of solving the overlapping plate model through Equations 5.11 and 5.12. By setting one plate fixed, the reference frame, we are forcing the minimization algorithm to find the best rotation, scaling and offset constants that brings all plates to the same reference frame. Additionally to the plate

111
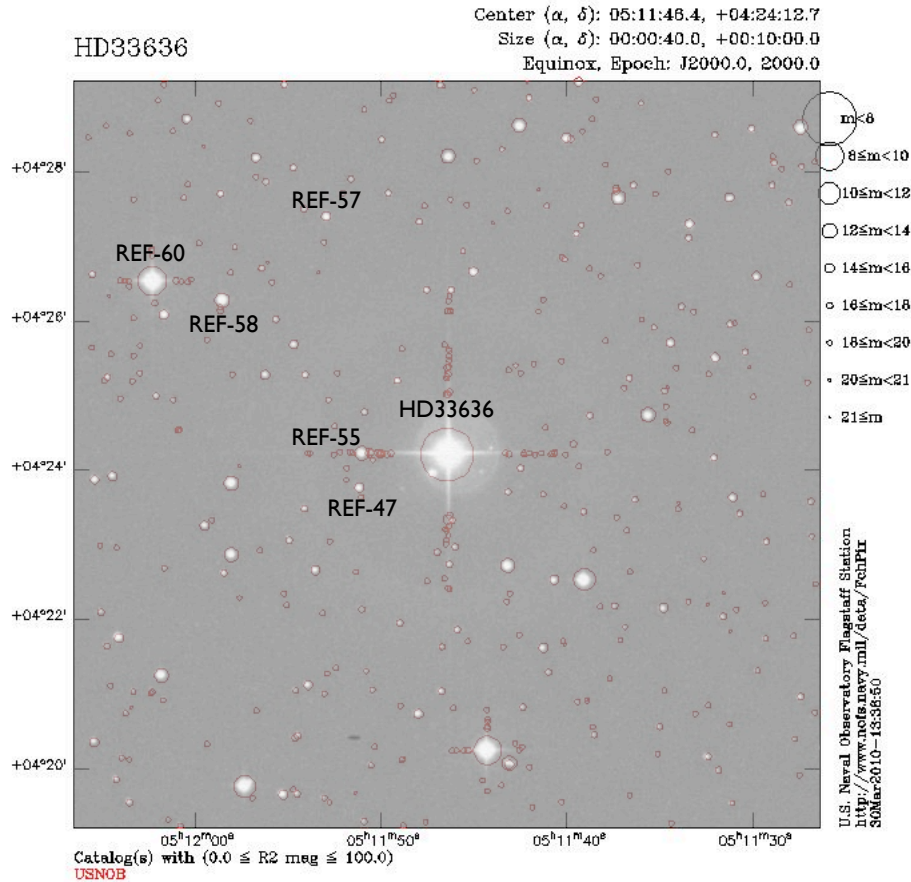
FIGURE 6.13 - HD 33636 field-of-view. Source: image from the Palomar Observatory Sky Survey (POSSII), Space Telescope Science Institute (STSI), digitized with the Plate Densitometer Scanner (PDS). This is superimposed on the Naval Observatory Merged Astrometric Dataset (NOMAD) catalog. These were obtained through the Aladin previewer and the SIMBAD database.

model we also have to solve simultaneously the astrometric model, which is given by Equations 3.38 and 3.39. The latter provides each star's coordinates in the reference frame (ξ, η), parallaxes and proper motion components for each reference star, and the perturbation orbit.

A particular interesting feature of GaussFit, which is important for this problem, is that it permits the inclusion of constraints in the model. The constraints in GaussFit can be included in two different ways. First by using the in-built function `exportconstraint[u]`, to fix a given condition 'u', or by setting a given variable parameter as observation with error. The latter may be used whenever there is a

previous measurement of the quantity, which may be improved by the addition of new data. The use of a prior information to obtain a posterior updated solution resembles the Bayesian methods. For this reason we sometimes call this a quasi-Bayesian approach. In the sections below we describe the constraints we have used in order to obtain our global solution.

6.2.0.1 RV constraint

The analysis of astrometry data can not be made independently as we have done for RV data. This is due to the poor sampling and to the exceeding number of free parameters in the astrometric model. Nevertheless we can use the RV parameters in order to estimate the amplitude of the astrometric signal due to the RV-detected companions to HD 136118 and HD 33636. Equations 3.42 and 3.37 can be combined to give the following (POURBAIX; JORISSEN, 2000),

$$\frac{\alpha}{\pi_{\mathsf{abs}}} = \frac{(9.192 \times 10^{-8}) K P \sqrt{1 - e^2}}{\sin i}, \tag{6.2}$$

where α is the semimajor axis and π_{abs} is the absolute parallax both in units of milliseconds of arc (mas). K, P, and e are the orbital elements obtained from RV analysis, where the velocity is in $\mathrm{m\,s^{-1}}$ and the period in days. i is the inclination angle, which is also unknown. In Figure 6.14 we plot the semimajor axis (perturbation size) as function of inclination, adopting the parameters obtained from RV analysis only and also the parallaxes from *Hipparcos* previous determination, $\pi_{abs}[\mathsf{HD\ 136118}] = 19.13 \pm 0.85\,\mathrm{mas}$ (PERRYMAN et al., 1997) and $\pi_{abs}[\mathsf{HD\ 33636}] = 34.9 \pm 1.3\,\mathrm{mas}$ (PERRYMAN et al., 1997).

From Figure 6.14 we notice that HD 136118 b, for inclinations below the limit $i \lesssim 25°$ (similarly $i \gtrsim 155°$), would produce a detectable astrometric signal at the limit of 1 mas. We can also notice that even if the nuisance orbit, found in the HD 136118 RV data is confirmed as a companion to the system, it would produce an undetectable astrometric signal, therefore we do not expect to confirm this detection with our FGS astrometry data. Figure 6.14 also shows the perturbation size of HD 33636 b, which presents a detectable astrometric signal for almost all possible inclinations.

Equation 6.2 provides not only a way to estimate the orbit size, but also an important constraint between RV and astrometry data. By imposing this equation we
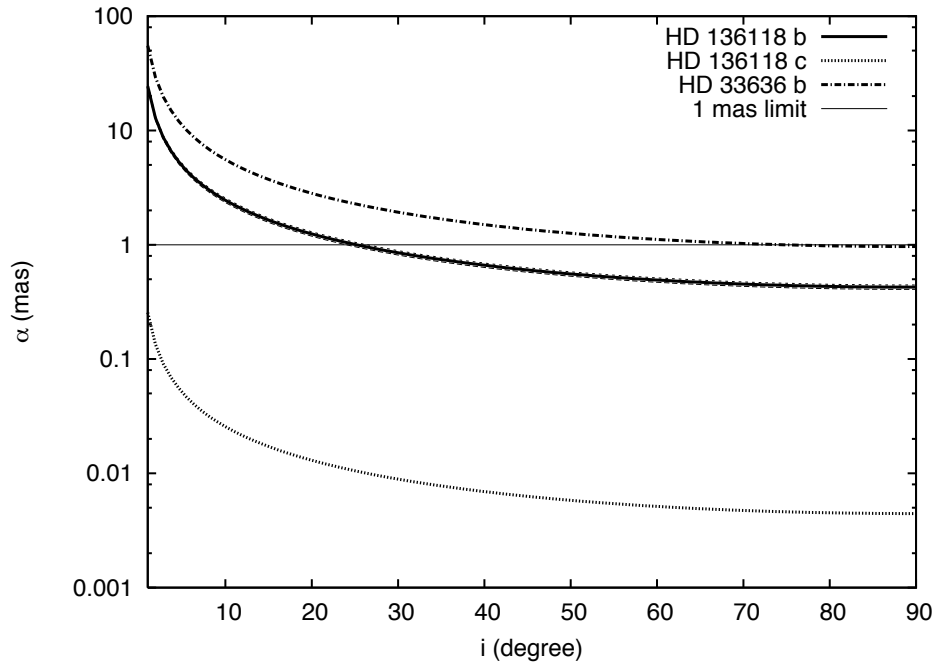
FIGURE 6.14 - Predicted orbit perturbation size α as function of orbital inclination i for HD 136118 b (solid line), HD 33636 b (dashed line) and the nuisance orbit (dotted line). The latter is identified as a possible component 'c' of HD 136118. The horizontal line represents a 1 mas detection threshold.

guarantee, for a certain degree, the agreement between RV and astrometry orbital solutions.

As we notice from Figure 6.14 the orbit contribution is extremely small, and if detectable, it will lie close to the FGS detection limit. Therefore, we first perform a fit to the FGS data without the orbit, and after we include the orbit with all possible constraints, so our search will be restricted to a very specific orbit signal and therefore it will not result in doubtful solutions. In fact, although our FGS data may be precise enough to detect such small signals, the observations do not cover the entire companion's orbit neither the parallactic orbit. This situation requires the use of "a priori" knowledge of the parallax through either a previous determination (e.g. from *Hipparcos*) or spectro-photometric independent determination.

6.2.0.2 Spectro-Photometric Parallaxes

We first call attention to the fact that the target's parallax obtained from relative astrometry is a relative measure with respect to the reference stars, each of which has its own parallax. For this reason, in order to obtain absolute, not relative parallax, we must either apply a correction from relative to absolute parallax or estimate the absolute parallaxes of reference stars by other means. We have already mentioned that absolute parallaxes can be determined independently through the photometric and spectral information of each star, from the definition of distance modulus. The so-called spectro-photometric absolute parallax can be calculated through the following expression,

$$\pi_{abs} = 10^{-(V-M_V-A_V+5)/5},\tag{6.3}$$

where V is the magnitude in the V-band, A_V is the extinction, and M_V is the absolute magnitude. In principle, M_V can be obtained from the color, spectral type and luminosity class of each star. Because this is an additional and important constraint to be used as prior in our models, we have also carried out independent photometric and spectroscopic observations of FGS reference-frame stars.

The spectra were obtained at the KPNO 4 m Telescope and the photometric data at the NMSU 1 m telescope in 2006 May. Tables 6.10 and 6.11 summarize spectral and photometric information for HD 136118 and HD 33636 astrometric reference stars. Tables 6.10 and 6.11 also show the derived spectro-photometric parallaxes.

TABLE 6.10 - HD 136118: classification spectra and photometric information for the astrometric reference stars.

Star	Sp Ty	V	$B-V$	M_V	A_V	π_{abs} (mas)
HD 136118	F9V	6.93	0.55	3.34	0.0	19 ± 4
REF-14	K0V	13.95	0.86	5.88	0.12	2.6 ± 0.8
REF-16	G0V	12.46	0.73	4.2	0.45	2.7 ± 0.8
REF-17	K0.5III	13.55	1.13	0.65	0.21	0.3 ± 1.0

The spectro-photometric parallaxes in Tables 6.10 and 6.11 are adopted as priors in our models unless there is any better determination of these quantities available, as

TABLE 6.11 - HD 33636: classification spectra and photometric information for the astrometric reference stars.

Star	Sp Ty	V	$B - V$	M_V	A_V	π_{abs} (mas)
HD 33636	G0V	7.06	0.58	(4.77)	(0.0)	34.9 ± 1.3
REF-47	F6V	15.23	0.64	3.56	0.50	0.6 ± 0.1
REF-55	F6V	14.08	0.59	3.56	0.37	0.9 ± 0.2
REF-57	K6V	15.31	1.25	7.28	0.06	2.6 ± 0.5
REF-58	G2V	13.06	0.61	4.56	0.05	2.0 ± 0.4
REF-60	K3III	9.92	1.30	0.27	0.05	1.2 ± 0.2

is the case of our targets, which have *Hipparcos* measurements (see Section 6.2.0.4).

6.2.0.3   Proper Motion

Proper motions are obtained from the NOMAD catalog (ZACHARIAS et al., 2005) and the UCAC-3 catalog (ZACHARIAS et al., 2010), for which the values and respective positions and additional information are listed in Tables 6.12 and 6.13. The proper motions are also included as observations with errors, but FGS measurements are more precise than any catalog based on ground-based observations, therefore we expect to improve these quantities.

TABLE 6.12 - HD 136118, HD 33636, and the astrometric reference stars information from the NOMAD catalog (ZACHARIAS et al., 2005).

Star	NOMAD ID	RA(2000)	DEC(2000)	μ_α (mas yr^{-1})	μ_δ (mas yr^{-1})	B	V	R
HD136118	0884-0265533	15:18:55.4718	-01:35:32.591	-124.0 ± 0.8	23.5 ± 0.6	7.432	6.945	6.630
REF-14	0883-0281420	15:18:57.4353	-01:37:40.726	-9 ± 6	6 ± 6	14.640	13.970	13.030
REF-16	0884-0265573	15:19:04.3421	-01:35:25.289	-1 ± 6	-7 ± 6	13.100	12.630	12.000
REF-17	0883-0281398	15:18:53.6195	-01:36:31.821	-5 ± 6	-5 ± 6	14.480	13.640	12.980
HD33636	0944-0053995	05:11:46.449	+04:24:12.74	180.8 ± 1.0	-137.3 ± 0.8	7.559	6.990	6.600
REF-47	0943-0054186	05:11:51.175	+04:23:45.95	11 ± 6	-14 ± 6	14.780	14.620	14.720
REF-55	0944-0054026	05:11:51.041	+04:24:13.84	-13 ± 6	-8 ± 6	14.340	-	-
REF-57	0944-0054038	05:11:52.954	+04:27:24.00	-5 ± 6	4 ± 6	15.700	14.920	14.460
REF-58	0944-0054066	05:11:58.555	+04:26:17.03	-0.8 ± 2.0	-0.7 ± 2.0	13.400	13.000	12.550
REF-60	0944-0054097	05:12:02.307	+04:26:32.02	1.1 ± 1.6	-7.1 ± 1.3	11.335	9.964	9.100

6.2.0.4   *Hipparcos* Data for the Targets

Perryman et al. (1997) present a catalog with the reduction of *Hipparcos* data. This contains parallaxes and proper motion values for both of our targets, HD 136118 and HD 33636. This determination is more accurate than any other work. van Leeuwen (2007) has recently presented a new reduction of *Hipparcos* data that presents an overall improvement. The parallaxes and proper motions for our targets from both

TABLE 6.13 - HD 136118, HD 33636, and the astrometric reference stars information from the UCAC-3 catalog (ZACHARIAS et al., 2010).

Star	UCAC-3 ID	RA(2000)	DEC(2000)	μ_α (mas yr^{-1})	μ_δ (mas yr^{-1})	J	H	K
HD 136118	177-135412	229.7311074	-01.5922470	-125 ± 13	30 ± 13	5.935	5.694	5.599
REF-14	177-135414	229.7393086	-01.6279823	-16 ± 7	6 ± 7	12.266	11.918	11.782
REF-16	177-135423	229.7680912	-01.5903600	7 ± 7	13 ± 7	10.963	10.654	10.532
REF-17	177-135407	229.7234153	-01.6088389	-18 ± 7	-11 ± 7	11.442	10.896	10.808
HD 33636	189-021417	077.9435289	+04.4034978	180.0 ± 1.0	-138.0 ± 1.0	5.931	5.633	5.572
REF-47	189-021432	077.9632321	+04.3961034	8 ± 10	-5 ± 10	13.995	13.701	13.595
REF-55	189-021431	077.9626727	+04.4038487	17 ± 9	-11 ± 9	-	-	-
REF-57	189-021437	077.9706595	+04.4566664	4 ± 11	-1 ± 10	12.910	12.249	12.136
REF-58	189-021464	077.9939842	+04.4380659	-1.0 ± 2.2	-0.3 ± 2.1	11.873	11.553	11.526
REF-60	189-021479	078.0096071	+04.4422239	-0.7 ± 0.7	-9.1 ± 0.9	7.650	6.988	6.813

catalogs are shown in Table 6.14.

TABLE 6.14 - HD 136118 and HD 33636 astrometric information from the *Hipparcos* catalog (PERRYMAN et al., 1997; VAN LEEUWEN, 2007).

Star	Reference	π_abs (mas)	μ_α (mas yr^{-1})	μ_δ (mas yr^{-1})	$B - V$
HD 136118	Perryman et al. (1997)	19.1 ± 0.8	-124.1 ± 0.9	23.5 ± 0.7	0.553
HD 136118	van Leeuwen (2007)	21.5 ± 0.5	-122.7 ± 0.6	23.7 ± 0.5	0.553
HD 33636	Perryman et al. (1997)	34.9 ± 1.3	180.8 ± 1.1	-137.3 ± 0.8	0.588
HD 33636	van Leeuwen (2007)	35.3 ± 1.0	179.7 ± 0.9	-138.4 ± 0.6	0.588

6.3 Combining Astrometry, Radial Velocity, and Priors

The framework for obtaining an overall solution simultaneously from RV and astrometry data is summarized below.

1. Obtain an independent fit for the RV parameters.

2. Set priors, which comprise the observed spectro-photometric parallaxes or, if available, any previous determination of parallaxes, and proper motions from catalogs.

3. Constrain one plate by setting its position as zero, with no scaling and no rotation.

4. Set the constraint relationship between RV and astrometry orbit parameters (Equation 6.2).

5. Given the astrometric priors one can search for an astrometric independent solution in order to obtain an initial set of plate constant values. Notice that the perturbation orbit parameters should not be included in this step.

117

6. Finally, run GaussFit including all these constraints, priors and observed data, with all parameters free, in order to obtain the best fit model for astrometry and radial velocity simultaneously. The GaussFit model for this analysis is available in the Appendix in Chapter 10.

6.3.1 Results

Notice that we have listed two catalogs, NOMAD and UCAC-3, each of which provides proper motions for the reference stars (Tables 6.12 and 6.13). We have also listed two *Hipparcos* reductions (Perryman et al. (1997) and van Leeuwen (2007)), which provide target parallaxes and proper motion (Table 6.14). FGS astrometry data is more precise than any of these catalog data, however our sampling does not suffice to obtain an independent value for neither the parallaxes nor the proper motions. For this reason we use the catalog information as priors in our analysis. Notice that the proper motion values for the HD 33636 reference stars in the two catalogs contradict each other. We prefer in this case to use only the UCAC-3 values.

Figure 6.15 and 6.16 show the reduced astrometric data. The data are shown separately for each star plotted together with the resulting parallax and proper motion models. We also show the proper motion and the parallactic orbit components of the model separately. The parallaxes, proper motion and statistics of residuals are shown in Tables 6.15 and 6.16. Figure 6.17 shows the histogram of astrometric residuals in X and Y FGS positions from all reference stars. We also show a Gaussian fit to each residual distribution, each of which indicates the corresponding FWHM (σ) and the mode.
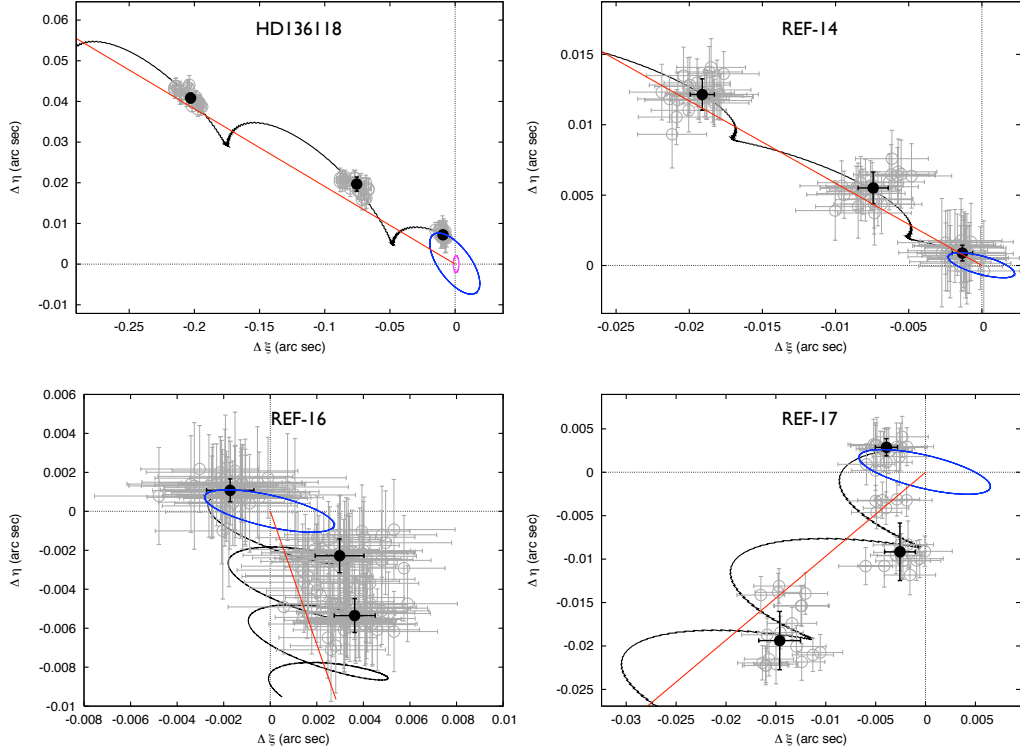
FIGURE 6.15 - Open circles are the reduced astrometry data for HD 136118 (top left panel) and for the astrometric reference stars. Filled circles show the median for clumps with 100 data points. Black lines show the fit model for the apparent path of each star. Each component of this model is also shown separately: blue lines for the parallax, red lines for the proper motion, and magenta line for the perturbation orbit.

TABLE 6.15 - Resulting astrometric catalog for HD 136118 from the RV and astrometry simultaneous fit.

Star	ξ (arcsec)	η (arcsec)	μ_α(mas yr^{-1})	μ_δ(mas yr^{-1})	π_{abs}(mas)
HD 136118	59.7255 ± 0.0018	659.3267 ± 0.0014	-123.6 ± 0.4	23.59 ± 0.19	19.9 ± 0.6
Ref-14	16.4100 ± 0.0023	783.7946 ± 0.0017	-12 ± 3	7.0 ± 2.2	2.3 ± 0.4
Ref-16	-72.6607 ± 0.0022	638.4372 ± 0.0029	1 ± 3	-3 ± 4	2.9 ± 0.4
Ref-17	80.4887 ± 0.0014	721.3350 ± 0.0015	-10.9 ± 2.0	-10.6 ± 2.0	6.8 ± 1.5
Statistical Quantities:					

Algorithm	χ^2	DOF	χ^2_ν	RMS$_X$	RMS$_Y$
LM	313.17	635	0.49	1.07 mas	1.40 mas
Robust	80.38	631	0.13	1.10 mas	1.36 mas

119
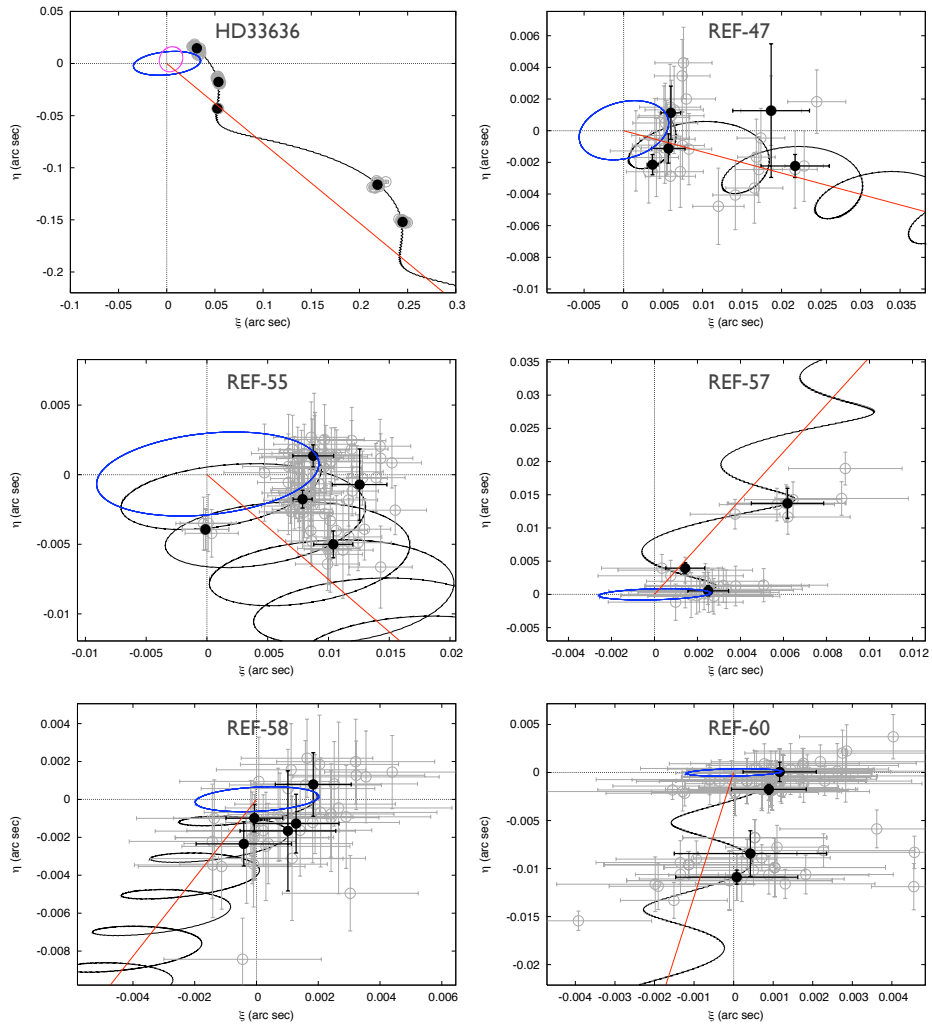
FIGURE 6.16 - Open circles are the reduced astrometry data for HD 33636 (top left panel) and for the astrometric reference stars. Filled circles show the median for clumps with 40 data points. Black lines show the fit model for the apparent path of each star. Each component of this model is also shown separately: blue lines for the parallax, red lines for the proper motion, and magenta line for the perturbation orbit.

120

TABLE 6.16 - Resulting astrometric catalog for HD 33636 from the RV and astrometry simultaneous fit.

Star	ξ (arcsec)	η (arcsec)	μ_α(mas yr^{-1})	μ_δ(mas yr^{-1})	π_{abs}(mas)
HD 33636	13.772 ± 0.004	789.791 ± 0.004	180.3 ± 0.4	-137.8 ± 0.3	34.98 ± 0.28
Ref-47	-49.7357 ± 0.0009	828.4899 ± 0.0006	12 ± 4	-2 ± 4	5.70 ± 0.03
Ref-57	-117.0620 ± 0.0009	619.2937 ± 0.0007	4 ± 5	13 ± 8	2.60 ± 0.15
Ref-60	-244.5390 ± 0.0004	696.8457 ± 0.0003	-0.70 ± 0.23	-9.0 ± 0.3	1.20 ± 0.06
Ref-55	-53.0216 ± 0.0006	800.7207 ± 0.0004	4 ± 4	-3 ± 3	9.20 ± 0.06
Ref-58	-186.6731 ± 0.0005	700.8105 ± 0.0004	-0.9 ± 0.9	-1.9 ± 1.5	2.01 ± 0.12
Statistical Quantities:					

Algorithm	χ^2	DOF	χ^2_ν	RMS$_X$	RMS$_Y$
LM	480.44	711	0.68	1.62 mas	1.19 mas
Robust	61.33	711	0.086	1.67 mas	1.21 mas
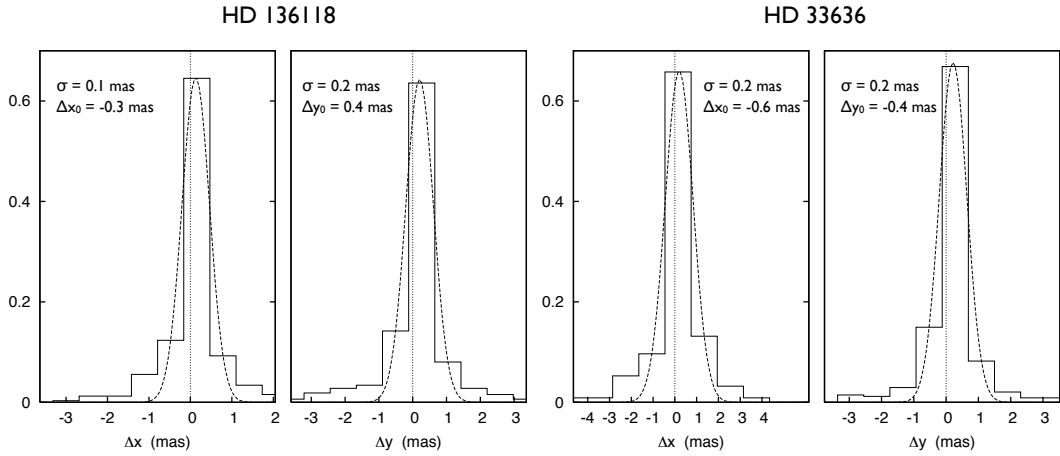
FIGURE 6.17 - Histogram of astrometric residual data for FGS X and Y positions for HD 136118 (left panels) and HD 33636 (right panels).

Fig 6.18 shows the reduced star positions $\Delta\xi$ and $\Delta\eta$, versus time for HD 136118. Although our solutions were obtained considering each data point individually, in Fig 6.18, in order to provide the reader a better visualization to show how the fit works, we also plot normal points which are the median and respective standard deviation of the mean of each clump of data, representing 3 different epochs. These collapsed points are also shown on Fig 6.19, where we plotted $\Delta\xi$ versus $\Delta\eta$ and the apparent orbit fit model.
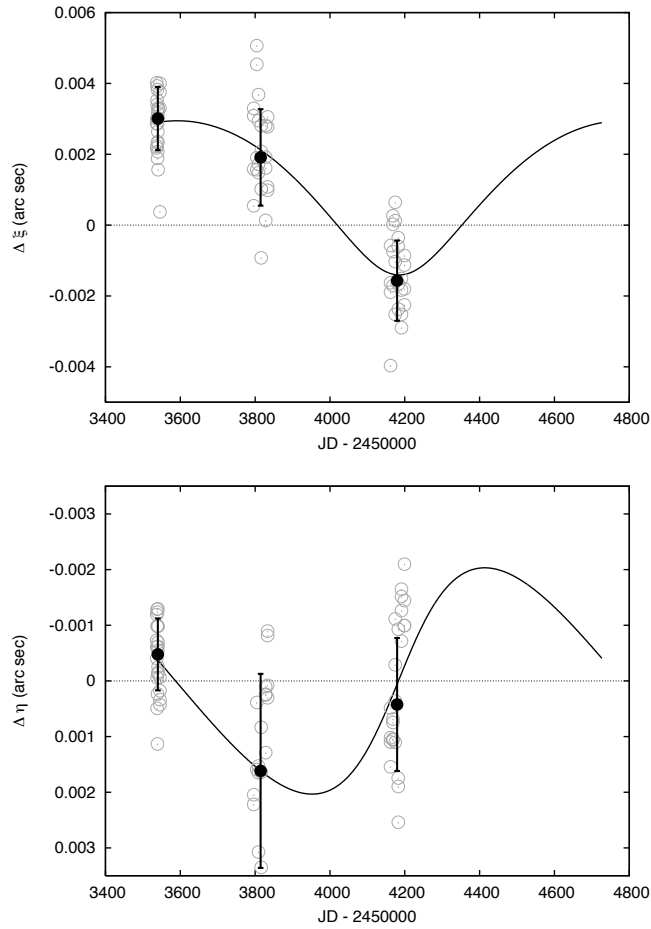
FIGURE 6.18 - $\Delta\xi$ and $\Delta\eta$ components of HD 136118 perturbation orbit versus time.

For HD 136118 we obtain a semimajor axis of the perturbation orbit $\alpha_s = 2.2 \pm 0.8$ mas, an inclination $i = 169° \pm 4°$ and a longitude of the ascending node $\Omega =$
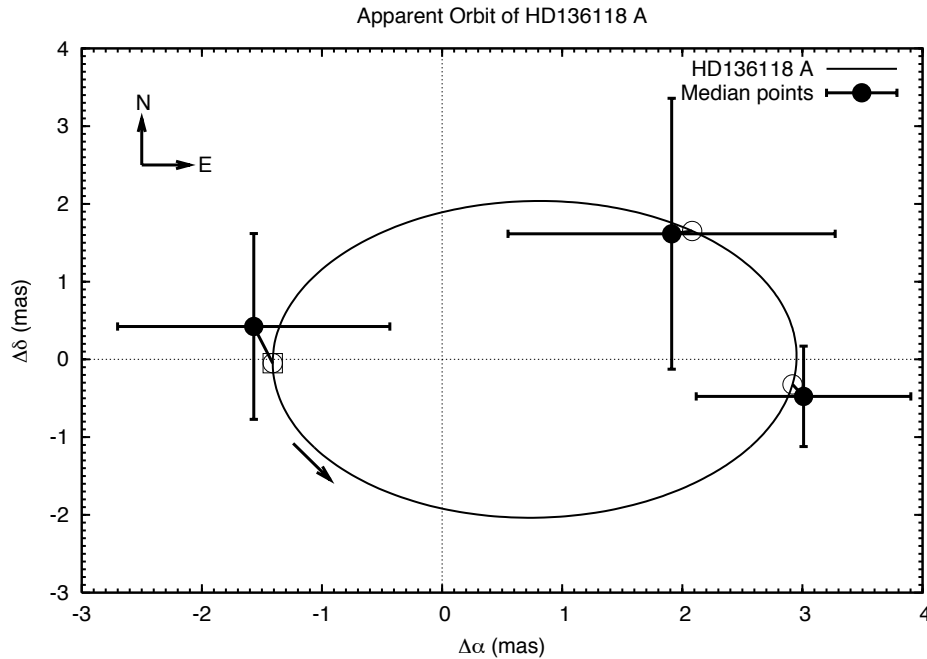
FIGURE 6.19 - Filled circles with error bars are the median and standard deviation of three groups of astrometric residuals of HD 136118, representing three different epochs. Solid line is the fit model of the apparent perturbation orbit of HD 136118. Open circles are the positions calculated from the fit model, each of which is connected by a thick solid line to its respective observed epoch. The open square shows the predicted position of the periastron passage.

227°±39°. A summary containing all HD 136118 b and the nuisance orbit parameters derived from the simultaneous RV and astrometry solution is shown on Table 6.17. Notice that all RV parameters have been improved. The statistics of RV residual data is similar to that shown in Table 6.3 and the final χ^2 is the one shown in Table 6.15.

For HD 33636 we have performed a similar analysis except that we consider a one-companion model. The results are presented in Table 6.18. The resulting apparent orbit model and the astrometric residual data are shown in Figure 6.20.

Apparent Orbit of HD33636 A
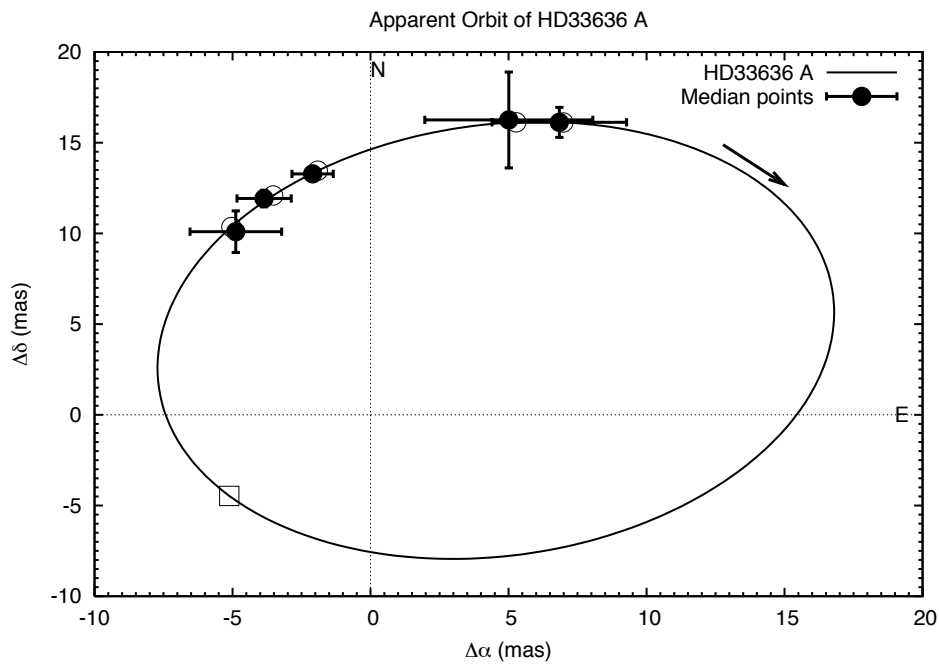
FIGURE 6.20 - Filled circles with error bars are the median and standard deviation of five groups of astrometric residuals of HD 33636, representing five different epochs. Solid line is the fit model of the apparent perturbation orbit of HD 33636. Open circles are the positions calculated from the fit model, each of which is connected by a thick solid line to its respective observed epoch. The open square shows the predicted position of the periastron passage.

TABLE 6.17 - HD 136118: best-fit parameters for a two-companion model from the simultaneous RV and astrometry data analysis.

	HD 136118 b	Nuisance orbit
Orbital parameters:		
P (days)	1190.8 ± 1.2	255.3 ± 1.1
T (JD)	2450611 ± 4	2453761 ± 5
e	0.353 ± 0.005	0.51 ± 0.08
ω (°)	316.5 ± 0.6	198 ± 11
K (m s^{-1})	215.8 ± 0.9	11.3 ± 1.3
Derived parameters from RV:		
$M \sin i$ (M$_J$)	12.2 ± 0.5 (3.77%)	0.35 ± 0.05 (12.82%)
$M \sin i$ (M$_\odot$)	0.0117 ± 0.0004 (3.77%)	0.00033 ± 0.00004 (12.82%)
$a \sin i$ (AU)	2.35 ± 0.16 (6.81%)	0.85 ± 0.17 (20.60%)
Astrometric quantities:		
α_s (mas)	2.2 ± 0.8	–
i (°)	169 ± 4	–
Ω (°)	227 ± 39	–
a_s (AU)	0.11 ± 0.04	–
Derived parameters from Astrometry:		
M_p (M$_J$)	63^{+22}_{-13}	–
M_p (M$_\odot$)	$0.060^{+0.021}_{-0.012}$	–
a_p (AU)	2.29 ± 0.04	–
Systemic velocities (m s^{-1}):		
$\Gamma_{Lick1} = -1.5 \pm 2.2$		
$\Gamma_{Lick2} = -12 \pm 7$		
$\Gamma_{HET} = 485.5 \pm 0.8$		

TABLE 6.18 - HD 33636: best-fit parameters from the simultaneous RV and astrometry data analysis.

	HD 33636 B
Orbital parameters:	
P (days)	2118 ± 5
T (JD)	2451198 ± 4
e	0.474 ± 0.004
ω (°)	337.7 ± 0.8
K (m s^{-1})	162 ± 1
Derived parameters from RV:	
M $\sin i$ (M$_{\mathrm{J}}$)	9.17 ± 0.19 (2.06%)
M $\sin i$ (M$_{\odot}$)	0.00875 ± 0.00018 (2.06%)
a $\sin i$ (AU)	3.23 ± 0.12 (3.68%)
Astrometric quantities:	
α_s (mas)	13 ± 4
i (°)	4.3 ± 1.4
Ω (°)	250 ± 20
a_s (AU)	0.37 ± 0.12
Derived parameters from Astrometry:	
M$_p$ (M$_{\mathrm{J}}$)	131^{+43}_{-26}
M$_p$ (M$_{\odot}$)	$0.125^{+0.041}_{-0.025}$
a$_p$ (AU)	$3.01^{+0.05}_{-0.07}$
Systemic velocities (m s^{-1}):	
$\Gamma_{Lick} = -36.8 \pm 1.7$	
$\Gamma_{Keck} = -33.1 \pm 0.9$	
$\Gamma_{HET} = 0.9 \pm 1.6$	
$\Gamma_{Elodie} = 156.5 \pm 1.0$	

6.4 Derivation of the True Mass and Semimajor Axis

By determining the inclination we are able to remove the previous degeneracy on the mass of the companions. However the true mass should not be calculated simply by replacing the inclination into the $M \sin i$ expression. Instead, one should calculate the actual mass by iterating Equation 3.43. Moreover one should take into account the uncertainties from all parameters in Equation 3.43. In order to do this we have calculated the mass 100,000 times, where the input parameters are chosen by a normal probability distribution with dispersion given by their uncertainties. This leads to an asymmetric probability distribution for the mass. Figure 6.21 presents the Cumulative Distribution Function (CDF) [1] for the masses of HD 136118 b and HD 33636 B. The abscissa corresponding to the 0.5 value in the CDF is the median. The 1-σ uncertainties are obtained from the 34.13% percentile areas. This yields the following true masses: $M_b = 63^{+22}_{-13}\,\mathrm{M_J}$ for HD 136118 b and $M_B = 131^{+43}_{-26}\,\mathrm{M_J}$ for HD 33636 B.

Analogously to the calculation of the mass, the physical semimajor axis may also be obtained through Equation 3.5. Figure 6.22 shows the CDF for the semimajor axes of both systems. This yields $a_b = 2.29 \pm 0.04\,\mathrm{AU}$ for HD 136118 b and $a_B = 3.01^{+0.05}_{-0.07}\,\mathrm{AU}$ for HD 33636 B.

6.5 Infrared Interferometry for HD 33636

The interpretation of interferometric observations depends strongly on the model adopted for the analysis. This model can be obtained from prior knowledge of the system. In our case we expect to be able to test the binary model (see Chapter 3) for HD 33636 A and its M-dwarf companion, HD 33636 B.

By making use of HD 33636 parameters obtained from RV and astrometry analysis (Table 6.18) we are able to estimate the expected signal in the interferometry experiment. The squared visibility model for a binary is given by Equation 3.61, which requires the assumption of a visibility function for each individual target. Figure 5.19 presents the squared visibility model for HD 33636 A, which is modeled as a disk-like source with diameter $\Theta_A \sim 0.38\,\mathrm{mas}$. According to the evolutionary model for very-low-mass stars with dusty atmospheres of Chabrier et al. (2000), the companion HD 33636 B, with mass $M_B = 0.125^{+0.041}_{-0.025}\,\mathrm{M_\odot}$, has a physical diameter

---

[1]The CDF is reflected vertically for values > 0.5
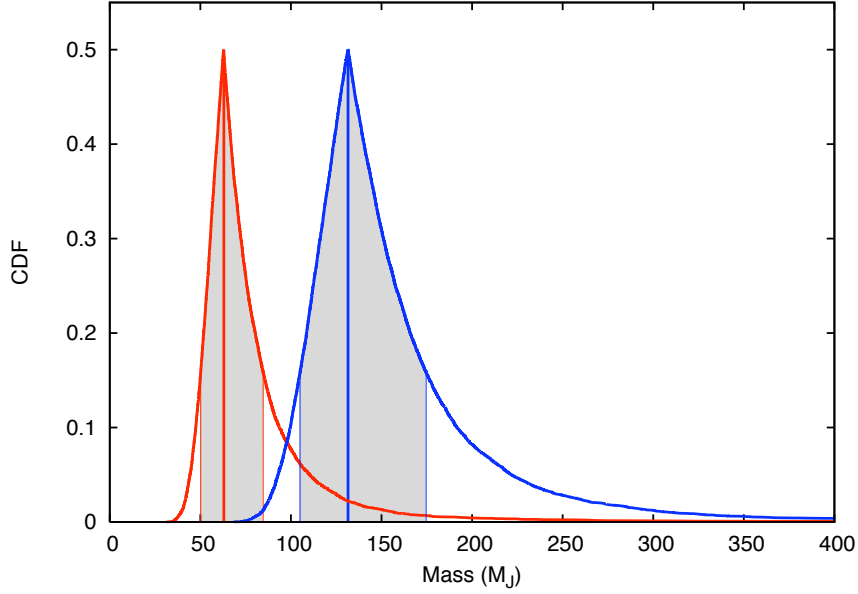
FIGURE 6.21 - CDF (reflected vertically for values > 0.5) for the masses of HD 136118 b (red curve) and HD 33636 B (blue curve). Filled in grey presents the region within which we consider the uncertainty on the mass measurement.

$D < 0.3\,\mathrm{R_\odot}$, which implies an apparent angular size of $\Theta_B < 0.1\,\mathrm{mas}$. The latter produces a negligible signal in the visibility for the spatial frequencies considered in our experiment. Therefore we use a binary model consisted of an uniform disk for the central star and a point-like source for the companion.

The parameters involved in the interferometric model are the flux ratio between components A and B, $f = F_B/F_A$, and the binary parameters, ρ and θ, which can be estimated from our previous orbital results. Figure 6.23 shows the orbit of the two components in the system. The angular separation between the two bodies is $\rho = 157.22\,\mathrm{mas}$ and the position angle is $\theta = 255°.98$. These values are input as initial guesses to fit the interferometric data.

We performed a fit using GaussFit, which provided the flux ratio $f = 0.323 \pm 0.025$, the binary separation, $\rho = 169.52 \pm 0.11\,\mathrm{mas}$, and the position angle $\theta = 269°.03 \pm 0.16$. The squared visibility data points and the fit model are shown in Figure 6.24.
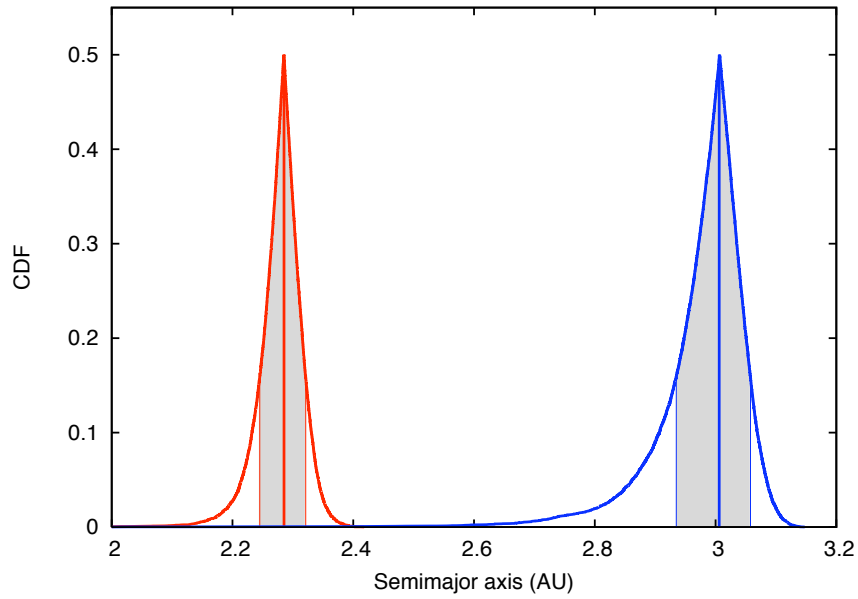
FIGURE 6.22 - CDF (reflected vertically for values > 0.5) for the semimajor axes of HD 136118 b (red curve) and HD 33636 B (blue curve). Filled in grey presents the region within which we consider the uncertainty on the semimajor axis measurement.

6.5.1 Interferometric Phase and Closure Phase

Figure 6.25 shows the reduced interferometric phases and Figure 6.26 shows the reduced closure phases for HD 33636. One can notice that the phase and closure phase variations for HD 33636 are consistent with a symmetrical brightness distribution, i.e. constant phase. The filled circles show the median and respective deviations for clumps of 15 points.
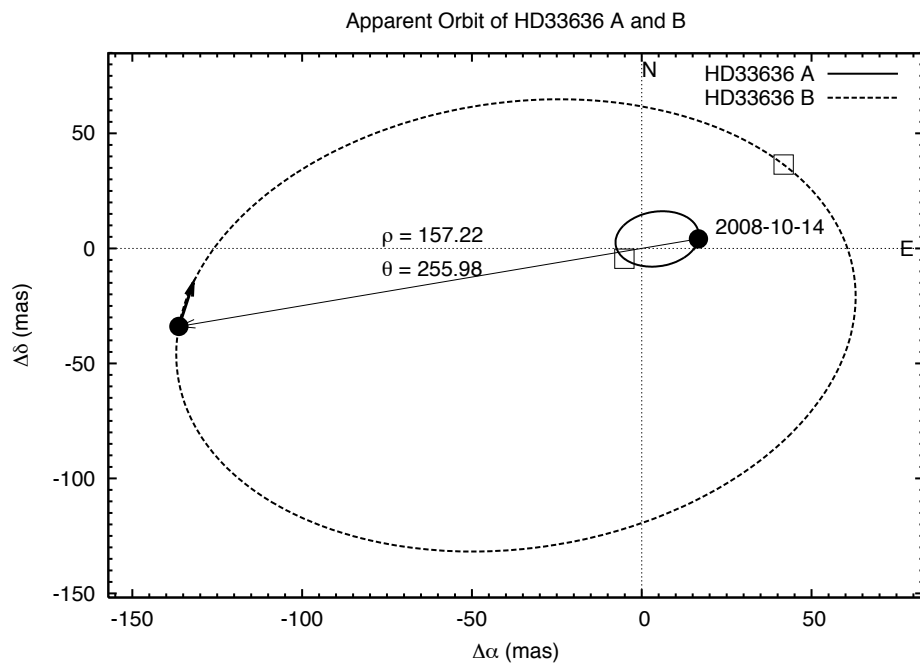
FIGURE 6.23 - Apparent orbit of HD 33636 A (solid line) and B (dashed line). Filled circles show the predicted positions for each component in UT 2008-10-14. The periastron is indicated with open squares.
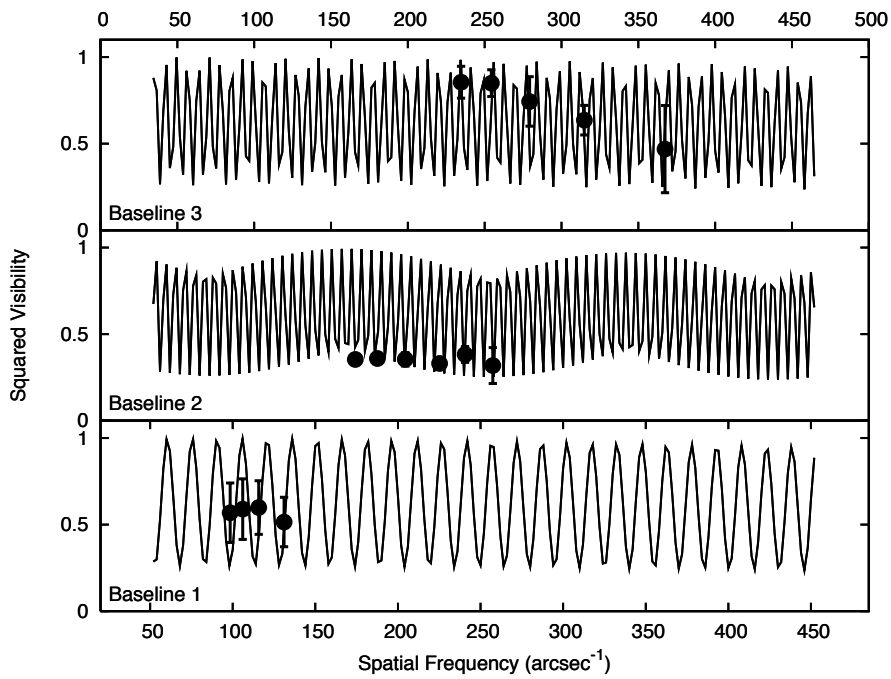
FIGURE 6.24 - Squared visibility reduced data (filled circles) for the three baselines and the best fit model (solid line). The model consists of a binary with a disk-like source with size $\Theta_A = 0.38$ mas plus a point-like source. The fit parameters are the flux ratio, $f = 0.323 \pm 0.025$, the binary separation, $\rho = 169.52 \pm 0.11$ mas, and the position angle $\theta = 269°.03 \pm 0.16$.
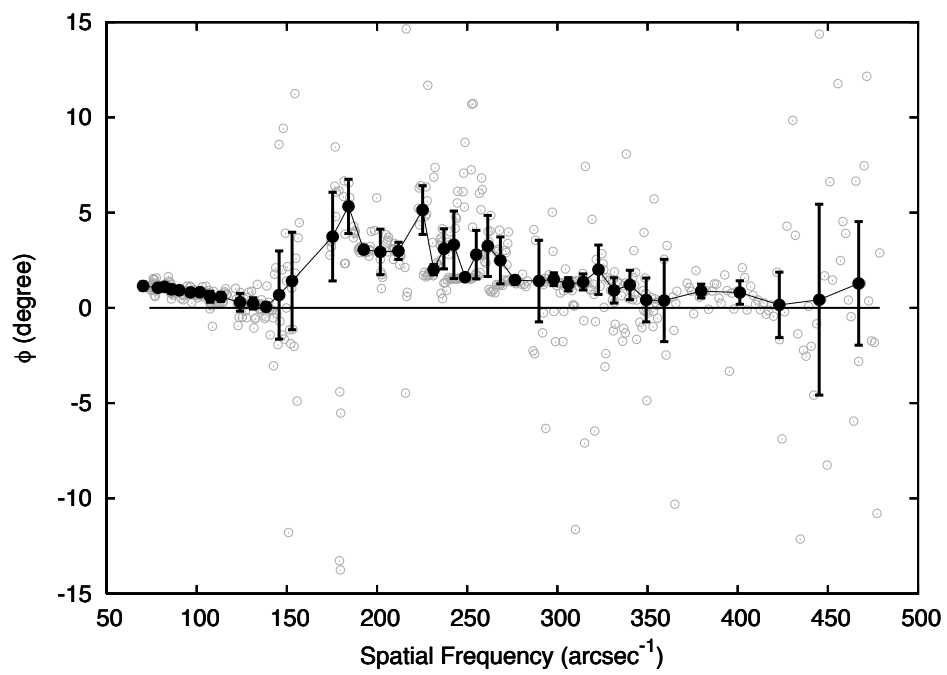
FIGURE 6.25 - Open circles are the reduced interferometric phases for HD 33636. Filled circles show the median taken over clumps containing 15 points.
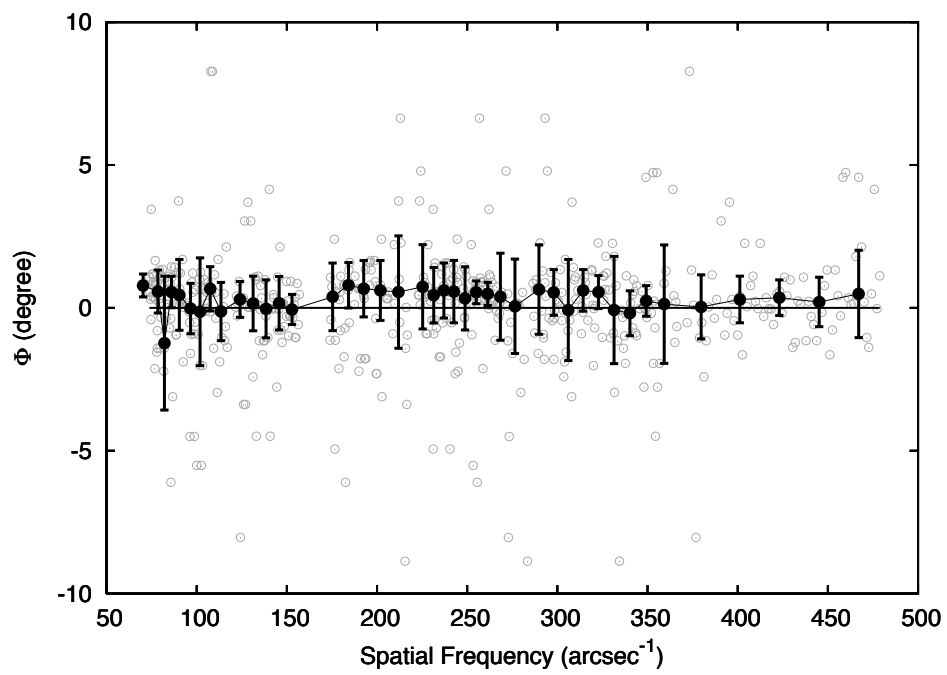
FIGURE 6.26 - Open circles are the reduced closure phases for HD 33636. Filled circles show the median taken over clumps containing 15 points.

7 RESULTS AND DISCUSSIONS

7.1 HD 136118

The HD 136118 system has an RV-detected companion confirmed by our HRS/HET RV measurements. We have also detected an additional signal in our RV data with amplitude near the limit of our instrument sensitivity. Our FGS/HST astrometry allowed us to determine the complete set of orbital parameters of the known companion, which permit us to calculate the actual mass of this companion. This has been identified as a likely brown dwarf companion.

7.1.1 Activity in HD 136118

Stellar chromospheric activity can produce radial velocity variations. These could add either noise or periodic signals to the RV data. Observations of Ca II H and K lines (FISCHER et al., 2002) indicate modest chromospheric activity for HD 136118, therefore not many spots should be expected. Using the Saar & Donahue (1997) relationship for the spot radial velocity amplitude versus filling factor: $A_S = 6.5 f_S^{0.9} v \sin i$, where f_S is spot filling factor in percent, $v \sin i$ is the projected velocity in km/s and A_S is the spot radial velocity amplitude in m/s. For the radial velocity amplitude of 216 m/s, and the measured velocity $v \sin i = 7 \pm 0.5$ km/s (BUTLER et al., 2006), we obtain a spot filling factor of about 6%, i.e. about 60 millimag variations. As shown in Benedict et al. (1998) and Nelan et al. (2010) the Fine Guidance Sensor itself is a millimag precision photometer. The variations we see in HD 136118 over 700 days are of the order of 4 parts per 1000, about 4 millimags, as shown on Fig 7.1. This implies only small variations in spectral line shapes, which typically introduces noise of the order of $5 - 10$ m/s in the velocities. Notice that the 255 d signal detected in the HET RV data has amplitude of 11.3 m/s, and its period is not correlated with any known star cycle.

7.1.2 HD 136118 Spin Axis and the Companion's Orbit Alignment

Fischer et al. (2002) have provided evidence that the stellar rotation period of HD 136118 is about 12.2 d. Given a stellar radius of $R = 1.58 \pm 0.11 \, R_\odot$ (PRIETO; LAMBERT, 1999) we calculate the maximum rotation speed at the stellar equator $v_{max} = 6.5 \pm 0.2$ km/s. The measured projected velocity $v \sin i = 7 \pm 0.5$ km/s is then consistent with the maximum speed. This suggests a very high inclination of the spin axis. Therefore, if the whole system follows the same angular momentum
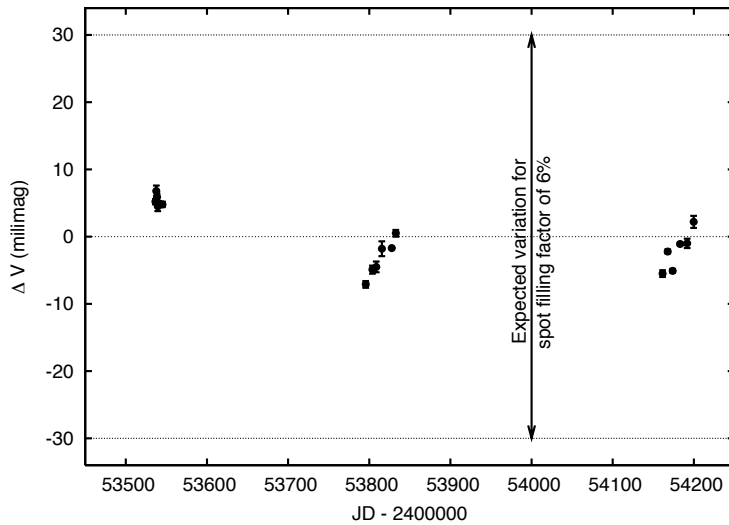
FIGURE 7.1 - FGS-1r photometry of HD136118. Magnitude variation is relative to the mean magnitude, V=6.93. Dashed lines show the amplitude of variation possible from a (single) spot filling factor of 6%, the spot filling factor required to produce the observed RV variation from HD136118 b (SAAR; DONAHUE, 1997).

orientation as that of the star, then the companion's orbit would be close to an edge-on orientation with respect to our line of sight.

Conversely, we found that HD 136118 b has an orbital inclination of $i = 169° \pm 4°$, nearly perpendicular to the inferred inclination of the stellar spin axis. This misalignment is a puzzling result since conservation of angular momentum would favor alignment between stellar spin and companion orbital axes, assuming both were formed in the same primordial cloud.

7.1.3   HD 136118 b: a Brown Dwarf Companion

HD 136118 b is likely a brown dwarf companion orbiting at 2.3 AU that falls in the so called 'brown dwarf desert' (GRETHER; LINEWEAVER, 2006). They showed that the frequency of companions in the stellar mass range follows a slope with gradient -9.1 ± 2.9, while in the planetary mass region, the gradient is 24 ± 5. These two separate linear fits intersect below the abscissa at $M = 43^{+14}_{-23}\,\mathrm{M_J}$. HD 136118 b mass is $M_b = 63^{+22}_{-13}\,\mathrm{M_J}$. Reffert & Quirrenbach (2006) measured astrometric masses

for two exoplanet candidates HD 38529 c ($M = 37^{+36}_{-19}\,\mathrm{M_J}$) and HD 168443 c ($M = 34 \pm 12\,\mathrm{M_J}$). Benedict et al. (2010) presented a more accurate measurement for the mass of HD 38529 c, $M = 17.6^{+1.5}_{-1.2}\,\mathrm{M_J}$. Both objects are likely brown dwarf companions around solar type stars like HD 136118 b. These are important cases for studying the mass function and evolutionary models at the brown dwarf mass range, as we explain below.

Most of brown dwarfs known to date are those detected through photometric surveys (DELFOSSE et al., 1999, e.g.). The masses of these objects are determined based on evolutionary models (BARAFFE et al., 1998) . These objects are also the main source of data for the construction of mass-functions and evolutionary tracks in the HR diagram for the brown dwarfs range (BARAFFE et al., 2002). However, there are a lot of uncertainties in these models, some of which raising, for example, from the age/mass degeneracy. Brown dwarfs in multiple systems with dynamical masses, like HD 136118 b, may have their ages calibrated with the age of the primary, assuming coevality. Therefore, these are important calibrators to improve the determination of evolutionary tracks. However, due to the high contrast between the companion and the primary, the luminosity of these companions are usually unknown. We have described in this thesis a method for this purpose, the infrared interferometry, which is shown to be a promising technique for the detection of the companion's flux signature in high contrast binaries. Below we make use of the current models to estimate the flux contribution from HD 136118 b.

According to Chabrier et al. (2000), Baraffe et al. (2002) evolutionary dusty model for brown dwarfs, assuming $M_b = 0.060^{+0.021}_{-0.012}\,\mathrm{M_\odot}$ and the age of the brown dwarf as 5 Gyr, HD 136118 b has a temperature of about $T_b = 1100\,\mathrm{K}$ and a radius of $R_b = 0.084\,\mathrm{R_\odot}$. If one considers the uncertainty in the age of the system (see Table 2.1), this brown dwarf may be much younger, therefore considering the age as 1 Gyr, HD 13118 b has a temperature of about $T_b = 1675\,\mathrm{K}$ and a radius of $R_b = 0.094\,\mathrm{R_\odot}$. These characteristics classifies HD 136118 b as either a L-dwarf, or if one considers the inferior mass limit, a T-dwarf. Using these values we calculate the emission and reflection spectra, and the flux ratio between the brown dwarf and the parent star as show in Fig 7.2. The flux ratio increases toward the far infrared (L, M and N bands), where it can get as high as 10^{-4}.
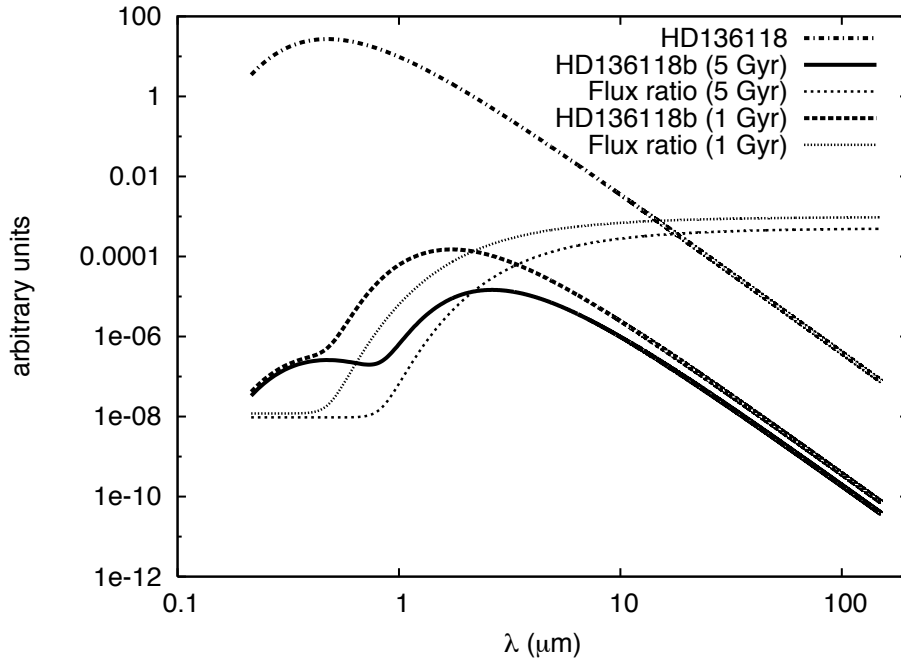
FIGURE 7.2 - Predicted emission spectrum of HD 136118 (dash-dotted line), emission/reflection spectrum of HD 136118 b and the flux ratio between the brown dwarf and the parent star for a 5 Gyr and 1 Gyr system age, as indicated in the legend.

7.1.4   HD 136118 c: A Possible New Planet?

We have detected a low-amplitude 255 days signal with orbit shape in the HD 136118 RV data. Such solution suggests the presence of an additional lower mass companion to the system. If confirmed, this is identified as a likely planetary companion with minimum mass $M_c \sin i = 0.35 \pm 0.05 \, \mathrm{M_J}$ and projection of semimajor axis $a \sin i = 0.85 \pm 0.17 \, \mathrm{UA}$. Furthermore, if this companion's orbit follows the same orientation as that of the brown dwarf companion, the true mass would be $M_c \sim 1.75 \, \mathrm{M_J}$.

Although it seems evident that this signal comes from an additional massive component, we call attention to the fact that this is a very eccentric orbit and considerably large $M \sin i$ planet, which lead us to conclude that such body could hardly coexist with a brown dwarf orbiting the same system at the distances they seem to be. In fact we have performed a dynamical stability analysis using the MERCURY pack-

138

age (CHAMBERS, 1999). We have input the two companions around HD 136118, and considered the minimum mass, which minimizes interactions. We also explored the full range of inclinations for the lower-mass component. The system always becomes unstable for very short time scales.

Besides the stability constraint, this detection is at the limit of our instrument, and also if we look at Fig 6.11 we note that only a few data points are contributing to form the orbit we have obtained. For these reasons we prefer to be cautious and take this as a "nuisance orbit" to fix an unknown source of systematic error present in the HET data, although the possibility of a second companion is not out of the question. Further observations are advised to investigate the origin of this signal.

7.2 HD 33636

7.2.1 RV and Astrometry Results

For HD 33636 we have used more constraints in our analysis than those used in Bean et al. (2007). This was possible because some of the priors we used have been published more recently than Bean's work. For this reason we have obtained slightly different values for the system parameters. These are different but consistent with each other. The mass we obtained for HD 33636 B is $M_B = 131^{+43}_{-26}\,M_J$, and the previous determination is $M_B = 142 \pm 11\,M_J$. The disagreement between the uncertainties is due to the fact that they have not been calculated in the same fashion. Although our mass is smaller than that obtained by Bean et al. (2007), the classification of this companion remains an M-dwarf star.

7.2.2 Reliability of our Interferometric Results

Notice that the minimum baseline used in our interferometry experiment provides the measurement at spatial frequency of about $100\,\text{arcsec}^{-1}$. This limits the interferometric field-of-view up to $\sim 10\,\text{mas}$. As one can see from Figure 6.23 the binary separation is $\rho \sim 160\,\text{mas}$, thus larger than the field-of-view. For this reason we consider that the fit shown in Figure 6.24 is not as definitive, thus we can not trust the fit parameters obtained from our analysis. In fact the visibility models for these spatial frequencies are oscillating functions of high frequency, which can easily produce aliases, reproducing the positions of those data points for basically any phase adopted in the model. From Equation 3.61 we notice that the angular variable, i.e. the term inside the cosine, is only affected by two parameters, the position angle, θ,

and the binary angular separation, ρ. The conclusion here is that unfortunately the interferometer baselines of our experiment do not provide an adequate sampling to provide information about these binary parameters.

However the variations in the observed visibility are clear. From Equation 3.61 we can also notice that the visibility amplitude is affected only by one parameter, the flux ratio. Variations in the visibility with this amplitude can only be reproduced by a binary brightness distribution with flux ratio of order of 30%.

Although we are positive about the detection of an additional light other than the primary star, we can not draw any conclusion about the morphology of this source only from the interferometric results. Therefore, we suggest three possible situations to explain the origin of this signal.

First we recall that even though the interferometer baseline separations do not sample larger spatial scales in the field-of-view, each individual telescope has an 8 m mirror, each of which is, in principle, able to sample smaller spatial frequencies. This fact may introduce contributions from the HD 33636 B luminosity to the detected signal.

Another possible explanation could be the presence of an additional light that comes either from a disk, a field-star or an additional inner companion. The disk hypothesis is supported by the fact that HD 33636 shows an excess emission at 70 μm (BEICHMAN et al., 2005), which is an evidence for a debris disk, possibly located at wider distances. The inner companion hypothesis is contradicted by the fact that radial velocity data do not present any expressive signal. This would limit the size of the companion to a very low-mass, thus less luminous source. The field-star hypothesis is a possibility that may be ruled out using future observations. HD 33636 is a high proper motion star (over $100 \, \mathrm{mas \, yr^{-1}}$), thus it would get away very rapidly from any "polluting" field-star.

7.2.3 Flux Ratio

Let us consider that the flux ratio between components A and B is given by the one measured in Chapter 6 from interferometry, $f \sim 30\%$. As for comparison we can calculate the same flux ratio from other means. Figure 7.3 presents the Baraffe et al. (1998) mass-magnitude diagram for low-mass stars, which provides the relationship between mass and absolute magnitude in the K-band. The models

correspond to an age of 5 Gyr, which is consistent with the age of HD 33636 (see Table 2.2). This relationship allows us to obtain the magnitude of the companion from its dynamical mass, and consequently we are able to calculate the flux ratio. Figure 7.3 also presents the position of HD 33636 B in this diagram, where the absolute magnitude has been calculated from the interferometric flux ratio.
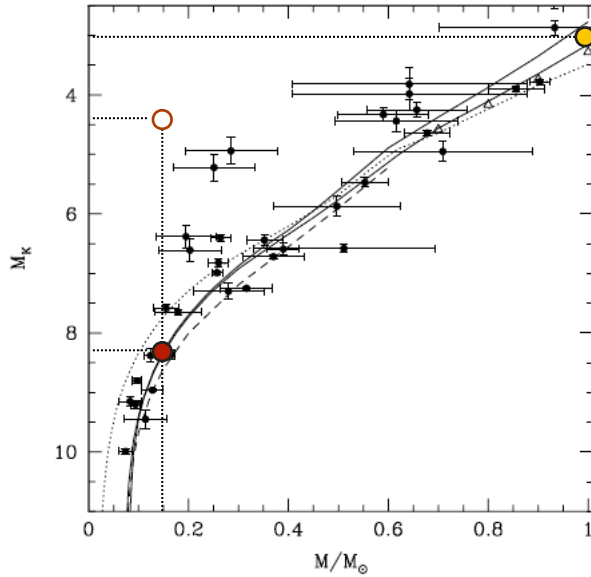
FIGURE 7.3 - Mass versus absolute magnitude in the K band for low-mass stars (BARAFFE et al., 1998). The models correspond to an age of 5 Gyr. The yellow filled circle shows the position of HD 33636 A. The red filled circle shows the predicted position of HD 33636 B from its dynamical mass. The red open circle shows the position of HD 33636 B considering both the dynamical mass and the infrared flux ratio obtained from interferometry.

Although the luminosity of the companion determined by each method seems to disagree, we call attention to the fact that the interferometric experiment has not been performed in ideal conditions. This suggests that further observations with more careful consideration of the spatial scales should be done. Below we discuss the experimental conditions that should provide more definitive results for HD 33636.

7.2.4 The Spectral Distribution of HD 33636 Components

Figure 7.4 presents the blackbody emission spectra of the two components of the HD 33636 system. The spectrum for the primary has been calculated from the parameters listed in Table 2.2, and the model spectrum for the companion has been

calculated with the aid of the evolutionary models for low-mass stars of Baraffe et al. (1998), Baraffe et al. (2002). We notice from Figure 7.4 that the flux ratio between components can reach up to only 1%, which is far from the 30% value obtained from interferometry.
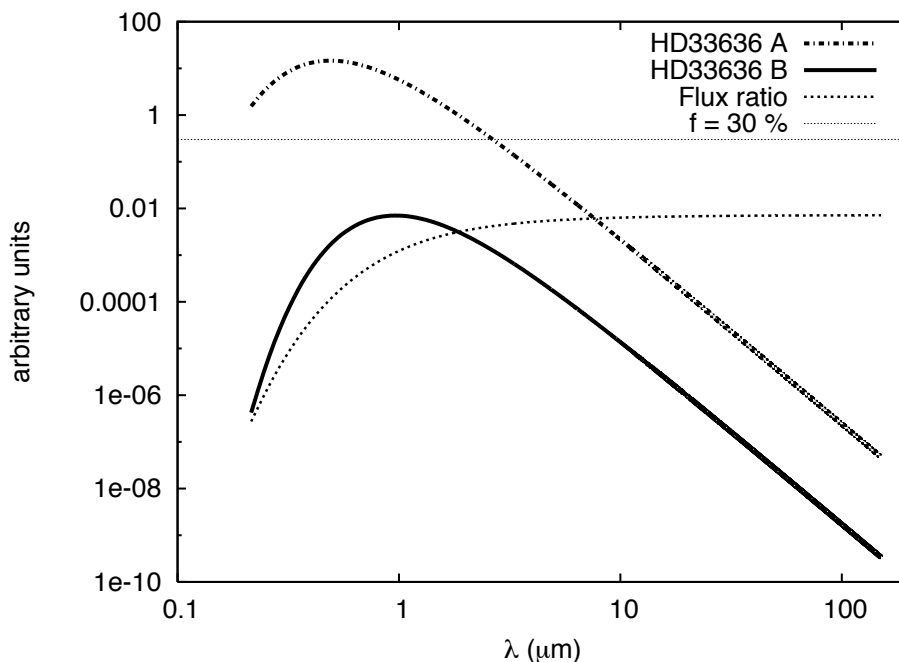
FIGURE 7.4 - Blackbody emission spectra of HD 33636 A (dash-dotted line) and HD 33636 B (solid line). The flux ratio between the two components and the limit where the flux ratio is 30% is shown in dotted lines.

7.2.5 What would be the Proper Interferometer Set Up to Study HD 33636?

We saw that our interferometry experiment was not adequate to investigate HD 33636. However, infrared interferometry is still a promising technique to study high-contrast binaries, like HD 33636. As an example we cite the Duvert et al. (2010) work, where they have used AMBER/VLTI to detect the 5-mag fainter companion of HD 59717 at a distance of 4 stellar radii. They present measurements for the squared visibilities that cover spatial frequencies between 50 and 250 arcsec^{-1}. This

is not very different from the range we observed. However, the difference is that for HD 59717, the first interferometric null of the visibility function of the primary star falls within the observed range of spatial frequencies. This enables one to inspect small deviations on the visibility function where the relative contribution from the companion is more expressive, i.e. around the null. The phase of the complex visibility function of the primary star also changes abruptly from 0 to π at the first null. This change is a step-like function for a single disk-like visibility function (see Equation 3.55). According to Equation 3.64 the effect of an additional light from the faint companion is the "smoothing out" of the phase function at the zero visibility crossing, i.e. around the null. The smaller the flux ratio, the smaller the spatial frequency range within which this "smoothing" happens. Notice that the alteration in the phase function is not dictated by the flux ratio, therefore the capacity of detection of a companion's signature depends only on how fine you can sample spatial frequencies around the null. We refer the reader to the work of Chelli et al. (2009), where they explore the detectability of faint companions in a broader context. Below we apply the concepts developed in Chelli et al. (2009) to provide a brief discussion on the interferometer set up needed to detect HD 33636 B.

The spatial frequency at the first null for a disk-like visibility function given by Equation 3.55 is

$$u_0 = \frac{0.61}{R_\star}, \tag{7.1}$$

where $R_\star$ is the star radius in angular units. Therefore, for the radius of HD 33636 A that we have estimated in Chapter 5, $\Theta = 0.383\,\text{mas}$, the first null falls at frequency $\sim 1600\,\text{arcsec}^{-1}$. From Equation 3.46 we calculate that the baseline required to observe frequencies around this value is $B = 330\lambda$, where λ is the wavelength in μm. Thus, for $\lambda = 1\,\mu$m one needs a baseline of $330\,\text{m}$ to probe the first visibility null of HD 33636 A. The maximum baseline supported by VLTI is only $200\,\text{m}$ and the Keck Interferometer (KI) baseline is $85\,\text{m}$.

Therefore, with these instruments one can not reach spatial frequency scales large enough to probe the first null of the visibility function of HD 33636 A. Let us check now whether one can sample the smaller frequencies to probe the binary signature. The binary separation is $\rho \sim 160\,\text{mas}$, therefore one needs to sample the visibility function at spatial frequencies of about $5\,\text{arcsec}^{-1}$ in order to provide a field-of-view

that allows the measurement of the binary pair without alias. This frequency is reached for a baseline of about 1.3 m. This means that we do not necessarily need an interferometer to measure the pair. Instead one can use a monolithic instrument with aperture larger than ~ 2 m. For ground-based observations one would need an Adaptive Optics (AO) system in order to correct for atmospheric blurring. The instrument would also need a coronagraph, so that the high contrast could be minimized.

8 SUMMARY AND CONCLUSIONS

Our spectroscopic data provide radial velocities for HD 136118 with precision better than 5 m/s. These velocities have been combined with archival data to confirm the presence of the exoplanet candidate companion HD 136118 b. Our analysis revealed an additional low amplitude 255 d signal with a typical orbital shape. We conclude that this is not a positive detection of an additional companion to the system, but we strongly suggest further observations and/or improvement on data reduction methods to test the reality of this signal. If this companion is confirmed, according to the orbit fit we obtained the minimum mass $M_c \sin i = 0.35 \pm 0.05\, M_{\rm J}$, thus a likely planetary companion.

Our FGS/HST astrometry combined with radial velocity data allows the thorough characterization of the perturbation orbit of HD 136118 due to its known companion HD 136118 b. This allowed us to determine the actual mass of this object, $M_b = 63^{+22}_{-13}\, M_{\rm J}$, in contrast to the minimum mass obtained from the radial velocity data alone, $M_b \sin i \sim 12\, M_{\rm J}$. Therefore, given that its mass is above the $13\, M_{\rm J}$ limit, it is not a planetary but a likely brown dwarf companion. This makes it an important object for studying the initial mass function for brown dwarfs and low-mass stars, since it provides the dynamical mass of an object that seems to be residing in the "brown dwarf desert". The confirmation of an additional planetary body to this system would make it an even more interesting case of study. Our long-term dynamical stability analysis that includes a third body in the system has presented severe constraints due to the strong interactions between the brown dwarf and the possible planetary companions.

We have accessed the published RV and FGS/HST data from HD 33636, for which we have used newer determinations for the astrometric priors in order to perform the analysis of these data using the same methods as those we used to analyze HD 136118 data. From the HD 33636 results we were able to compare with previously published results and conclude that our analysis is reliable. The new set of priors provided slightly different values that agree with previous results. This has also permitted us to improve the proper motion and parallaxes of astrometric reference stars (Tables 6.15 and 6.16).

The new set of parameters for HD 33636 has been used to complement the analysis of interferometric data. For the interferometry experiment we conclude that our

instrumental set up was not adequate to validate the binary parameters obtained from RV and astrometry analysis, however we have detected visibility variations that can not be explained by a symmetrical brightness distribution, like a disk or point-like individual source. Although we have not concluded that this signal comes from the companion, we estimated a flux ratio of the order of 30% for the observed variations. This is too high to be explained by the flux of the companion. We conclude that an ideal interferometer set-up to study HD 33636 would have a baseline of 330 m, which is not available presently neither in the VLTI nor in the Keck Interferometer.

The astrometric determination of the masses is definitive to establish the nature of low mass companions. It can decisively characterize a companion as a planet. A good illustration of this can be seen from the results for three objects that were previously listed as exoplanet candidates: Gliese 876 b, HD 136118 b and HD 33636 b. Each object has been found to belong to a different class: a giant planet, a brown dwarf and an M-dwarf star, respectively, Benedict et al. (2002), Martioli et al. (2010) (and this work), and Bean et al. (2007) (and this work). These results demonstrate the importance of the application of complementary techniques in observing extrasolar planetary systems.

The *HST* observing time is precious and therefore scarce. There are prospective projects under development, like the Space Interferometric Mission (SIM) (`http://sim.jpl.nasa.gov`) and PRIMA (VAN BELLE et al., 2008), that aim to follow-up nearby targets astrometrically with μarcsec precision. The analysis of these data will certainly make use of similar methods as those presented in this thesis. Therefore we conclude that this work is not only important for the analysis of FGS/HST data, but rather it is an experiment that provides important background for future involvement in worldwide astrometric missions that aim the detection and characterization of low-mass star, brown dwarfs and exoplanets companions.

Infrared interferometry is a promising technique for following up high contrast binaries with low mass companions. Although we were not able to determine the binary parameters for HD 33636, interferometry potentially allows one to determine the position angle and separation of binaries. This presents as a cheaper and faster alternative over long term space astrometry. In ideal cases, interferometry allows one to obtain the companion's spectrum. This feature turns interferometry of utmost importance, since it complements the other two methods with luminous information

from the low mass objects in study.

We finally conclude by saying that these techniques, when combined, may lead to the determination of accurate masses, orbits and spectra of exoplanets, brown dwarfs and low-mass star companions. These objects comprise the most informative material from the bottom of the H-R diagram. Consequently, the implementation of these techniques, using state-of-the-art instrumentation, will soon provide us with a better understanding on the nature of these bodies and consequently a construction of better evolutionary models for the star-planet transition range. Moreover, these techniques may be improved and hence employed extensively in the characterization of Neptunes, Super-Earths and Earth-like exoplanets. The Neptune-like exoplanets are known to be more abundant than those with the size of Jupiter (SUMI et al., 2010). Therefore, less massive planets tend to be even more abundant, which makes us believe that in the near future these techniques will be part of astronomers' quotidian for the exploration of extrasolar planetary systems. Ultimately, this may soon lead to unearthing planetary formation processes, or to the first detection of an exoplanetary biological activity.

REFERENCES

ADAMS, F. C.; LAUGHLIN, G. Relativistic effects in extrasolar planetary systems. **International Journal of Modern Physics D**, v. 15, p. 2133–2140, 2006. 16

ARSENAULT, R.; DONALDSON, R.; DUPUY, C.; FEDRIGO, E.; HUBIN, N. N.; IVANESCU, L.; KASPER, M. E.; OBERTI, S.; PAUFIQUE, J.; ROSSI, S.; SILBER, A.; DELABRE, B.; LIZON, J.-L.; GIGAN, P. MACAO-VLTI adaptive optics systems performance. **Proceedings- SPIE the International Society for Optical Engineering**, v. 5490, p. 47–58, 2004. 43

BARAFFE, I.; CHABRIER, G.; ALLARD, F.; HAUSCHILDT, P. H. Evolutionary models for solar metallicity low-mass stars: mass-magnitude relationships and color-magnitude diagrams. **Astronomy and Astrophysics**, v. 337, p. 403–412, September 1998. xviii, 137, 140, 141, 142

_____. Evolutionary models for low-mass stars and brown dwarfs: Uncertainties and limits at very young ages. **Astronomy and Astrophysics**, v. 382, p. 563–572, February 2002. 137, 142

BARANNE, A.; QUELOZ, D.; MAYOR, M.; ADRIANZYK, G.; KNISPEL, G.; KOHLER, D.; LACROIX, D.; MEUNIER, J.-P.; RIMBAUD, G.; VIN, A. ELODIE: A spectrograph for accurate radial velocity measurements. **Astronomy and Astrophysics Supplement**, v. 119, p. 373–390, October 1996. 5

BEAN, J. L.; MCARTHUR, B. E.; BENEDICT, G. F.; HARRISON, T. E.; BIZYAEV, D.; NELAN, E.; SMITH, V. V. The mass of the candidate exoplanet companion to HD 33636 from Hubble Space Telescope astrometry and high-precision radial velocities. **The Astronomical Journal**, v. 134, p. 749–758, August 2007. 3, 7, 10, 50, 92, 93, 94, 139, 146

BEICHMAN, C. A.; BRYDEN, G.; RIEKE, G. H.; STANSBERRY, J. A.; TRILLING, D. E.; STAPELFELDT, K. R.; WERNER, M. W.; ENGELBRACHT, C. W.; BLAYLOCK, M.; GORDON, K. D.; CHEN, C. H.; SU, K. Y. L.; HINES, D. C. Planets and infrared excesses: Preliminary results from a Spitzer MIPS survey of solar-type stars. **Astrophysical Journal**, v. 622, p. 1160–1170, April 2005. 140

BENEDICT, G. F.; MCARTHUR, B.; CHAPPELL, D. W.; NELAN, E.; JEFFERYS, W. H.; ALTENA, W. van; LEE, J.; CORNELL, D.; SHELUS, P. J.; HEMENWAY, P. D.; FRANZ, O. G.; WASSERMAN, L. H.; DUNCOMBE, R. L.; STORY, D.; WHIPPLE, A. L.; FREDRICK, L. W. Interferometric astrometry of Proxima Centauri and Barnard's star using Hubble Space Telescope Fine Guidance Sensor 3: Detection limits for substellar companions. **The Astronomical Journal**, v. 118, p. 1086–1100, August 1999. 1

BENEDICT, G. F.; MCARTHUR, B.; NELAN, E.; STORY, D.; WHIPPLE, A. L.; SHELUS, P. J.; JEFFERYS, W. H.; HEMENWAY, P. D.; FRANZ, O. G.; WASSERMAN, L. H.; DUNCOMBE, R. L.; ALTENA, W. van; FREDRICK, L. W. Photometry of Proxima Centauri and Barnard's star using Hubble Space Telescope Fine Guidance Sensor 3: A search for periodic variations. **The Astronomical Journal**, v. 116, p. 429–439, July 1998. 135

BENEDICT, G. F.; MCARTHUR, B. E.; BEAN, J. L.; BARNES, R.; HARRISON, T. E.; HATZES, A.; MARTIOLI, E.; NELAN, E. P. The mass of HD 38529 c from Hubble Space Telescope astrometry and high-precision radial velocities. **The Astronomical Journal**, v. 139, p. 1844–1856, May 2010. 6, 137

BENEDICT, G. F.; MCARTHUR, B. E.; FORVEILLE, T.; DELFOSSE, X.; NELAN, E.; BUTLER, R. P.; SPIESMAN, W.; MARCY, G.; GOLDMAN, B.; PERRIER, C.; JEFFERYS, W. H.; MAYOR, M. A mass for the extrasolar planet Gliese 876 b determined from Hubble Space Telescope Fine Guidance Sensor 3 astrometry and high-precision radial velocities. **Astrophysical Journal Letters**, v. 581, n. 2, p. L115–L118, December 2002. 3, 6, 146

BERGER, J. P.; SEGRANSAN, D. An introduction to visibility modeling. **New Astronomy Review**, v. 51, p. 576–582, October 2007. 25

BODEN, A. F. Calibrating optical/IR interferometry visibility data. **New Astronomy Review**, v. 51, p. 617–622, October 2007. 81

BONNEAU, D.; CLAUSSE, J.-M.; DELFOSSE, X.; MOURARD, D.; CETRE, S.; CHELLI, A.; CRUZALÈBES, P.; DUVERT, G.; ZINS, G. SearchCal: a virtual observatory tool for searching calibrators in optical long baseline interferometry. I. The bright object case. **Astronomy and Astrophysics**, v. 456, p. 789–789, September 2006. 80

BUTLER, R. P.; MARCY, G. W.; WILLIAMS, E.; MCCARTHY, C.; DOSANJH, P.; VOGT, S. S. Attaining doppler precision of 3 m s-1. **The Publications of the Astronomical Society of the Pacific**, v. 108, p. 500–+, June 1996. 5, 31, 50, 63, 64

BUTLER, R. P.; WRIGHT, J. T.; MARCY, G. W.; FISCHER, D. A.; VOGT, S. S.; TINNEY, C. G.; JONES, H. R. A.; CARTER, B. D.; JOHNSON, J. A.; MCCARTHY, C.; PENNY, A. J. Catalog of nearby exoplanets. **Astrophysical Journal**, v. 646, p. 505–522, July 2006. 7, 9, 10, 92, 135

CAMPBELL, B.; WALKER, G. A. H. Precision radial velocities with an absorption cell. **The Publications of the Astronomical Society of the Pacific**, v. 91, p. 540–545, August 1979. 63

CAMPBELL, B.; WALKER, G. A. H.; YANG, S. A search for substellar companions to solar-type stars. **Astrophysical Journal**, v. 331, p. 902–921, August 1988. 63

CHABRIER, G.; BARAFFE, I.; ALLARD, F.; HAUSCHILDT, P. Evolutionary models for very low-mass stars and brown dwarfs with dusty atmospheres. **Astrophysical Journal**, v. 542, p. 464–472, October 2000. 127, 137

CHAMBERS, J. E. A hybrid symplectic integrator that permits close encounters between massive bodies. **Monthly Notices of the Royal Astronomical Society**, v. 304, p. 793–799, April 1999. 16, 139

CHARBONNEAU, D.; BROWN, T. M.; NOYES, R. W.; GILLILAND, R. L. Detection of an extrasolar planet atmosphere. **Astrophysical Journal**, v. 568, p. 377–384, March 2002. 3

CHELLI, A.; DUVERT, G.; MALBET, F.; KERN, P. Phase closure nulling. Application to the spectroscopy of faint companions. **Astronomy and Astrophysics**, v. 498, p. 321–327, April 2009. 7, 143

CORCIONE, L.; BAUVIER, B.; BONINO, D.; GAI, M.; GARDIOL, D.; GENNAI, A.; LATTANZI, M. G.; LOREGGIA, D.; MASSONE, G.; MÉNARDI, S. FINITO: Fringe tracking Instrument of NIce and Torino for VLTI. In: GENIE - DARWIN WORKSHOP - HUNTING FOR PLANETS, 2002, Leiden, The Netherlands. **Proceedings...** Noordwijk, The Netherlands: ESA Publications Division, 2003. (ESA SP, v. 522). 45

CUTRI, R. M.; SKRUTSKIE, M. F.; DYK, S. van; BEICHMAN, C. A.;
CARPENTER, J. M.; CHESTER, T.; CAMBRESY, L.; EVANS, T.; FOWLER,
J.; GIZIS, J.; HOWARD, E.; HUCHRA, J.; JARRETT, T.; KOPAN, E. L.;
KIRKPATRICK, J. D.; LIGHT, R. M.; MARSH, K. A.; MCCALLON, H.;
SCHNEIDER, S.; STIENING, R.; SYKES, M.; WEINBERG, M.; WHEATON,
W. A.; WHEELOCK, S.; ZACARIAS, N. **2MASS All Sky Catalog of point
sources**. June 2003. Disponível em:
<http://irsa.ipac.caltech.edu/applications/Gator/>. 9, 10

DELFOSSE, X.; TINNEY, C. G.; FORVEILLE, T.; EPCHTEIN, N.;
BORSENBERGER, J.; FOUQUÉ, P.; KIMESWENGER, S.; TIPHÈNE, D.
Searching for very low-mass stars and brown dwarfs with DENIS. **Astronomy
and Astrophysics Supplement**, v. 135, p. 41–56, February 1999. 137

DUVERT, G.; CHELLI, A.; MALBET, F.; KERN, P. Phase closure nulling of HD
59717 with AMBER/VLTI . Detection of the close faint companion. **Astronomy
and Astrophysics**, v. 509, p. A66+, January 2010. 7, 142

DUVERT, G.; ZINS, G.; MALBET, F.; MILLOUR, F.; LEBOUQUIN, J.-B.;
ALTARIBA, E.; ACKE, B.; TATULLI, E. amdlib. **Astrophysics Software
Database**, p. 35–+, January 2008. 78

ENDL, M.; KÜRSTER, M.; ELS, S. The planet search program at the ESO Coudé
Echelle spectrometer. I. Data modeling technique and radial velocity precision
tests. **Astronomy and Astrophysics**, v. 362, p. 585–594, October 2000. 66

FISCHER, D. A.; MARCY, G. W.; BUTLER, R. P.; VOGT, S. S.; WALP, B.;
APPS, K. Planetary companions to HD 136118, HD 50554, and HD 106252. **The
Publications of the Astronomical Society of the Pacific**, v. 114, p. 529–535,
May 2002. 3, 9, 31, 35, 92, 93, 95, 135

FISCHER, D. A.; VALENTI, J. The planet-metallicity correlation.
Astrophysical Journal, v. 622, p. 1102–1117, April 2005. 10

GAI, M.; MENARDI, S.; CESARE, S.; BAUVIR, B.; BONINO, D.; CORCIONE,
L.; DIMMLER, M.; MASSONE, G.; REYNAUD, F.; WALLANDER, A. The VLTI
fringe sensors: FINITO and PRIMA FSU. **Proceedings- SPIE the
International Society for Optical Engineering**, v. 5491, p. 528–539, 2004. 45

GONZALEZ, G.; LAWS, C. Parent stars of extrasolar planets - VIII. Chemical abundances for 18 elements in 31 stars. **Monthly Notices of the Royal Astronomical Society**, v. 378, p. 1141–1152, July 2007. 8, 9

GREGORY, P. C. A Bayesian periodogram finds evidence for three planets in HD 11964. **Monthly Notices of the Royal Astronomical Society**, v. 381, p. 1607–1616, November 2007. 98

GRETHER, D.; LINEWEAVER, C. H. How dry is the brown dwarf desert? Quantifying the relative number of planets, brown dwarfs, and stellar companions around nearby Sun-like stars. **Astrophysical Journal**, v. 640, p. 1051–1062, April 2006. 136

HANIFF, C. An introduction to the theory of interferometry. **New Astronomy Review**, v. 51, p. 565–575, October 2007. 22, 23

_____. Ground-based optical interferometry: A practical primer. **New Astronomy Review**, v. 51, p. 583–596, October 2007. 22

HENRY, G. W.; MARCY, G. W.; BUTLER, R. P.; VOGT, S. S. A transiting "51 Peg-like" planet. **Astrophysical Journal**, v. 529, p. L41–L44, January 2000. 2

HOLLAND, P. W.; WELSCH, R. E. Robust estimation using iteratively reweighted least squares. **Communications in Statistics - Theory and Methods**, A6, n. 9, p. 813, 1977. 91

HUBER, P. J. **Robust Statistics**. New York: John Wiley and Sons, 1981. 91

JACOB, W. S. On certain anomalies presented by the binary star 70 Ophiuchi. **Monthly Notices of the Royal Astronomical Society**, v. 15, p. 228–+, June 1855. 1

JEFFERYS, W.; WHIPPLE, A.; WANG, Q.; MCARTHUR, B.; BENEDICT, G. F.; NELAN, E.; STORY, D.; ABRAMOWICZ-REED, L. Optical field angle distortion calibration of FGS3. In: CALIBRATING HUBBLE SPACE TELESCOPE, 1., 1993, Baltimore, MD USA. **Proceedings...** Baltimore: STScI, 1994. p. 353–+. 74

JEFFERYS, W. H.; FITZPATRICK, M. J.; MCARTHUR, B. E. GaussFit - a system for least squares and robust estimation. **Celestial Mechanics**, v. 41, p. 39–+, 1988. 72, 91

KAMP, P. van de. **Principles of Astrometry**. San Francisco and London: W. H. Freeman and Company, 1967. 17, 20

_____. Parallax, proper motion, acceleration, and orbital motion of Barnard's star. **The Astronomical Journal**, v. 74, p. 238–+, March 1969. 1

LOVIS, C.; PEPE, F. A new list of thorium and argon spectral lines in the visible. **Astronomy and Astrophysics**, v. 468, p. 1115–1121, June 2007. 62, 63

MARTIOLI, E.; MCARTHUR, B. E.; BENEDICT, G. F.; BEAN, J. L.; HARRISON, T. E.; ARMSTRONG, A. The mass of the candidate exoplanet companion to HD 136118 from Hubble Space Telescope astrometry and high-precision radial velocities. **Astrophysical Journal**, v. 708, p. 625–634, January 2010. 9, 92, 146

MAYOR, M.; QUELOZ, D. A Jupiter-mass companion to a solar-type star. **Nature**, v. 378, p. 355–359, November 1995. 1

MCARTHUR, B.; BENEDICT, G. F.; JEFFERYS, W. H. The optical field angle distortion calibration of HST Fine Guidance Sensors 1R and 3. In: THE 2005 HST CALIBRATION WORKSHOP, 2005, Baltimore, MD USA. **Proceedings...** Baltimore: STScI, 2005. p. 396–+. 74

MCARTHUR, B.; BENEDICT, G. F.; JEFFERYS, W. H.; NELAN, E. Maintaining the FGS3 optical field angle distortion calibration. In: THE 1997 HST CALIBRATION WORKSHOP, 1997, Baltimore, MD USA. **Proceedings...** Baltimore: STScI, 1997. p. 472–+. 74

_____. The optical field angle distortion calibration of HST Fine Guidance Sensors 1R and 3. In: THE 2002 HST CALIBRATION WORKSHOP : HUBBLE AFTER THE INSTALLATION OF THE ACS AND THE NICMOS COOLING SYSTEM, 2002, Baltimore, MD USA. **Proceedings...** Baltimore: STScI, 2002. p. 373–+. 74

MCARTHUR, B. E.; BENEDICT, G. F.; BARNES, R.; MARTIOLI, E.; KORZENNIK, S.; NELAN, E.; BUTLER, R. P. New observational constraints on the Upsilon Andromedae system with data from the Hubble Space Telescope and Hobby-Eberly Telescope. **Astrophysical Journal**, v. 715, p. 1203–1220, June 2010. 6

MCARTHUR, B. E.; ENDL, M.; COCHRAN, W. D.; BENEDICT, G. F.; FISCHER, D. A.; MARCY, G. W.; BUTLER, R. P.; NAEF, D.; MAYOR, M.; QUELOZ, D.; UDRY, S.; HARRISON, T. E. Detection of a Neptune-mass planet in the ρ Cancri system using the Hobby-Eberly Telescope. **Astrophysical Journal Letters**, v. 614, p. L81–L84, October 2004. 6

MÉRAND, A.; BORDÉ, P.; FORESTO, V. C. A catalog of bright calibrator stars for 200-m baseline near-infrared stellar interferometry. **Astronomy and Astrophysics**, v. 433, n. 3, p. 1155–1162, April 2005. 80

MERAND, A.; DUMAS, C.; KAUFER, A. **Very Large Telescope Paranal science operations AMBER user manual**. Garching bei Munchen, Germany, 2010. Disponível em: <http://www.eso.org/sci/facilities/paranal/instruments/amber/doc/>. 43

NELAN, E.; MAKIDON, R. B.; YOUNGER, J.; LUPIE, O. L.; HOLFELTZ, S. T.; TAFF, L. G.; LATTANZI, M. G.; FRESNEAU, A. **Fine Guidance Sensor instrument handbook**. Baltimore, STScI, 2010. Disponível em: <http://www.stsci.edu/hst/fgs/documents/instrumenthandbook>. 37, 38, 39, 40, 72, 135

NORDSTROM, B.; MAYOR, M.; ANDERSEN, J.; HOLMBERG, J.; PONT, F.; JORGENSEN, B. R.; OLSEN, E. H.; UDRY, S.; MOWLAVI, N. The Geneva-Copenhagen survey of the solar neighbourhood. Ages, metallicities, and kinematic properties of ∼14 000 F and G dwarfs. **Astronomy and Astrophysics**, v. 418, p. 989–1019, May 2004. 10

PAULS, T. A.; YOUNG, J. S.; COTTON, W. D.; MONNIER, J. D. A data exchange standard for optical (visible/IR) interferometry. **The Publications of the Astronomical Society of the Pacific**, v. 117, p. 1255–1262, November 2005. 79

PERRIER, C.; SIVAN, J.-P.; NAEF, D.; BEUZIT, J. L.; MAYOR, M.; QUELOZ, D.; UDRY, S. The ELODIE survey for northern extra-solar planets. I. Six new extra-solar planet candidates. **Astronomy and Astrophysics**, v. 410, p. 1039–1049, November 2003. 7, 92

PERRYMAN, M. A. C.; LINDEGREN, L.; KOVALEVSKY, J.; HOEG, E.; BASTIAN, U.; BERNACCA, P. L.; CRÉZÉ, M.; DONATI, F.; GRENON, M.;

155

LEEUWEN, F. van; MAREL, H. van der; MIGNARD, F.; MURRAY, C. A.; POOLE, R. S. L.; SCHRIJVER, H.; TURON, C.; ARENOU, F.; FROESCHLÉ, M.; PETERSEN, C. S. The HIPPARCOS catalogue. **Astronomy and Astrophysics**, v. 323, p. L49–L52, July 1997. xix, 9, 113, 116, 117, 118

PETROV, R. G.; MALBET, F.; WEIGELT, G.; ANTONELLI, P.; BECKMANN, U.; BRESSON, Y.; CHELLI, A.; DUGUÉ, M.; DUVERT, G.; GENNARI, S.; GLÜCK, L.; KERN, P.; LAGARDE, S.; COARER, E. L.; LISI, F.; MILLOUR, F.; PERRAUT, K.; PUGET, P.; RANTAKYRÖ, F.; ROBBE-DUBOIS, S.; ROUSSEL, A.; SALINARI, P.; TATULLI, E.; ZINS, G.; ACCARDO, M.; ACKE, B.; AGABI, K.; ALTARIBA, E.; AREZKI, B.; ARISTIDI, E.; BAFFA, C.; BEHREND, J.; BLÖCKER, T.; BONHOMME, S.; BUSONI, S.; CASSAING, F.; CLAUSSE, J.-M.; COLIN, J.; CONNOT, C.; DELBOULBÉ, A.; SOUZA, A. Domiciano de; DRIEBE, T.; FEAUTRIER, P.; FERRUZZI, D.; FORVEILLE, T.; FOSSAT, E.; FOY, R.; FRAIX-BURNET, D.; GALLARDO, A.; GIANI, E.; GIL, C.; GLENTZLIN, A.; HEIDEN, M.; HEININGER, M.; UTRERA, O. H.; HOFMANN, K.-H.; KAMM, D.; KIEKEBUSCH, M.; KRAUS, S.; CONTEL, D. L.; CONTEL, J.-M. L.; LESOURD, T.; LOPEZ, B.; LOPEZ, M.; MAGNARD, Y.; MARCONI, A.; MARS, G.; MARTINOT-LAGARDE, G.; MATHIAS, P.; MÈGE, P.; MONIN, J.-L.; MOUILLET, D.; MOURARD, D.; NUSSBAUM, E.; OHNAKA, K.; PACHECO, J.; PERRIER, C.; RABBIA, Y.; REBATTU, S.; REYNAUD, F.; RICHICHI, A.; ROBINI, A.; SACCHETTINI, M.; SCHERTL, D.; SCHÖLLER, M.; SOLSCHEID, W.; SPANG, A.; STEE, P.; STEFANINI, P.; TALLON, M.; TALLON-BOSC, I.; TASSO, D.; TESTI, L.; VAKILI, F.; LÜHE, O. von der; VALTIER, J.-C.; VANNIER, M.; VENTURA, N. AMBER, the near-infrared spectro-interferometric three-telescope VLTI instrument. **Astronomy and Astrophysics**, v. 464, p. 1–12, March 2007. 43

PISKUNOV, N. E.; VALENTI, J. A. New algorithms for reducing cross-dispersed echelle spectra. **Astronomy and Astrophysics**, v. 385, p. 1095–1106, April 2002. 50

POURBAIX, D.; JORISSEN, A. Re-processing the Hipparcos transit data and intermediate astrometric data of spectroscopic binaries. I. Ba, CH and Tc-poor S stars. **Astronomy and Astrophysics Supplement**, v. 145, p. 161–183, July 2000. 113

PRIETO, C. A.; LAMBERT, D. L. Fundamental parameters of nearby stars from the comparison with evolutionary calculations: masses, radii and effective temperatures. **Astronomy and Astrophysics**, v. 352, p. 555–562, December 1999. 9, 10, 135

REDFIELD, S.; ENDL, M.; COCHRAN, W. D.; KOESTERKE, L. Sodium absorption from the exoplanetary atmosphere of HD 189733b detected in the optical transmission spectrum. **Astrophysical Journal Letters**, v. 673, p. L87–L90, January 2008. 3

REFFERT, S.; QUIRRENBACH, A. Hipparcos astrometric orbits for two brown dwarf companions: HD 38529 and HD 168443. **Astronomy and Astrophysics**, v. 449, p. 699–702, April 2006. 136

REY, W. J. J. **Introduction to Robust and Quasi-Robust Methods**. New York: Springer-Verlag, 1983. 91

RICHARDSON, L. J.; DEMING, D.; HORNING, K.; SEAGER, S.; HARRINGTON, J. A spectrum of an extrasolar planet. **Nature**, v. 445, p. 892–895, February 2007. 3

ROBBE-DUBOIS, S.; LAGARDE, S.; PETROV, R. G.; LISI, F.; BECKMANN, U.; ANTONELLI, P.; BRESSON, Y.; MARTINOT-LAGARDE, G.; ROUSSEL, A.; SALINARI, P.; VANNIER, M.; CHELLI, A.; DUGUÉ, M.; DUVERT, G.; GENNARI, S.; GLÜCK, L.; KERN, P.; COARER, E. L.; MALBET, F.; MILLOUR, F.; PERRAUT, K.; PUGET, P.; RANTAKYRÖ, F.; TATULLI, E.; WEIGELT, G.; ZINS, G.; ACCARDO, M.; ACKE, B.; AGABI, K.; ALTARIBA, E.; AREZKI, B.; ARISTIDI, E.; BAFFA, C.; BEHREND, J.; BLÖCKER, T.; BONHOMME, S.; BUSONI, S.; CASSAING, F.; CLAUSSE, J.-M.; COLIN, J.; CONNOT, C.; DELAGE, L.; DELBOULBÉ, A.; SOUZA, A. Domiciano de; DRIEBE, T.; FEAUTRIER, P.; FERRUZZI, D.; FORVEILLE, T.; FOSSAT, E.; FOY, R.; FRAIX-BURNET, D.; GALLARDO, A.; GIANI, E.; GIL, C.; GLENTZLIN, A.; HEIDEN, M.; HEININGER, M.; UTRERA, O. H.; HOFMANN, K.-H.; KAMM, D.; KIEKEBUSCH, M.; KRAUS, S.; CONTEL, D. L.; CONTEL, J.-M. L.; LESOURD, T.; LOPEZ, B.; LOPEZ, M.; MAGNARD, Y.; MARCONI, A.; MARS, G.; MATHIAS, P.; MÈGE, P.; MONIN, J.-L.; MOUILLET, D.; MOURARD, D.; NUSSBAUM, E.; OHNAKA, K.; PACHECO, J.; PERRIER, C.; RABBIA, Y.; REBATTU, S.; REYNAUD, F.; RICHICHI, A.; ROBINI, A.;

SACCHETTINI, M.; SCHERTL, D.; SCHÖLLER, M.; SOLSCHEID, W.; SPANG, A.; STEE, P.; STEFANINI, P.; TALLON, M.; TALLON-BOSC, I.; TASSO, D.; TESTI, L.; VAKILI, F.; LÜHE, O. von der; VALTIER, J.-C.; VENTURA, N. Optical configuration and analysis of the AMBER/VLTI instrument. **Astronomy and Astrophysics**, v. 464, p. 13–27, March 2007. 43

SAAR, S. H.; DONAHUE, R. A. Activity-related radial velocity variation in cool stars. **Astrophysical Journal**, v. 485, p. 319–+, August 1997. xviii, 135, 136

SAFFE, C.; GÓMEZ, M.; CHAVERO, C. On the ages of exoplanet host stars. **Astronomy and Astrophysics**, v. 443, p. 609–626, November 2005. 9

SALAMI, H.; ROSS, A. J. A molecular iodine atlas in ascii format. **Journal of Molecular Spectroscopy**, v. 233, p. 157–159, 2005. 64, 65

SCARGLE, J. D. Studies in astronomical time series analysis. II - Statistical aspects of spectral analysis of unevenly spaced data. **Astrophysical Journal**, v. 263, p. 835–853, December 1982. 95

SHAW, B.; QUIJANO, J. K.; KAISER, M. E. **HST data handbook**. Baltimore, STScI, 2009. Disponível em: <http://www.stsci.edu/hst/HST_overview/documents/datahandbook/>. 71, 72

STANDISH JR., E. M. **JPL planetary and lunar ephemerides, DE405/LE405**. Pasadena, California, August 1998. Disponível em: <http://iau-comm4.jpl.nasa.gov/relateds.html>. 18

SUMI, T.; BENNETT, D. P.; BOND, I. A.; UDALSKI, A.; BATISTA, V.; DOMINIK, M.; FOUQUÉ, P.; KUBAS, D.; GOULD, A.; MACINTOSH, B.; COOK, K.; DONG, S.; SKULJAN, L.; CASSAN, A.; ABE, F.; BOTZLER, C. S.; FUKUI, A.; FURUSAWA, K.; HEARNSHAW, J. B.; ITOW, Y.; KAMIYA, K.; KILMARTIN, P. M.; KORPELA, A.; LIN, W.; LING, C. H.; MASUDA, K.; MATSUBARA, Y.; MIYAKE, N.; MURAKI, Y.; NAGAYA, M.; NAGAYAMA, T.; OHNISHI, K.; OKUMURA, T.; PERROTT, Y. C.; RATTENBURY, N.; SAITO, T.; SAKO, T.; SULLIVAN, D. J.; SWEATMAN, W. L.; TRISTRAM, P. J.; YOCK, P. C. M.; COLLABORATION, T. M.; BEAULIEU, J. P.; COLE, A.; COUTURES, C.; DURAN, M. F.; GREENHILL, J.; JABLONSKI, F.; MARBOEUF, U.; MARTIOLI, E.; PEDRETTI, E.; PEJCHA, O.; ROJO, P.;

ALBROW, M. D.; BRILLANT, S.; BODE, M.; BRAMICH, D. M.; BURGDORF, M. J.; CALDWELL, J. A. R.; CALITZ, H.; CORRALES, E.; DIETERS, S.; PRESTER, D. D.; DONATOWICZ, J.; HILL, K.; HOFFMAN, M.; HORNE, K.; JØRGENSEN, U. G.; KAINS, N.; KANE, S.; MARQUETTE, J. B.; MARTIN, R.; MEINTJES, P.; MENZIES, J.; POLLARD, K. R.; SAHU, K. C.; SNODGRASS, C.; STEELE, I.; STREET, R.; TSAPRAS, Y.; WAMBSGANSS, J.; WILLIAMS, A.; ZUB, M.; COLLABORATION, T. P.; SZYMAŃSKI, M. K.; KUBIAK, M.; PIETRZYŃSKI, G.; SOSZYŃSKI, I.; SZEWCZYK, O.; WYRZYKOWSKI, Ł.; ULACZYK, K.; COLLABORATION, T. O.; ALLEN, W.; CHRISTIE, G. W.; DEPOY, D. L.; GAUDI, B. S.; HAN, C.; JANCZAK, J.; LEE, C.-U.; MCCORMICK, J.; MALLIA, F.; MONARD, B.; NATUSCH, T.; PARK, B.-G.; POGGE, R. W.; SANTALLO, R. A cold neptune-mass planet OGLE-2007-BLG-368Lb: cold neptunes are common. **Astrophysical Journal**, v. 710, p. 1641–1653, February 2010. 147

TAKEDA, G.; FORD, E. B.; SILLS, A.; RASIO, F. A.; FISCHER, D. A.; VALENTI, J. A. Structure and evolution of nearby stars with planets. II. Physical properties of ~1000 cool stars from the SPOCS catalog. **The Astrophysical Journal Supplement Series**, v. 168, p. 297–318, February 2007. 10, 93

TATULLI, E.; MILLOUR, F.; CHELLI, A.; DUVERT, G.; ACKE, B.; UTRERA, O. H.; HOFMANN, K.-H.; KRAUS, S.; MALBET, F.; MÈGE, P.; PETROV, R. G.; VANNIER, M.; ZINS, G.; ANTONELLI, P.; BECKMANN, U.; BRESSON, Y.; DUGUÉ, M.; GENNARI, S.; GLÜCK, L.; KERN, P.; LAGARDE, S.; COARER, E. L.; LISI, F.; PERRAUT, K.; PUGET, P.; RANTAKYRÖ, F.; ROBBE-DUBOIS, S.; ROUSSEL, A.; WEIGELT, G.; ACCARDO, M.; AGABI, K.; ALTARIBA, E.; AREZKI, B.; ARISTIDI, E.; BAFFA, C.; BEHREND, J.; BLÖCKER, T.; BONHOMME, S.; BUSONI, S.; CASSAING, F.; CLAUSSE, J.-M.; COLIN, J.; CONNOT, C.; DELBOULBÉ, A.; SOUZA, A. Domiciano de; DRIEBE, T.; FEAUTRIER, P.; FERRUZZI, D.; FORVEILLE, T.; FOSSAT, E.; FOY, R.; FRAIX-BURNET, D.; GALLARDO, A.; GIANI, E.; GIL, C.; GLENTZLIN, A.; HEIDEN, M.; HEININGER, M.; KAMM, D.; KIEKEBUSCH, M.; CONTEL, D. L.; CONTEL, J.-M. L.; LESOURD, T.; LOPEZ, B.; LOPEZ, M.; MAGNARD, Y.; MARCONI, A.; MARS, G.; MARTINOT-LAGARDE, G.; MATHIAS, P.; MONIN, J.-L.; MOUILLET, D.; MOURARD, D.; NUSSBAUM, E.; OHNAKA, K.; PACHECO, J.; PERRIER, C.; RABBIA, Y.; REBATTU, S.; REYNAUD, F.; RICHICHI, A.; ROBINI, A.; SACCHETTINI, M.; SCHERTL, D.;

SCHÖLLER, M.; SOLSCHEID, W.; SPANG, A.; STEE, P.; STEFANINI, P.; TALLON, M.; TALLON-BOSC, I.; TASSO, D.; TESTI, L.; VAKILI, F.; LÜHE, O. von der; VALTIER, J.-C.; VENTURA, N. Interferometric data reduction with AMBER/VLTI. Principle, estimators, and illustration. **Astronomy and Astrophysics**, v. 464, p. 29–42, March 2007. 43, 44, 45, 77, 79

TULL, R. G. High-resolution fiber-coupled spectrograph of the Hobby-Eberly Telescope. **Proceedings- SPIE the International Society for Optical Engineering**, v. 3355, p. 387–398, 1998. 32, 33, 34

VALENTI, J. A.; BUTLER, R. P.; MARCY, G. W. Determining spectrometer instrumental profiles using FTS reference spectra. **The Publications of the Astronomical Society of the Pacific**, v. 107, p. 966–+, October 1995. 50, 66, 67

VAN BELLE, G. T.; SAHLMANN, J.; ABUTER, R.; ACCARDO, M.; ANDOLFATO, L.; BRILLANT, S.; JONG, J. de; DERIE, F.; DELPLANCKE, F.; DUC, T. P.; DUPUY, C.; GILLI, B.; GITTON, P.; HAGUENAUER, P.; JOCOU, L.; JOST, A.; LIETO, N. di; FRAHM, R.; MÉNARDI, S.; MOREL, S.; MORESMAU, J.-M.; PALSA, R.; POPOVIC, D.; POZNA, E.; PUECH, F.; LÉVÊQUE, S.; RAMIREZ, A.; SCHUHLER, N.; SOMBOLI, F.; WEHNER, S.; CONSORTIUM, T. E. The VLTI PRIMA facility. **The Messenger**, v. 134, p. 6–11, December 2008. 146

VAN LEEUWEN, F. Validation of the new Hipparcos reduction. **Astronomy and Astrophysics**, v. 474, p. 653–664, November 2007. xix, 116, 117, 118

VOGT, S. S.; BUTLER, R. P.; MARCY, G. W.; FISCHER, D. A.; POURBAIX, D.; APPS, K.; LAUGHLIN, G. Ten low-mass companions from the Keck precision velocity survey. **Astrophysical Journal**, v. 568, p. 352–362, March 2002. 7, 10

WHIPPLE, A. L.; MCARTHUR, B.; WANG, Q.; JEFFERYS, W. H.; BENEDICT, G. F.; LALICH, A. M.; HEMENWAY, P. D.; NELAND, E.; SHELUSS, P. J.; STORY, D. Astrometric precision and accuracy with HST FGS3 in the position mode. In: CALIBRATING HUBBLE SPACE TELESCOPE: POST-SERVICING MISSION, 1995, Baltimore, MD USA. **Proceedings...** Baltimore: STScI, 1995. p. 119–+. 74

WOLSZCZAN, A.; FRAIL, D. A. A planetary system around the millisecond pulsar PSR1257 + 12. **Nature**, v. 355, p. 145–147, January 1992. 1

ZACHARIAS, N.; FINCH, C.; GIRARD, T.; HAMBLY, N.; WYCOFF, G.; ZACHARIAS, M. I.; CASTILLO, D.; CORBIN, T.; DIVITTORIO, M.; DUTTA, S.; GAUME, R.; GAUSS, S.; GERMAIN, M.; HALL, D.; HARTKOPF, W.; HSU, D.; HOLDENRIED, E.; MAKAROV, V.; MARTINES, M.; MASON, B.; MONET, D.; RAFFERTY, T.; RHODES, A.; SIEMERS, T.; SMITH, D.; TILLEMAN, T.; URBAN, S.; WIEDER, G.; WINTER, L.; YOUNG, A. The third US Naval Observatory CCD Astrograph Catalog (UCAC3). **The Astronomical Journal**, v. 139, p. 2184–2199, June 2010. xix, 9, 10, 116, 117

ZACHARIAS, N.; MONET, D. G.; LEVINE, S. E.; URBAN, S. E.; GAUME, R.; WYCOFF, G. L. NOMAD catalog (Zacharias+ 2005). **VizieR Online Data Catalog**, v. 1297, p. 0–+, November 2005. xix, 10, 116

10 APPENDIX

This appendix provides the GaussFit model for the simultaneous analysis of RV and astrometry data.

10.1 Model for the Simultaneous Analysis of Astrometry and Radial Velocity HD 136118 Data

```
parameter P01;
parameter T01;
parameter ecc01;
parameter wrv01;
parameter K01;

parameter P02;
parameter T02;
parameter ecc02;
parameter wrv02;
parameter K02;

parameter a01;
parameter inc01;
parameter omg01;

parameter gamma01;
parameter gamma02;
parameter gamma03;

parameter xi[star], eta[star];
parameter mux[star], muy[star];
parameter par[star];
parameter a[set], b[set], d[set], e[set];
parameter f[set], c[set];

observation RV;
data jd_rv;

data obstime, P_alpha, P_delta, rollV3, pra, pdec;
observation X, Y;
```

```
observation muxabs, muyabs, Parabs;
data star,set,file;
variable u, v, i, pxt, pyt, tc, pix, piy, mx, my, R, OFF, DtoR;
variable obstime1 = 0;
variable par_asec, mux_spd, muy_spd;
variable lx, ly, xx, yy, ww, xi0, eta0, Rback;
variable llcx, llcy, xxfx, xxfy, BmV;
variable orbx,orby;
variable obs = 1, mu = 2, pis = 3;


variable sinE01, cosE01, ecos01, cosv01, sinv01;
variable param01, cosvw01, coswrv01, sinwrv01, mu01, wwrv01, E01;
variable sinE02, cosE02, ecos02, cosv02, sinv02
variable param02, cosvw02, coswrv02, sinwrv02, mu02, wwrv02, E02;
variable orbx01,orby01,x_orb01,y_orb01,rvatmcnstr01;


variable agamma;
variable DegToRad;
variable pi = 3.141592654;
variable vp;
variable vorb;
variable ct;
variable EE;



main(){
        DegToRad = pi/180.0;
        doconstraints();
        domoreconstraints();
        while(import())
        {
                if (file == obs)
                {
                        atmmodel();
                }
                else if (file == pis)
                {
                        pimodel();
```

```
                }
                else if (file == mu)
                {
                        mumod();
                }
                else {
                        rvmodel();
                }
        }
}


doconstraints() {
        exportconstraint(a[8]-1);
        exportconstraint(b[8]);
        exportconstraint(c[8]);
        exportconstraint(d[8]);
        exportconstraint(e[8]-1);
        exportconstraint(f[8]);
}


domoreconstraints() {
        rvatmcnstr01 = (a01*(1.49598e11)*sin(DegToRad*inc01)/par[3])  -
            ((P01*86400)*K01*sqrt(1 - ecc01*ecc01)/(2*pi));
        exportconstraint(rvatmcnstr01);
}


atmmodel(){
        if (obstime1 == 0)
                obstime1 = obstime;

        DtoR = 3.141592654/180;
        R = DtoR * (rollV3 - 90.0);
        tc = obstime - obstime1;
        par_asec = par*1e-3;
        mux_spd = mux*1e-3/365.25;
        muy_spd = muy*1e-3/365.25;

        pxt = P_alpha * cos(DtoR * pdec);
```

```
pyt = P_delta;

pix = (+pxt*cos(R) + pyt*sin(R)) * par_asec;
piy = (-pxt*sin(R) + pyt*cos(R)) * par_asec;

mx = (+mux_spd*cos(R) + muy_spd*sin(R));
my = (-mux_spd*sin(R) + muy_spd*cos(R));

if(star == 3)
{
  x_orb01 = orbitx(obstime, P01, T01, ecc01);
  y_orb01 = orbity(obstime, P01, T01, ecc01);

  orbx01 = a01*1e-3*(
   + orbfac_xi(x_orb01,y_orb01,inc01,wrv01,omg01)*cos(R)
   + orbfac_eta(x_orb01,y_orb01,inc01,wrv01,omg01)*sin(R));

   orby01 = a01*1e-3*(
   - orbfac_xi(x_orb01,y_orb01,inc01,wrv01,omg01)*sin(R)
   + orbfac_eta(x_orb01,y_orb01,inc01,wrv01,omg01)*cos(R));

  orbx = orbx01;
  orby = orby01;
} else {
  orbx = 0;
  orby = 0;
}

llcx = 0;
llcy = 0;



xxfx = 0;
xxfy = 0;


xx = X - tc*mx - pix - orbx + llcx - xxfx;
yy = Y - tc*my - piy - orby + llcy - xxfy;
```

```
        Rback = DtoR * (264.174900 - rollV3);


        lx = xx*cos(Rback) + yy*sin(Rback);
        ly = - xx*sin(Rback) + yy*cos(Rback);


        xi0 = a*lx + b*ly + c;
        eta0 = d*lx + e*ly + f;


        u = xi0 - xi;
        v = eta0 - eta;
        export2(u,v); /* Export equations of condition */
}


pimodel() /* model for ref star parallaxes */
{
        yy = Parabs - par;
        export (yy);         /*Export equations of condition*/
}


mumod()
{
                ww = muxabs - mux;
                yy = muyabs - muy;
                export2 (ww, yy);        /*Export equations of condition
                    */
}


rvmodel()
{
        ct = jd_rv;
        make_RVorbit();
        vp = RV - vorb;
        export(vp);
}


orbitx(time, period, T_0, ecce) {
        variable x0, EA,MA;
        MA = (2*pi/period)*(time-T_0);
```

```
        EA = kepler(ecce,MA);
        x0 = cos(EA) - ecce;
        return x0;
}


orbity(time, period, T_0, ecce) {
        variable y0, EA, MA;
        MA = (2*pi/period)*(time-T_0);
        EA = kepler(ecce,MA);
        y0 = sin(EA)*sqrt(1. - ecce*ecce);
        return y0;
}


orbfac_xi(x_orb, y_orb,i_deg, w_deg, o_deg) {
        variable orbfacx;
        variable i_rad, w_rad, o_rad;
        variable bb,aa,gg,ff;
        i_rad = DegToRad*i_deg;
        w_rad = DegToRad*w_deg;
        o_rad = DegToRad*o_deg;
        bb = + cos(w_rad)*sin(o_rad)
                + sin(w_rad)*cos(o_rad)*cos(i_rad);
        aa = + cos(w_rad)*cos(o_rad)
                - sin(w_rad)*sin(o_rad)*cos(i_rad);
        gg = - sin(w_rad)*sin(o_rad)
                + cos(w_rad)*cos(o_rad)*cos(i_rad);
        ff = - sin(w_rad)*cos(o_rad)
              - cos(w_rad)*sin(o_rad)*cos(i_rad);
        orbfacx = bb*x_orb + gg*y_orb;
        return orbfacx;
}


orbfac_eta(x_orb, y_orb,i_deg, w_deg, o_deg) {
        variable orbfacy;
        variable i_rad, w_rad, o_rad;
        variable bb,aa,gg,ff;
        i_rad = DegToRad*i_deg;
        w_rad = DegToRad*w_deg;
```

```
        o_rad = DegToRad*o_deg;
        bb = + cos(w_rad)*sin(o_rad)
                + sin(w_rad)*cos(o_rad)*cos(i_rad);
        aa = + cos(w_rad)*cos(o_rad)
                - sin(w_rad)*sin(o_rad)*cos(i_rad);
        gg = - sin(w_rad)*sin(o_rad)
                + cos(w_rad)*cos(o_rad)*cos(i_rad);
        ff = - sin(w_rad)*cos(o_rad)
              - cos(w_rad)*sin(o_rad)*cos(i_rad);
        orbfacy = aa*x_orb + ff*y_orb;
        return orbfacy;
}


make_RVorbit() {
                if (file == 04)
                        agamma = gamma01;
                if (file == 05)
                        agamma = gamma02;
                if (file == 06)
                        agamma = gamma03;


        mu01 = 2*pi/P01;
        wwrv01 = wrv01*DegToRad;
        coswrv01 = cos(wwrv01);
        sinwrv01 = sin(wwrv01);
        param01 =  sqrt(1-ecc01*ecc01);

        kepler(ecc01,mu01*(ct-T01));
        E01 = EE;

                sinE01 = sin(E01);
                cosE01 = cos(E01);
                ecos01 = 1 - ecc01 * cosE01;
                cosv01 = (cosE01 - ecc01)/ecos01;
                sinv01 = param01*sinE01/ecos01;
                cosvw01 = cosv01 * coswrv01 - sinv01 * sinwrv01;

        mu02 = 2*pi/P02;
```

```
        wwrv02 = wrv02*DegToRad;

        coswrv02 = cos(wwrv02);

        sinwrv02 = sin(wwrv02);

        param02 =  sqrt(1-ecc02*ecc02);


        kepler(ecc02,mu02*(ct-T02));

        E02 = EE;


                sinE02 = sin(E02);

                cosE02 = cos(E02);

                ecos02 = 1 - ecc02 * cosE02;

                cosv02 = (cosE02 - ecc02)/ecos02;

                sinv02 = param02*sinE02/ecos02;

                cosvw02 = cosv02 * coswrv02 - sinv02 * sinwrv02;



                vorb = agamma +

                        + K01*(ecc01*coswrv01+cosvw01)

                        + K02*(ecc02*coswrv02+cosvw02);


}


kepler(ecc,M)

{

        variable n;

        EE = M;

        for(n = 0; n < 100; n=n+1)

        {

                EE = M + ecc*sin(EE);

        }

        return EE;

}
```